MECHANISMS FOR THE EXISTENCE OF DIAGONAL SOUTHERN HEMISPHERE CONVERGENCE ZONES

A thesis submitted to the School of Environmental Sciences
of the University of East Anglia in partial fulfilment
of the requirements for the degree of Doctor of Philosophy

KARIN VAN DER WIEL

JUNE 2015

ABSTRACT

This thesis considers the northwest-southeast, diagonal, orientation of the South Pacific and South Atlantic Convergence Zones (SPCZ and SACZ, respectively) which provide vital precipitation locally and influence mean climate globally. Their basic formation mechanism is not fully understood.

A conceptual framework is developed to explain the mechanism responsible for the SPCZ diagonal orientation. Wind shear and Rossby wave refraction cause vorticity centres in the subtropical jet to develop a diagonal orientation and propagate equatorward towards the eastern Pacific upper-tropospheric westerlies. Ascent ahead of cyclonic vorticity anomalies in the wave then triggers deep convection parallel to the vorticity centre. Latent heat from condensation forces additional ascent and upper-tropospheric divergence; through vortex stretching this leads to an anticyclonic vorticity tendency. The calculation of a vorticity budget shows this tendency is strong enough to dissipate the wave. A similar sequence of events triggers diagonal bands of convection in the SACZ, though the vortex stretching feedback is not strong enough to dissipate the Rossby wave.

An atmospheric general circulation model is used to investigate this mechanism. In an experiment the parametrisation of convection is modified: dynamic Rossby wave forcing is decoupled from the usual thermodynamic response. Consequently, Rossby waves over the SPCZ region are not dissipated, confirming the feedback in the framework. Furthermore, it is shown that SPCZ convective events decrease the strength of the eastern Pacific upper-tropospheric westerlies.

Further experiments show which surface boundary conditions support the SPCZ diagonal orientation. Continental configuration, orography and absolute Sea Surface Temperatures (SST) do not have a significant influence. The key boundary condition is the zonally asymmetric component of the SST distribution. This leads to a strong subtropical anticyclone over the southeast Pacific that transports and supplies moisture to the SPCZ. Convection is triggered when the dynamical forcing from Rossby waves is present.

CONTENTS

LIST OF FIGURES

LIST OF TABLES

LIST OF SYMBOLS

$\mathbf{c_g}$	Group velocity
$\mathbf{c_{gs}}$	Group velocity for stationary waves
c_x	Zonal phase speed
C_p	Specific heat of dry air at constant pressure
D	Divergence
f	Coriolis parameter, planetary vorticity
J	Diabatic heating
k	Zonal wavenumber
$\mathbf{k}$	Unit vector along vertical axis
K	Total wavenumber
K_s	Total stationary wavenumber
l	Meridional wavenumber
p	Pressure
p_s	Surface pressure
q	Water vapour mixing ratio
t	Time
T	Temperature
u	Zonal wind component (eastward)
$\mathbf{U}$	Three dimensional velocity, (u, v, ω)
v	Meridional wind component (northward)
$\mathbf{V}$	Horizontal velocity, (u, v)
x	Horizontal axis in the eastward direction
y	Horizontal axis in the northward direction
β	Meridional gradient of planetary vorticity
$\hat{\beta}$	Meridional gradient of absolute vorticity
ζ	Relative vorticity
η	Absolute vorticity

θ	Potential temperature
λ	Longitude
ρ	Density
σ	Vertical coordinate in σ system
τ	Relaxation time
ϕ	Latitude
Φ	Geopotential
ψ	Streamfunction
ω	Angular frequency
ω	Pressure velocity

LIST OF ACRONYMS

AGCM	Atmospheric General Circulation Model
AMIP	Atmospheric Model Intercomparison Project
BOM	(Australian) Bureau of Meteorology
CAPE	Convective Available Potential Temperature
CMAP	CPC Merged Analysis of Precipitation
CMIP	Coupled Model Intercomparison Project
CPC	Climate Prediction Center
CSIRO	Commonwealth Scientific and Industrial Research Organization
DJF	December, January, February
DOE	(US) Department of Energy
ENSO	El Niño-Southern Oscillation
EOF	Empirical Orthogonal Function
GOES	Geostationary Operational Environmental Satellite
GPCC	Global Precipitation Climatology Centre
IGCM	Intermediate General Circulation Model
IPCC	Intergovernmental Panel on Climate Change
IPO	Interdecadal Pacific Oscillation
ITCZ	Intertropical Convergence Zone
JJA	June, July, August
MJO	Madden-Julian Oscillation
NCAR	(US) National Center for Atmospheric Research
NCEP	(US) National Center for Environmental Prediction
NESDIS	(US) National Environmental Satellite, Data, and Information Service
NOAA	(US) National Oceanic and Atmospheric Administration
OLR	Outgoing Longwave Radiation
OPI	OLR-based Precipitation Index

PC	Principle Component
SACZ	South Atlantic Convergence Zone
SICZ	South Indian Convergence Zone
SPCZ	South Pacific Convergence Zone
SST	Sea Surface Temperature
WKB	Wentzel-Kramers-Brillouin (approximation)

ACKNOWLEDGEMENTS

I'm singing in the rain; I'm laughing at clouds; what a glorious feeling[1] – I'm happy to say the work is done, the thesis has been written. The past three years have been a great adventure. Although I can't thank everyone that supported me over this time, I would like to express my gratitude to everyone who made me laugh, made me leave my computer or who feigned interest in rain and Rossby waves during this time.

I would like to thank my supervisors, Adrian Matthews, Dave Stevens and Manoj Joshi, for their contributions and time. Thank you for taking me on as a student, for giving plenty of encouragement in our meetings, for always providing new ideas and for never failing to answer any questions I may have had. It has been a pleasure to work with you. I think we made great progress, whither the SPCZ. Thanks also to the Faculty of Science for providing funding to study at UEA and to the HPC support staff, who, despite continued efforts of its users, keep the cluster running.

Thanks to everyone, past and present, in 3.17 for making days in the office as much fun as days off work. Thanks to Céline for discussions on waves and convection, whether it be atmospheric or oceanic, green or red. To Tahmeena for being a wonderful friend and for lovely dinner parties. To Laura for promoting healthy procrastination in the gym. To Richard and his crosswords. To Honza, always willing to help when I was mathematically stuck. To Nick and Andy for being friends, despite the fact that the Dutch are better at football, and to Chris for fighting swans.

Thanks to the UEA ClimateSnack group, it was a pleasure to write something that is not this thesis. To the UEA ladies' hockey club and the girls of the 3s, 20 wins and 108 goals this season make us champion of Norfolk. To friends in the Netherlands who kept in contact and came for a visit and finally, to Pap and Map, for igniting curiosity, starting a love of maths and physics, and teaching me how to set my sails, no matter what the wind is like – the sky is the limit.

[1] Adapted from Gene Kelly, Singin' in the rain, 1952.

1

INTRODUCTION

Austral summer precipitation in the Southern Hemisphere subtropics is organized into distinct, large-scale, northwest-southeast, diagonally oriented bands (figure 1.1), in contrast to the Northern Hemisphere, where there are no such diagonal bands of precipitation; only the zonal Intertropical Convergence Zone (ITCZ). The South Pacific Convergence Zone (SPCZ) is the most prominent of these Southern Hemisphere diagonal bands, extending from New Guinea southeastward to the central, subtropical Pacific Ocean. At its tropical boundary the SPCZ becomes more zonal and joins the ITCZ over the Indian Ocean. Over South America, the South Atlantic Convergence Zone (SACZ) extends from the Amazon, over Paraguay and southern Brazil, towards the South Atlantic Ocean. And, though it is much weaker, the South Indian Convergence Zone (SICZ) over Africa and Madagascar is often described as the third diagonal convergence zone.

This thesis considers the origin, variability and climatic effect of these diagonally oriented bands of precipitation. Observational based data products are used to develop a dynamical framework for their existence, building on previous studies that emphasize the role of tropical-extratropical interactions. Furthermore, modelling experiments with an intermediate complexity Atmospheric General Circulation Model (AGCM) are conducted to test this framework, to study the effect of diabatic heating during convective events in the SPCZ region on other aspects of the larger Pacific climate and to investigate the (pre-)requisite conditions for a diagonally

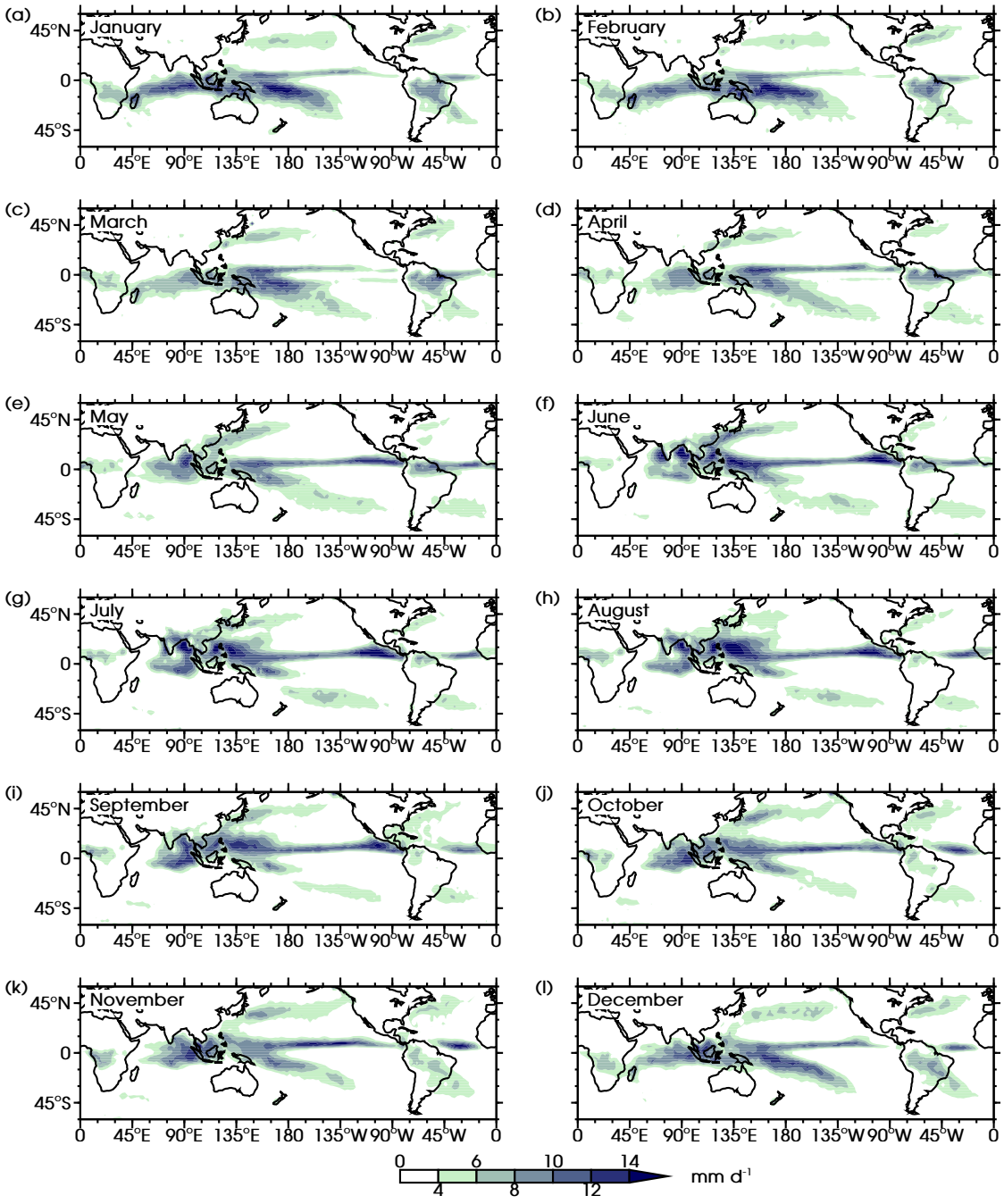

Figure 1.1: Monthly mean precipitation rate (mm d^{-1}, data source: CMAP, mean over 1979–2008). Months: (a) January, (b) February, (c) March, (d) April, (e) May, (f) June, (g) July, (h) August, (i) September, (j) October, (k) November and (l) December.

oriented SPCZ.

1.1 DIAGONAL CONVERGENCE ZONES

The first mention of the SPCZ in a scientific publication is often attributed to Hubert (1961). Newly available satellite images provided better data for the identification of large-scale patterns than the existing, sparse, Pacific surface observation network (Anderson *et al.*, 1974). From then onwards satellite data were used widely and the non-zonal cloud bands found across Southern Hemisphere ocean basins were observed in more studies (e.g. Kornfield *et al.*, 1967; Godshall, 1968; Bjerknes, 1969; Kornfield & Hasler, 1969; Streten, 1970). It was Streten (1973) that pulled data together and created seasonal mean maps of cloud cover. The SPCZ and SACZ were identified as persistent and prominent features in the precipitation climate of the Southern Hemisphere. The SICZ was noted to be weaker and to show more variability in both position and intensity.

Based on surface stations across the Pacific, Meehl (1987) discussed the seasonal cycle in sea level pressure, Outgoing Longwave Radiation (OLR) and precipitation rates. In figure 1.1 monthly maps of the distribution of precipitation are shown. Precipitation rates in the SPCZ, SACZ and SICZ are strongest during austral summer (December, January, February). In the months following the austral summer the precipitation rate in the SPCZ decreases. During austral winter (June, July, August) the precipitation rate is at its minimum, the SPCZ 4 mm d^{-1} contour no longer extends into the subtropics. Instead the precipitation pattern in the subtropical southern Pacific resembles that of the storm tracks found at similar latitudes in the Northern Hemisphere during boreal winter. The annual cycle of SACZ precipitation is similar to that of the SPCZ. The SICZ disappears completely outside austral summer. For this reason, the research in this thesis only considers the SPCZ and SACZ, and focuses on the six months in which these are most strongly developed: November to April (Meehl, 1987; Haffke & Magnusdottir, 2013).

Despite differences in land-sea distributions and Sea Surface Temperature (SST) patterns, several common features have been identified for the regions of the SPCZ, SACZ and SICZ. At their equatorial end, the three convergence zones are all linked to a region of deep tropical convection, i.e. the warm pool and maritime continent

for the SPCZ and the South American and African continents for the SACZ and SICZ, respectively. Also, the three convergence zones are located to the west of a subtropical high. Northeasterly flow on the western flank of these highs converges with southeasterly flow from higher latitudes along the mean axes of precipitation. Finally, there is a subtropical upper-tropospheric jet in the vicinity of the convergence zones (Trenberth, 1976, 1991; Kodama, 1992, 1993; Salinger *et al.*, 1995; Vincent, 1994; Widlansky, 2010). In the Northern Hemisphere similar features were found around the Baiu frontal zone, stretching from Japan into the Pacific Ocean (Kodama, 1992, 1993).

Both the SPCZ and the SACZ have a significant influence on Southern Hemisphere weather and climate. For example, the SPCZ is is one of the main sources of lightning activity in the region away from land (Ortega & Guignes, 2007) and a location favourable for tropical cyclone development (Vincent *et al.*, 2011; Lorrey *et al.*, 2012). The SPCZ is a well-defined maximum in front frequency (Berry *et al.*, 2011). The development of the SPCZ in December-February and related decreasing boundary layer wind speeds play an important role in terminating strong El Niño events (McGregor *et al.*, 2012). The associated changes to the boundary layer wind field with the SPCZ also impact coral reefs; extreme shifts of the SPCZ during three especially strong El Niño events have led to a significant drop of sea level and subsequent dying of shallow reefs in the western Pacific (Widlansky *et al.*, 2014). The SACZ interacts with the South American monsoon (Nieto Ferreira *et al.*, 2011; Jorgetti *et al.*, 2014) and a strong SACZ, through a cloud-radiation feedback, cools SSTs over the southwest tropical Atlantic (Chaves & Nobre, 2004; Jorgetti *et al.*, 2014). Finally, midlatitude disturbances interact with the convergence zones. This was already observed by Streten (1973) and is often mentioned as a potential mechanism for the formation of diagonally oriented precipitation zones (see section 1.1.2).

The SPCZ covers a large area and the inhabitants of many South Pacific island states depend on it for its precipitation (figure 1.2). Small changes away from the climatological mean in SPCZ location or strength have resulted in drought and flooding across the region (Griffiths *et al.*, 2003; Kumar *et al.*, 2006; Murphy *et al.*, 2014). Variations in SACZ orientation and strength impact South American countries such as Brazil, Paraguay, Uruguay and Argentina (Barros *et al.*, 2000; Todd *et al.*, 2003; Espinoza *et al.*, 2014). The importance of the convergence zones to both climate

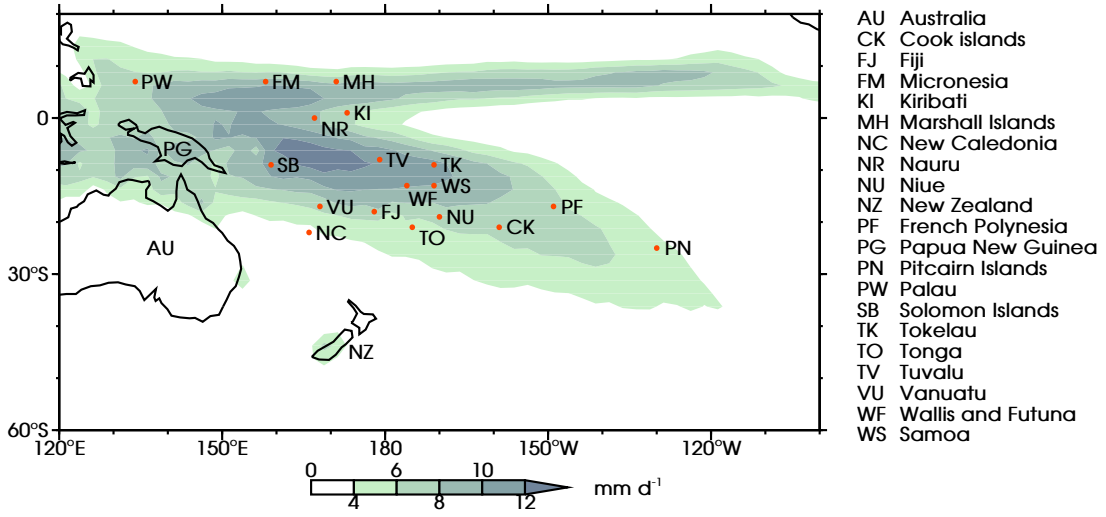

Figure 1.2: Map of the South Pacific region. The location of the member states of the Pacific Island Forum are indicated in red dots if the island (group) is too small for the map resolution. Shaded colours show November to April time mean precipitation rate (mm d^{-1}).

and society on local scales, and the wider Pacific climate, make it important to have good scientific understanding of the atmospheric mechanisms that create and maintain them, and the processes that force the observed variability. This is especially important in the context of providing reliable projections of their development in a future warmer climate.

1.1.1 TEMPORAL VARIABILITY

The precipitation distribution and the mean synoptic situation in the vicinity of the SPCZ and SACZ vary on several different time scales. By means of power spectra computed along the SPCZ mean precipitation axis, Widlansky *et al.* (2011) show that the tropical end of the SPCZ varies at time scales of approximately 2 weeks and 30–60 days. In the subtropical part of the SPCZ (south of 20°S) variability shifts towards shorter time scales, i.e. to synoptic variability at less than 8 days. In this section the temporal variability within the SPCZ and SACZ is discussed, starting at short synoptic time scales (~ 1-10 days) and moving towards longer time scales.

It was recognised early that the SPCZ shows variability on synoptic timescales (e.g. Streten, 1973). Trenberth (1976) noted frontal systems originating in the southwest ended their lifecycle in the SPCZ; he referred to the SPCZ region as "*a 'graveyard' region for fronts*". In both the SPCZ and SACZ, variability at short time scales is more

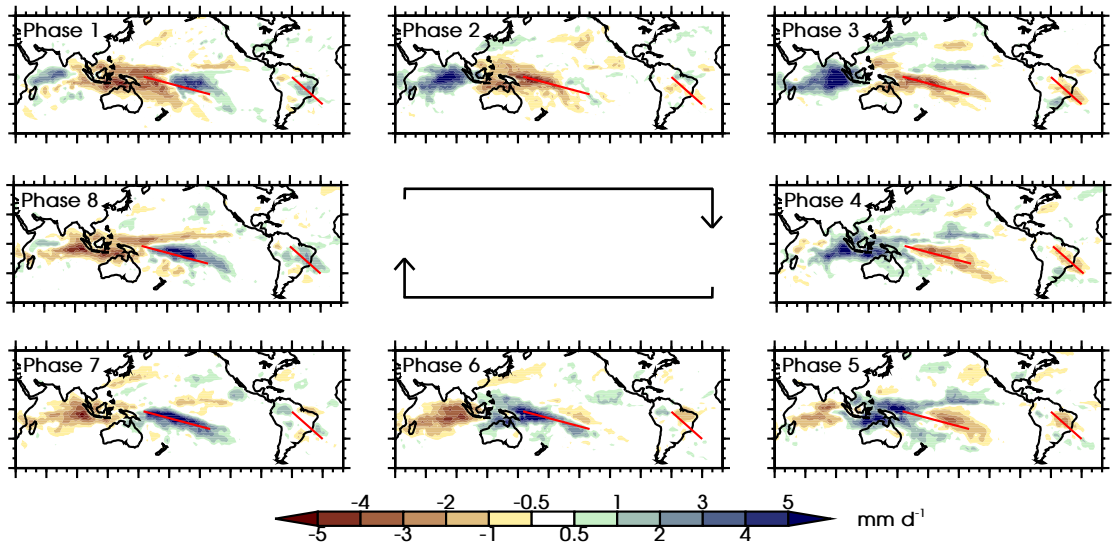

Figure 1.3: Precipitation anomalies (mm d^{-1}) during 8 MJO phases (clockwise progression). Phases based on the Wheeler & Hendon (2004) method[1]. Red diagonal lines indicate the position of the SPCZ and SACZ climatological mean precipitation axes.

enhanced in the subtropical part than in the tropical part (Liebmann *et al.*, 1999; Widlansky, 2010; Widlansky *et al.*, 2011). Widlansky *et al.* (2011) and Matthews (2012) propose dynamical mechanisms for the observed synoptic variability, these will be discussed in section 1.1.2.

On intraseasonal timescales, the Madden-Julian Oscillation (MJO) forces significant changes in atmospheric convection and precipitation over the tropics. The MJO is an eastward propagating dipole pattern of enhanced and reduced convection; it moves from the Indian Ocean towards the maritime continent and into the western Pacific Ocean (Madden & Julian, 1971, 1972; Zhang, 2005). Wheeler & Hendon (2004) present an index to distinguish different MJO phases; during its eastward progression the dipole pattern passes through eight phases. The precipitation anomalies associated with these phases are shown in figure 1.3. In phase 1 enhanced convection develops over the Indian Ocean; this anomaly propagates eastward in the consecutive phases. In phase 5 an anomaly of reduced convection develops over the Indian Ocean and follows eastward. The SPCZ location and intensity is dependent on the current MJO phase. During MJO phase 6 the SPCZ is in its normal position and precipitation rates are stronger than normal. As the MJO progresses this enhanced convection anomaly moves equatorward and eastward (Matthews, 2012; Haffke &

[1] Source: http://www.bom.gov.au/climate/mjo, accessed 2 March 2015

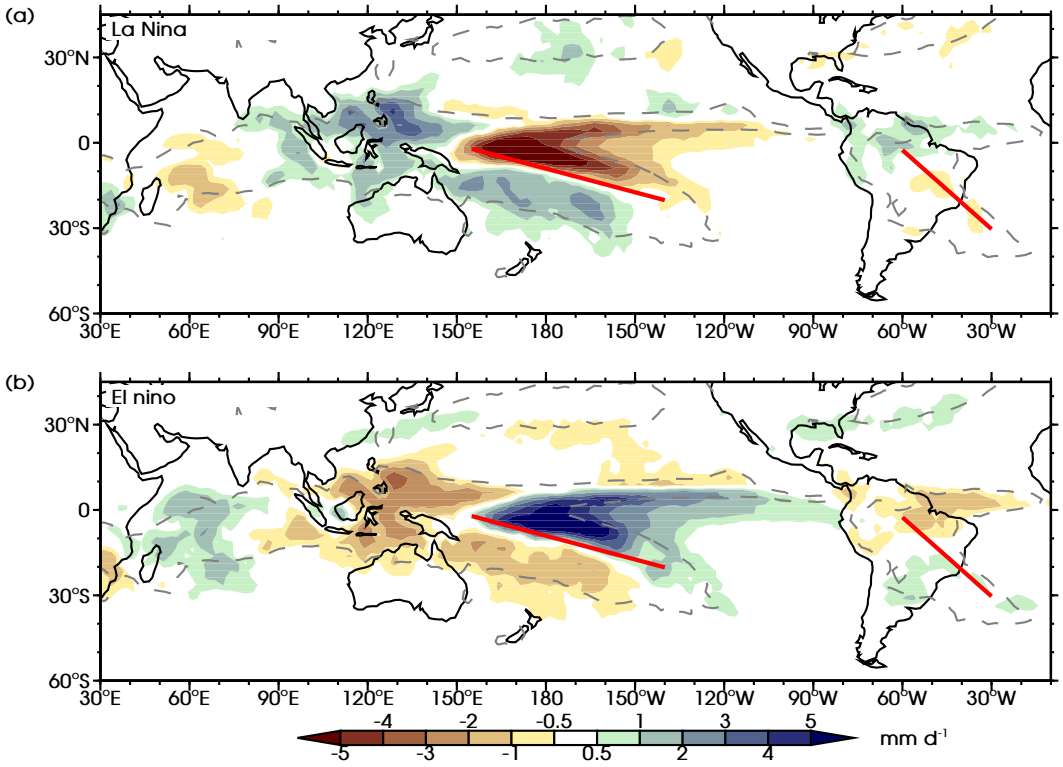

Figure 1.4: Precipitation anomalies (mm d^{-1}) during (a) La Niña and (b) El Niño years. La Niña and El Niño years are defined as years in which the December to January Niño 3.4 SST anomaly exceeded ±0.5°C[2]. The grey dashed line shows the climatological mean 4 mm d^{-1} contour, the thick red diagonal lines indicate the position of the SPCZ and SACZ climatological mean precipitation axes.

Magnusdottir, 2013). The MJO also modulates the location and intensity of SACZ events (Carvalho *et al.*, 2004). The SACZ shifts to the northeast in MJO phases 8 and 1 and to the southwest during MJO phases 3, 4 and 5. The dynamical processes involved in the variability of the SPCZ and the SACZ associated with MJO phase changes are not fully understood, though Matthews *et al.* (1996) discuss a Rossby wave mechanism for the evolution of convection along the SPCZ within a MJO cycle.

On interannual timescales shifts in the position of the mean SPCZ precipitation axis generally align with different modes of El Niño-Southern Oscillation (ENSO). During the ENSO cold phase (La Niña) zonal asymmetries in the SST distribution increase and the SPCZ moves poleward and westward (figure 1.4a). During the ENSO warm phase (El Niño) zonal asymmetries of SSTs decrease and the SPCZ shifts towards the equator and east (figure 1.4b, Vincent *et al.*, 2011; Haffke &

[2]Source: http://www.cpc.noaa.gov/products/analysis_monitoring/ensostuff/ensoyears.shtml, accessed: 2 March 2015

Magnusdottir, 2013; Murphy *et al.*, 2014). The largest precipitation changes are within the climatological 4 mm d^{-1} contour for both La Niña and El Niño years. During El Niño years there is are additional changes over the equatorial east Pacific. This is related to three extreme El Niño events (1982-83, 1991-92, 1997-98) that resulted in a collapse of the SPCZ; instead of a diagonally oriented SPCZ there was a broad zonal band of precipitation on the equator (Vincent *et al.*, 2011; Cai *et al.*, 2012; Borlace *et al.*, 2014; Widlansky *et al.*, 2014). ENSO related changes to the SACZ are smaller. During La Niña years changes are minor, in El Niño years precipitation increases mostly in the coastal and oceanic parts of the SACZ (Grimm *et al.*, 2000; Carvalho *et al.*, 2004).

On longer timescales, the impact of the Interdecadal Pacific Oscillation (IPO, also referred to as Pacific decadal oscillation) on the SPCZ is comparable to that of ENSO. The IPO has a typical timescale of 15–30 years; its SST signature is ENSO-like but extends further away from the equator (Power *et al.*, 1999). During IPO warm phases the SPCZ shifts northeastward, during IPO cold phases it shifts southwestward. When ENSO and the IPO have coinciding warm or cold phases, shifts of the SPCZ are largest (Salinger *et al.*, 2001; Folland *et al.*, 2002). Also in the SACZ region, the IPO acts to strengthen or weaken the effects of ENSO related variability depending on whether the two oscillations are in or out of phase (Kayano & Andreoli, 2007).

1.1.2 PROPOSED MECHANISMS

There are few studies that attempt to determine the relative roles of different dynamic and/or thermodynamic processes in setting the diagonal orientation of the SPCZ and the SACZ. Following an international workshop on the SPCZ, Power (2011) called for scientific efforts to increase understanding of the reasons why the SPCZ exists and the relative roles of orography, air-sea coupling and synoptic variability on SPCZ position and strength. The co-variability of the SST patterns (e.g. related to ENSO or IPO) and SPCZ and SACZ position suggests that the SST distribution has a role in the mechanism to create a diagonal SPCZ. Furthermore, a link between Rossby wave activity on synoptic time scales and convection within the SPCZ is known to exist (Streten, 1973; Trenberth, 1976).

Over tropical oceans precipitable water is mostly supplied by low-level moisture

convergence. Whether ascending motions in deep convection result in low-level convergence, or whether this convergence determines the location of climatological deep convection remains unclear (Back & Bretherton, 2009). Gill (1980) described the first mechanism in a model; diabatic heating in deep convection drives vertical motions that in turn drive the low-level tropical atmospheric circulation. Lindzen & Nigam (1987) developed a model for the second mechanism: SST gradients set surface pressure gradients by means of turbulent fluxes, the low-level winds result from these pressure gradients. Though both individual models have been very influential, many studies since have debated their assumptions and simplifications (e.g Neelin, 1989; Gutzler & Wood, 1990; Battisti *et al.*, 1999; Wang & Li, 1993).

The tropical part of the SPCZ is oriented more zonally than the subtropical part and is associated with strong low-level convergence and located along the largest gradients of SST. Along the eastern SPCZ margin a causal relationship has been identified between reduced trade winds and subsequent increased atmospheric moisture and increased precipitation in the SPCZ region (Vincent, 1994; Lintner & Neelin, 2008). Model studies on the influence of mountains and continental configuration on the climate show that these influence Pacific SSTs, the east Pacific dry zone, lower-tropospheric winds and the precipitation distribution (Kiladis *et al.*, 1989; Wang & Li, 1993; Kitoh, 1997, 2002; Takahashi & Battisti, 2007a,b).

As discussed before, the subtropical part of the SPCZ is more diagonally oriented, shows variability on shorter, synoptic time scales and is associated with extratropical weather systems. Widlansky *et al.* (2011) and Matthews (2012) discuss mechanisms involved in these interactions. The mechanism proposed by Widlansky *et al.* (2011) is based on theoretical work of Webster & Chang (1991). Synoptic disturbances that exit the subtropical jet propagate northeastward. The jet-exit region is an area of $\frac{\partial \overline{u}}{\partial x} < 0$, referred to as an area of negative stretching deformation, where u is the zonal wind component and x is the horizontal axis in the eastward direction. Wave propagation slows in this area and consequently there is an accumulation of wave energy. Widlansky *et al.* (2011) show by means of observational data and modelling experiments that this area of negative stretching deformation is correlated with the location of convection in the SPCZ. ENSO related changes to the atmospheric mean state show that the location of the area of negative stretching deformation and the location of the SPCZ convection co-vary.

The framework proposed by Matthews (2012) is also based on the northeastward propagation of disturbances originating in the subtropical jet. Instead of describing climatological mean processes, a more direct forcing mechanism is suggested. By means of Empirical Orthogonal Function (EOF) analysis, SPCZ modes of variability are found. Composite analysis is then used to describe the temporal evolution of these modes. It is observed that originally circular centres within a Rossby wave develop a northwest-southeast orientation once they reach the SPCZ region. Poleward flow ahead of cyclonic anomaly centres in the Rossby wave is associated with ascent and decreased static stability according to quasi-geostrophic dynamics. The tropics with high SSTs and conditionally unstable atmospheric conditions are sensitive to such forcing. Subsequently, deep convection and precipitation is triggered in a northwest-southeast band, parallel to the cyclonic anomaly in the wave. Interannual variability of the SPCZ is suggested to be due to changes to the propagation of Rossby waves. Observational analysis has shown that transient convection in the ITCZ during austral summer can be explained by the same sequence of events, involving Rossby waves propagating equatorward from the Northern Hemisphere (Kiladis & Weickmann, 1992a,b; Kiladis, 1998).

The early observation by Trenberth (1976) that the SPCZ region acts as a graveyard region for storms is in agreement with both mechamisms. Widlansky *et al.* (2011) suggest this is due to the slowing down of waves in the area of negative stretching deformation. Matthews (2012) again proposes a more causal mechanism. Diabatic heat release in the deep convection enhances ascending motions and results in upper-tropospheric divergence. Divergence is a source of anti-cyclonic vorticity through vortex stretching, $\frac{\partial \zeta}{\partial t} = -fD$, where ζ is relative vorticity, t is time, f is the Coriolis parameter or planetary vorticity and D is divergence. By means of a simple scale analysis it is hypothesized that the vortex stretching effect is strong enough to dissipate the Rossby wave within a day. The proposed mechanism is thus: Rossby waves propagate into the SPCZ region, trigger convection along the SPCZ and dissipate in situ, in the SPCZ graveyard.

The zonal stretching deformation hypothesis is also valid in the SACZ region (Widlansky, 2010). Furthermore, a similar configuration of upper-tropospheric Rossby waves and convection to that proposed by Matthews (2012) has been observed for the SACZ (Liebmann *et al.*, 1999; Robertson & Mechoso, 2000). Aquaplanet

experiments have demonstrated the importance of equatorward propagating midlatitude disturbances in setting up a diagonal precipitation band (Nieto Ferreira & Chao, 2013).

1.1.3 PROJECTIONS OF CHANGE IN A WARMER CLIMATE

Coupled ocean-atmosphere climate models are the main tool to help understand and investigate potential changes to the large-scale climate system in response to increasing greenhouse gas concentrations (IPCC, 2013). However, before investigating the effects of climate change, the ability of coupled models to capture the spatial position and temporal variability of the SPCZ and SACZ has to be evaluated. The models included in the Coupled Model Intercomparison Project phase 3 (CMIP3, Meehl *et al.*, 2007) simulate the SPCZ with varying quality: four models do not simulate a distinct SPCZ, none of the other models capture the observed diagonal orientation of the SPCZ. Models that use ocean-atmosphere heat flux adjustments have smaller SST biases and simulate the most realistic precipitation distributions (J R Brown *et al.*, 2011).

The next generation of coupled models in CMIP phase 5 (CMIP5) have an improved spatial pattern of precipitation over the Pacific, though in many models the 'double ITCZ' band is stronger than in CMIP3. Most models capture the observed ENSO-related variability of the SPCZ (J R Brown *et al.*, 2013). When the atmospheric model component is forced with observed SST patterns rather than coupled to the ocean model component the biases are reduced (appendix A). The observed biases in coupled models have been related to the westward extension of the eastern Pacific cold tongue in SSTs and feedback processes in the coupled atmosphere-ocean system (e.g. Zhang & Wang, 2006; Lin, 2007; Zhang *et al.*, 2007). Despite these biases in the mean state, the observed relation between surface winds, moisture transport and south Pacific precipitation is replicated by CMIP5 models (Lintner & Neelin, 2008; Niznik & Lintner, 2013). Furthermore, the observed tropical-extratropical interactions by means of transient Rossby waves is also simulated in these models (Niznik *et al.*, 2015).

Future projections of changes in tropical Pacific SSTs show a robust increase, with weak inter-model variance. However, projections of changes to the distribution of

precipitation show large inter-model uncertainty; variability and biases are larger than projected changes (J R Brown *et al.*, 2012, 2013; Widlansky *et al.*, 2013). J N Brown *et al.* (2013) emphasize the importance of taking into account model biases when making climate projections for the western Pacific. Widlansky *et al.* (2013) follow this advice and investigate changes to the SPCZ by means of an AGCM forced with an observed SST climatology plus added warming trend from the CMIP3 A1B scenario[3]. Two competing mechanisms were identified:

Thermodynamic – Specific humidity increases over the entire Pacific, which enhances the hydrological cycle ('wet gets wetter', Held & Soden, 2006). The atmospheric moisture content increases over the SPCZ and decreases in the southeast Pacific, enlarging existing differences of moisture content and precipitation (figure 1.5a).

Dynamic – Warming is greatest over the equator, as a result a monsoon-like meridional circulation is created. There is moisture transport from the SPCZ to the ITCZ, the 'warmest get wetter' (figure 1.5b).

By means of a regime sorting method (originally proposed by Bony *et al.*, 2004; Bellucci *et al.*, 2010), J R Brown *et al.* (2013) find that 20 of 21 models simulate the thermodynamic increase of SPCZ precipitation and 11 of 21 models simulate the negative precipitation trend due to dynamic changes.

1.2 TROPICAL-EXTRATROPICAL INTERACTIONS

As discussed before, many studies have found links between the Southern Hemisphere diagonal convergence zones and extratropical disturbances. Extratropical influence on the tropics is often by means of Rossby waves. The proposed mechanisms of Widlansky *et al.* (2011) and Matthews (2012) are both based on transient Rossby waves that propagate northeastwards from the subtropical jet. In this section theoretical Rossby wave behaviour is summarised. First the dispersion relation for barotropic Rossby waves is derived (section 1.2.1), followed by a description of the ray tracing technique to find patterns of Rossby wave propagation (section 1.2.2).

[3] In this scenario fossil fuel emissions peak mid-21st century and decline slowly thereafter (IPCC, 2000)

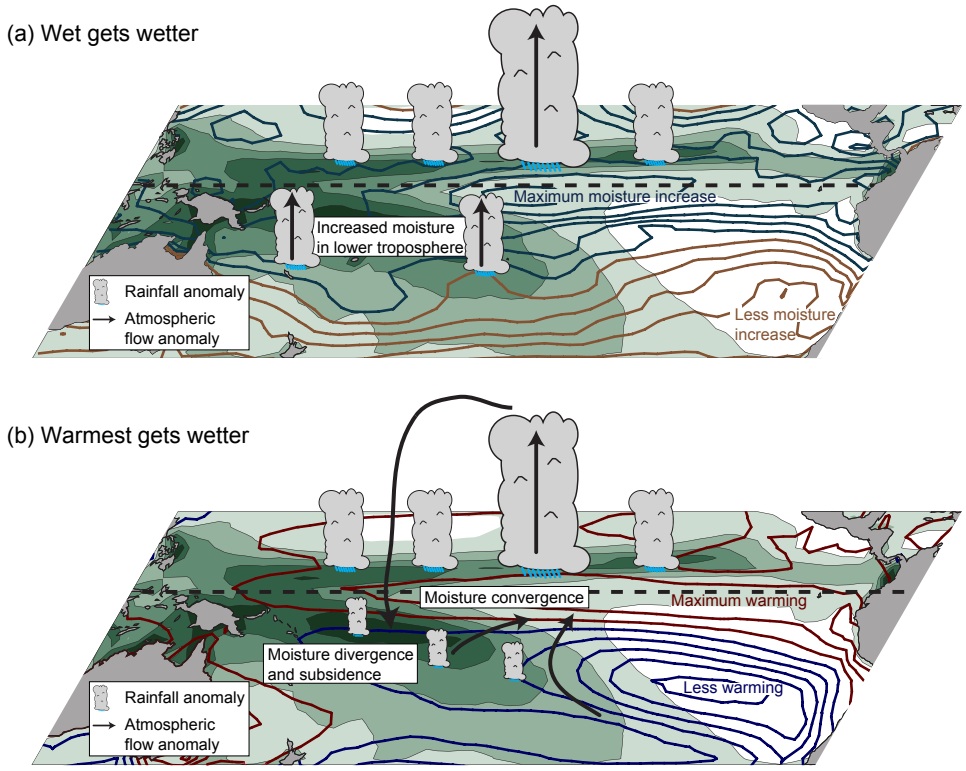

Figure 1.5: Illustration of two opposing mechanisms responsible for the SPCZ precipitation response to projected 21st-century greenhouse warming. Time mean precipitation in green shading (December-February; 2 mm d^{-1} contour interval, starting at 1 mm d^{-1}), large schematic clouds show increasing mean precipitation, small clouds show decreasing mean precipitation, arrows indicate changes to the atmospheric mean flow. (a) Projected near-surface moisture increase in contours (brown contours indicate increases less than 2 g kg^{-1}, blue contours increases more than 2 g kg^{-1}; 0.25 g kg^{-1} contour interval). (b) Projected twenty-first-century multi-model temperature trend (blue contours indicate warming less than the tropical mean (42.5°N/S), red contours warming more than the tropical mean; 0.2°C contour interval, starting at ±0.1°C). Taken from Widlansky *et al.* (2013).

1.2.1 BAROTROPIC ROSSBY WAVES

Rossby waves, or planetary waves, form due to the variation of the Coriolis parameter with latitude, the β-effect. Rossby wave propagation in a non-divergent barotropic atmosphere is an absolute vorticity (η) conserving process, with $\eta = \zeta + f$:

$$\frac{D_h}{Dt}\left(\zeta + f\right) = 0, \tag{1.1}$$

with

$$\frac{D_h}{Dt} = \frac{\partial}{\partial t} + u\frac{\partial}{\partial x} + v\frac{\partial}{\partial y},$$

in which v is the meridional wind component, y is the horizontal axis in the northward direction and subscript h denotes the horizontal plane. Equation 1.1 is the non-divergent barotropic vorticity equation (Holton, 2004, equation 4.27). In a mean westerly, zonally symmetric flow with small amplitude perturbations,

$$u = \overline{u}(y) + u'(x,y,t), \tag{1.2}$$

$$v = v'(x,y,t). \tag{1.3}$$

$$\zeta = \overline{\zeta}(y) + \zeta'(x,y,t),$$

$$u' = -\frac{\partial \psi'}{\partial y}, \quad v' = \frac{\partial \psi'}{\partial x},$$

$$\zeta' = \nabla_h^2 \psi',$$

equation 1.1 reduces to:

$$\left(\frac{\partial}{\partial t} + \overline{u}\frac{\partial}{\partial x}\right)\zeta' + v'\hat{\beta} = 0,$$

$$\left(\frac{\partial}{\partial t} + \overline{u}\frac{\partial}{\partial x}\right)\nabla_h^2 \psi' + \frac{\partial \psi'}{\partial x}\hat{\beta} = 0, \tag{1.4}$$

where ψ' is the perturbation streamfunction and

$$\hat{\beta} = \frac{\partial}{\partial y}\left(\overline{\zeta} + f\right)$$

is the meridional gradient of absolute vorticity of the basic state. Terms involving quadratic perturbation quantities have been neglected.

This equation is solved using plane wave solutions of the form

$$\psi' = \psi_0 e^{i(kx+ly-\omega t)},$$

in which k and l are the zonal and meridional wavenumbers, respectively, and ω is the angular frequency. This is a Wentzel-Kramers-Brillouin approximation (WKB, Gill, 1982, section 8.12; Karoly, 1983), in which it is assumed that the length scale of the perturbations is much smaller than the length scale of the mean flow. Simple algebra

gives

$$\frac{\partial \psi'}{\partial x} = ik\psi',$$
$$\frac{\partial \psi'}{\partial t} = -i\omega\psi',$$
$$\nabla_h^2 \psi' = -K^2\psi',$$

with $K = \sqrt{k^2 + l^2}$ the total wavenumber. Substituting these into equation 1.4 gives:

$$\left(-i\omega + \overline{u}ik\right)\left(-K^2\right)\psi' + ik\psi'\hat{\beta} = 0,$$

which results in the dispersion relation for barotropic Rossby waves:

$$\omega = \overline{u}k - \frac{\hat{\beta}k}{K^2}. \tag{1.5}$$

The zonal phase speed is then

$$c_x \equiv \frac{\omega}{k} = \overline{u} - \frac{\hat{\beta}}{K^2}, \tag{1.6}$$

which is always smaller than the mean zonal flow ($c_x < \overline{u}$), i.e. Rossby waves propagate westward relative to the mean flow ($c_x - \overline{u} < 0$).

The westward propagation of Rossby waves is shown qualitatively in figure 1.6. A chain of fluid parcels with initial $\zeta = 0$, aligned along a latitude is displaced meridionally (red line). For parcels displaced to the north f increases and therefore ζ becomes negative. Negative relative vorticity corresponds to clockwise motion (grey arrows). The displaced fluid parcels to the east of the vorticity maximum are therefore advected southwards; the fluid parcels to the west of the vorticity minimum are advected northwards (black arrows). As a result individual fluid parcels oscillate in a north-south direction; the wave pattern moves westward (green dashed line).

Rossby waves are dispersive, i.e. their phase speed depends on their wave length (equation 1.6). Longer waves (smaller K) travel westward faster than shorter waves (larger K). The total wavenumber, from equation 1.6, is

$$K = \sqrt{\frac{\hat{\beta}}{\overline{u} - c_x}}. \tag{1.7}$$

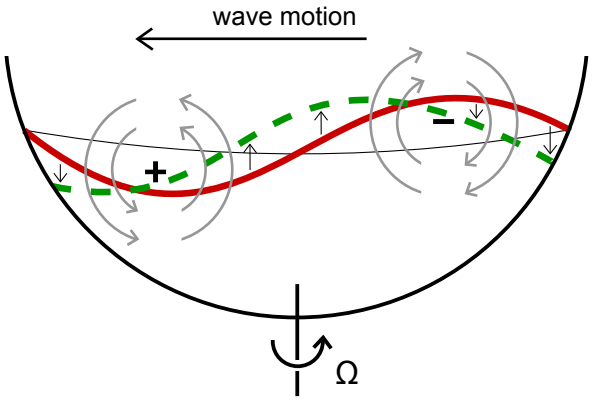

Figure 1.6: Schematic of westward Rossby wave propagation in the Southern Hemisphere. A meridionally displaced chain of fluid parcels (red line), induces a field of relative vorticity (+,−) and meridional velocity (grey arrows), due to advection by the induced velocity (black arrows) the wave pattern is displaced westward (green dashed line). Adapted from Holton (2004).

Rossby wave propagation is therefore limited to areas of mean relative westerlies ($\overline{u} - c_x > 0$) and positive $\hat{\beta}$. This was also observed in early observational and modelling based studies. Webster & Holton (1982) found that cross-equatorial Rossby wave propagation was only possible in areas of mean westerly flow at the equator, 'the westerly ducts'. In areas of mean easterlies a critical latitude was found when $\overline{u} = c_x$; Rossby wave propagation was observed to stop. Cross-equatorial Rossby wave propagation is limited to austral summer when the westerly duct is present, in austral winter waves are reflected or absorbed near the critical latitude (Hoskins & Ambrizzi, 1993; Ambrizzi *et al.*, 1995).

There is a wavelength, K_s, at which the westward wave propagation is balanced by the eastward advection by the mean wind ($c_x = 0$). The stationary wavenumber is

$$K_s = \sqrt{\frac{\hat{\beta}}{\overline{u}}}.$$

Rossby waves with $K < K_s$ have $c_x < 0$ and propagate westward relative to the Earth's surface; waves with $K > K_s$ propagate eastward ($c_x > 0$, Yang & Hoskins, 1996).

1.2.2 WAVE PROPAGATION PATHS

The phase speed discussed above denotes the propagation speed of individual troughs and ridges in a Rossby wave. Wave energy propagates at the group velocity,

given by

$$\mathbf{c_g} = (c_{gx}, c_{gy}), \tag{1.8}$$

which can be derived from the dispersion relation (equation 1.5):

$$c_{gx} \equiv \frac{\partial \omega}{\partial k} = c_x + \frac{2\hat{\beta}k^2}{K^4},$$

$$c_{gy} \equiv \frac{\partial \omega}{\partial l} = \frac{2\hat{\beta}kl}{K^4}.$$

For stationary Rossby waves ($c_x = 0$, $K = K_s$) the group velocity is in the same direction as the phase propagation, (k, l), as from 1.8:

$$\mathbf{c_{gs}} = \frac{2\hat{\beta}k}{K_s^4}(k, l). \tag{1.9}$$

The group velocity of westward propagating waves ($c_x < 0$) is more meridionally oriented, eastward propagating waves ($c_x > 0$) are more zonally oriented (Yang & Hoskins, 1996).

A 'ray' is defined to be in the direction of the local $\mathbf{c_g}$. Then, by means of ray tracing, the path of a Rossby wave through the varying mean flow can be computed. To do so, the rate of change of k, l and ω need to be considered. The following discussion is based on the theoretical work by Hoskins & Karoly (1981), Karoly (1983) and Hoskins & Ambrizzi (1993).

In the zonally symmetric, steady state mean flow (equations 1.2 and 1.3), k and ω are constant (Gill, 1982, section 8.12.3). The Rossby wave propagation path can therefore be computed by considering the rate of change of l only. Along a Rossby wave path (or ray, subscript p):

$$\frac{D_p l}{Dt} = \frac{dl}{dK}\frac{D_p K}{Dt}. \tag{1.10}$$

Using $l = \sqrt{K^2 - k^2}$ and

$$\frac{D_p}{Dt} = \frac{\partial}{\partial t} + c_{gx}\frac{\partial}{\partial x} + c_{gy}\frac{\partial}{\partial y}$$

equation 1.10 becomes

$$\frac{D_p l}{Dt} = \frac{K}{l}c_{gy}\frac{dK}{dy}. \tag{1.11}$$

The bending of the wave path can be described for stationary waves. For

stationary waves the group velocity, $\mathbf{c_{gs}}$, is parallel to (k, l) (equation 1.9), so

$$\frac{c_{gy}}{c_{gs}} = \frac{l}{K_s},$$

and equation 1.11 changes to

$$\frac{D_p l}{Dt} = c_{gs}\frac{dK_s}{dy}. \tag{1.12}$$

By means of trigonometry, equation 1.12 can be rewritten to describe the changing direction of wave propagation. Take α to be the angle between (k, l) and the x direction, then

$$\frac{D_p \tan(\alpha)}{Dt} = \frac{1}{k}\frac{D_p l}{Dt},$$

which gives

$$\frac{D_p \alpha}{Dt} = \cos^2(\alpha)\,\frac{1}{k}c_{gs}\frac{dK_s}{dy}. \tag{1.13}$$

From equation 1.11 it follows that wherever there is a meridional gradient of K, the meridional wavenumber, l, will change. In such regions, the Rossby wave path is curved. For stationary Rossby waves, the rate of change of α is described by equation 1.13. Rossby waves are refracted towards latitudes with larger K_s.

Hoskins & Ambrizzi (1993) use equation 1.13 to describe different hypothetical profiles of K_s and related refraction paths, a schematic representation of these is included in figure 1.7. In general, there is refraction towards latitudes with higher K_s (figure 1.7a). Special cases include a 'turning latitude' at which $k = K_s$ and $l = 0$ and the wave is reflected; a latitude at which $\hat{\beta} = 0$ and thus $K_s = 0$, the wave turns before reaching this latitude; a 'critical latitude' at which $\overline{u} = 0$ and $K_s \to \infty$, waves propagate into this latitude normally, though l and c_g tend to zero (as modelled by Webster & Holton, 1982); a local maximum of K_s can act as a waveguide for particular wavelengths ($K_1 < K_s < K_2$), most likely to occur in strong westerly wind jets (figure 1.7).

The derivation here is valid for a westerly, zonally symmetric mean flow (equations 1.2 and 1.3). Karoly (1983) extends this analysis for a more realistic time mean flow that is a function of both longitude and latitude

$$u = \overline{u}(x, y) + u'(x, y, t),$$
$$v = \overline{v}(x, y) + v'(x, y, t).$$

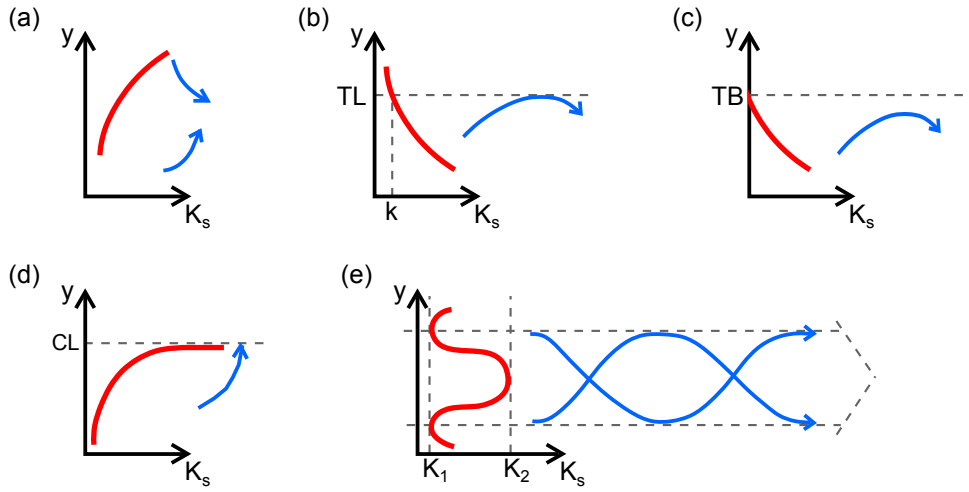

Figure 1.7: Schematic stationary Rossby wavenumber (K_S) profiles and ray path refraction. K_s is shown as a function of y (red line) and ray paths as curved arrows (blue). (a) simple refraction, (b) reflection from a turning latitude, TL, where $k = K_s$ and $l = 0$ (c) reflection before a latitude where $\hat{\beta} = 0$ and $K_s = 0$, (d) reflection into a critical latitude, CL, where $\overline{u} = 0$ and $K_s \rightarrow \infty$ (e) waveguide effect of a K_s maximum. Adapted from Hoskins & Ambrizzi (1993).

When the ray tracing technique is used in this thesis, the rate of change of k and l will be computed following the solution of that analysis.

It should be noted that the scale separation in the WKB approximation is not strictly met for long Rossby waves propagating on the mean flow. However many studies have found that the results obtained by the described ray tracing method do describe observed patterns of Rossby waves in the atmosphere (e.g. Hoskins & Ambrizzi, 1993; Yang & Hoskins, 1996; Matthews & Kiladis, 2000).

1.3 THESIS OUTLINE

The research presented in this thesis aims to increase the understanding of the dynamic and thermodynamic processes that determine the diagonal position and strength of the SPCZ and SACZ. Despite the work discussed in section 1.1, further insight into the detailed mechanisms promoting the SPCZ and SACZ is required. Bony *et al.* (2015) identify this question as one of four important open scientific question concerning the interactions of clouds, circulation and climate. Results could be applied to improve forecasts of SPCZ and SACZ positions on both synoptic and seasonal time scales, relevant for people locally. Additionally, it could aid process studies in CMIP5 models with the aim of improving the representation of the SPCZ

and SACZ and potentially reduce uncertainties of climate change projections.

The new work is presented in three chapters. Each chapter aims to answer a different question.

- **What is the origin of the diagonal orientation of the SPCZ and SACZ?**

In chapter 2 different aspects of the framework of Matthews (2012) for a diagonally oriented SPCZ are investigated in more detail. In particular, the observed reformation of centres in the transient Rossby wave, that is suggested to be important in setting the northwest-southeast orientation, is considered. This is done by means of the ray tracing technique described in section 1.2. Also, the strength of the proposed negative feedback mechanism is quantified by means of a full vorticity budget. The framework is extended to describe the origin of the diagonally oriented SACZ as well.

- **What is the effect of diabatic heating from convection in the SPCZ?**

In chapter 3 the interaction between transient Rossby waves and SPCZ convection, identified from the analysis of observational data (chapter 2), is tested. An AGCM of intermediate complexity is used to perform an ensemble of perturbation experiments in which the negative feedback mechanism is tested. The effect of diabatic heating on both local Rossby wave propagation and on the Pacific climatological mean flow will be considered.

- **Which surface boundary conditions are required for a diagonal SPCZ?**

In chapter 4 the AGCM is used for a set of experiments in which the influence of different atmospheric boundary conditions are tested separately. The impact of changes to land-sea contrasts, orography, absolute SST values and the zonally asymmetrical SST distribution on the orientation and strength of the SPCZ are investigated.

Final conclusions and discussions are given in chapter 5.

2

A DYNAMICAL FRAMEWORK FOR THE ORIGIN OF THE DIAGONAL SOUTH PACIFIC AND SOUTH ATLANTIC CONVERGENCE ZONES

This chapter is based on a paper that has been accepted for publication in the Quarterly Journal of the Royal Meteorological Society with the same title (Van der Wiel *et al.*, 2015a). The text in the chapter is largely unchanged from the published paper, apart from the introduction which has been shortened to avoid repetition of chapter 1. K. van der Wiel was responsible for the work, under supervision by A.J. Matthews, D.P. Stevens and M.M. Joshi, who provided scientific input and helped revise the text for publication. The comments of B.R. Lintner and an anonymous reviewer also helped to improve the manuscript.

2.1 INTRODUCTION

In this chapter, the proposed framework for diagonal convection within the South Pacific Convergence Zone (SPCZ, Matthews, 2012) is explored in more detail and extended to offer a potential explanation for the diagonal orientation of the South

Atlantic Convergence Zone (SACZ) as well. The analysis will be based on the November-April period, in which the SPCZ and SACZ are well defined (figure 2.1a).

As discussed in section 1.1.2 and repeated here for clarity, the hypothesized framework of Matthews (2012) is based on transient Rossby wave propagation. Following the conceptual framework of Meehl *et al.* (2001), synoptic Rossby waves propagate on the atmospheric mean state that is set by processes on interannual and intraseasonal time scales (e.g. El Niño-Southern Oscillation, ENSO, and the Madden-Julian Oscillation, MJO). Rossby waves are limited to areas where $\overline{u} - c_x > 0$ and $\hat{\beta} > 0$, where u is the zonal wind component, c_x is the zonal phase speed and $\hat{\beta}$ is the meridional gradient of absolute vorticity (Yang & Hoskins, 1996). These waves propagate through jet regions that act as wave guides and are refracted towards latitudes with higher total wavenumber K (equation 1.7, Karoly, 1983; Hoskins & Ambrizzi, 1993). Figure 2.1c shows the November to April time mean geographical distribution of K at 200 hPa for Rossby waves with a typical zonal phase speed of 6 m s^{-1}. Rossby waves from the subtropical jet are refracted equatorward towards the westerly winds over the eastern equatorial Pacific. This 'westerly duct' allows for cross-equatorial Rossby wave propagation (Webster & Holton, 1982). Rossby waves from the jet southwest of Australia pass over the SPCZ area, Rossby waves refracting towards the westerly duct in the equatorial Atlantic pass over the SACZ area. During austral winter the westerly ducts disappear and equatorward refraction of midlatitude Rossby waves stops (Ambrizzi *et al.*, 1995); coincidentally the SPCZ and SACZ are much less pronounced.

These transient Rossby waves can directly trigger convection over the SPCZ and SACZ regions. Ahead of diagonally oriented cyclonic vorticity centres in the waves poleward flow is observed, quasi-geostrophic dynamics links this poleward flow with ascent and decreased static stability. The tropics with warm SSTs and high moisture causing conditionally unstable atmospheric conditions are sensitive to such forcing and deep convection and precipitation is triggered. A similar sequence of events has been observed to create transient convection in the Intertropical Convergence Zone (ITCZ) during austral summer (Kiladis & Weickmann, 1992a,b; Kiladis, 1998). In the SACZ a similar combination of an upper-tropospheric Rossby wave, a cyclone and convection is found (Liebmann *et al.*, 1999; Robertson & Mechoso, 2000).

In Matthews (2012) it is noted that the wave decays within a day after convection is

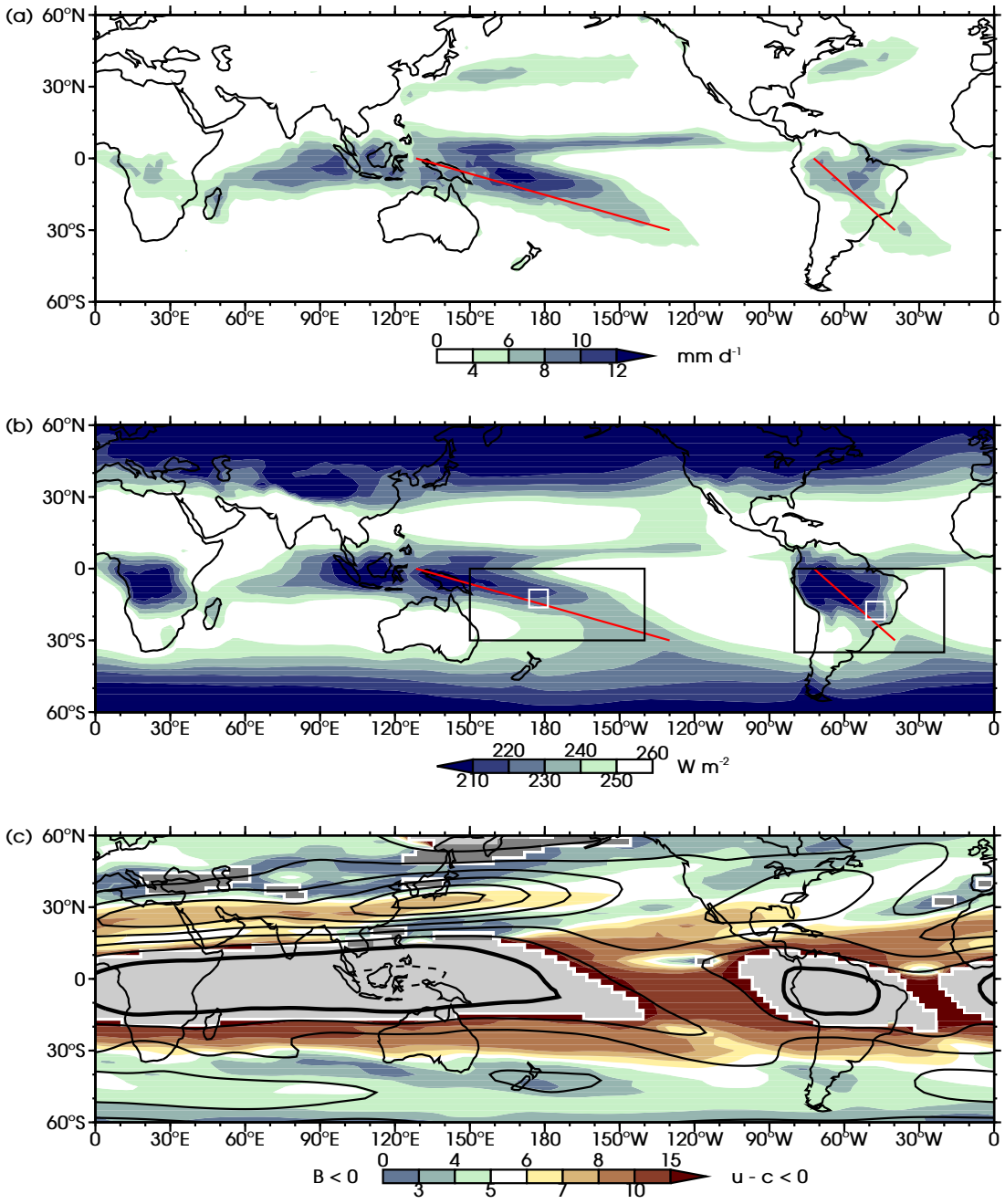

Figure 2.1: November to April time mean of (a) precipitation rate (mm d^{-1}, data source: CMAP), (b) OLR (W m^{-2}, data source: Interpolated OLR Dataset) and (c) 200 hPa total wavenumber for Rossby waves of phase speed 6 m s^{-1} in shaded colours (data source: NCEP-DOE reanalysis). Red diagonal lines in (a) and (b) indicate the position of the mean precipitation axis of the SPCZ and the SACZ. Small grey boxes in (b) indicate the areas of the power spectra in figure 2.2, large black boxes indicate the areas of the EOF analyses in figure 2.3. Contours in (c) show 200 hPa zonal wind (10 m s^{-1} contour interval, negative contours dashed, zero contour thickened). Light grey shading in (c) corresponds to areas of $\overline{u} - c_x < 0$, dark grey shading to $\hat{\beta} < 0$.

triggered. A hypothesis is proposed of a possible link and negative feedback between the convection and precipitation triggered by the transient wave and the subsequent decay of the wave. The diabatic heating released from condensation associated with the anomalous convection is substantial enough to force significant extra ascent and upper-tropospheric divergence. The divergence is a source of anticyclonic vorticity through vortex stretching. By means of a scale analysis it is shown that this anticyclonic vorticity tendency is large enough to remove the cyclone in the transient wave and dissipates the wave.

Here observational based data will be used to investigate the diagonal orientation of both convergence zones. The analysis of Matthews (2012) will be extended with a full vorticity budget, to quantify the strength of the proposed negative feedback mechanism. Rossby ray tracing techniques will be used to investigate Rossby wave propagation in the region. The analysis will be repeated for the SACZ. In the next section all observational data products that are used in this thesis will be discussed. In section 2.3 the temporal and spatial variability patterns for both the SPCZ and SACZ region are investigated. In section 2.4 the temporal evolution of transient waves are discussed. A framework for the diagonal SACZ is presented in section 2.5, followed by a framework for the diagonal SPCZ in section 2.6. The results are summarized in section 2.7 together with a discussion of their implications for global climate.

2.2 DATA

In tropical regions where precipitation is mostly from deep convection Outgoing Longwave Radiation (OLR) can be used as a proxy for precipitation (e.g. Lau & Chan, 1983; Janowiak & Arkin, 1991; Xie & Arkin, 1998). The annual cycle of temperature is small, therefore the strongest variations of OLR are the result of the presence of deep convective clouds (Salby, 2012). Figures 2.1a and 2.1b show time mean patterns of precipitation and OLR, respectively. In the tropics (approximately 30°S-30°N) more negative OLR values correspond to enhanced convection and more positive precipitation values; the SPCZ, SACZ and ITCZ can be identified in both panels. Higher OLR values are associated with reduced convection and negative precipitation anomalies, e.g. over the east Pacific dry zone. Polewards of 30°S/N OLR decreases due to decreasing surface and atmospheric temperatures.

For OLR the Interpolated OLR Dataset is used. These are estimates from the NOAA/NESDIS[1] polar-orbiting satellites. The interpolated dataset provides space and time interpolated data, the interpolation algorithm is described in Liebmann & Smith (1996). Data used are daily means from 1979 to 2013 on a 2.5°×2.5° grid.

Additionally, precipitation data from the Climate Prediction Center Merged Analysis of Precipitation (CMAP) project are used (Xie & Arkin, 1997). This is a precipitation product based on gauge observations from the Global Precipitation Climatology Center (GPCC, Rudolf *et al.*, 1994), five different satellite-based precipitation estimates and the NCEP-NCAR[2] re-analysis (Kalnay *et al.*, 1996). The satellite estimates included are the Geostationary Operational Environmental Satellite (GOES) Precipitation Index (Arkin & Meisner, 1987), the OLR Precipitation Index (OPI, Xie & Arkin, 1998), Spencer (Spencer, 1993), NOAA/NESDIS (Grody, 1991) and Chang (Wilheit *et al.*, 1991). Data are available on a 2.5°×2.5° grid as pentad values (five day means) from 1979 to 2008; for analysis purposes these have been linearly interpolated to daily values.

Horizontal wind and vertical velocity data are taken from the NCEP-Department of Energy (DOE) reanalysis (Kanamitsu *et al.*, 2002). Data were used on a 2.5°×2.5° grid with 12 vertical levels (1000-100 hPa) and covered the same period as was available for OLR: 1979-2013.[3]

The analysis in this chapter covers the months November to April when the SPCZ and SACZ are strongest. Anomalies were computed by removing the annual cycle from the data, the annual cycle was defined as the mean plus the first three (five for precipitation data) annual harmonics. To separate synoptic scale variability from variability at longer time scales a 20 day high-pass Lanczos filter (Duchon, 1979) was used.

2.3 PATTERNS OF VARIABILITY

Time series of daily OLR anomalies are defined in the centre of the SPCZ (175.0°-180.0°E, 15.0°-10.0°S, small grey box in figure 2.1b) and SACZ (50.0°-45.0°W,

[1] (US) National Oceanographic and Atmospheric Administration/National Environmental Satellite Data and Information System

[2] (US) National Centers for Environmental Predictions-National Climate Research Center

[3] The CMAP, interpolated OLR and NCEP Reanalysis data were provided by the NOAA/OAR/ESRL PSD, Boulder, Colorado, USA, from their web site at http://www.cdc.noaa.gov/.

20.0°-15.0°S). To assess the dominant modes of temporal variability in the SPCZ and SACZ, smoothed power spectra of these time series are shown in figure 2.2. Smoothing is based on a $L = 31$ point running mean. A red-noise theoretical background spectrum is added in black, based on the assumption that the time series were generated by a first-order Markov process and using the lag-1 autocorrelation coefficient ($r = 0.69$ for SPCZ and $r = 0.72$ for SACZ) of the time series (Wilks, 2006). The 95% confidence interval (dashed black line) was calculated by a chi-squared test using $2L$ degrees of freedom.

In the spectra of both the SPCZ and SACZ there is a large peak at the lowest frequencies, corresponding to ENSO at interannual timescales. At intraseasonal time scales variability is found only in the SPCZ, where there is a large peak at approximately 0.02 cycles day^{-1} or a 50 day period. This relates to the MJO, a 30-90 day coupled pattern in circulation and convection over the Indian and Pacific warm pool (Madden & Julian, 1971; Zhang, 2005) which has been shown to impact the SPCZ (Matthews *et al.*, 1996). Finally, at submonthly periods there are Rossby waves impacting both the SPCZ and the SACZ. This corresponds to peaks near 0.1 cycles day^{-1}, a 10 day period, and shorter time scales.

Spatial patterns of variability in the SPCZ and SACZ are found by means of Empirical Orthogonal Function (EOF) analysis. The EOFs are based on OLR anomalies over 34 austral summers (November to April, 1979-80 to 2012-13). The leading EOF patterns shown are significantly different from each other and following EOFs (North *et al.*, 1982). In figures 2.3a and 2.3b the patterns associated with the first two EOFs of the SPCZ and the SACZ are shown. The EOFs are calculated separately for the SPCZ and the SACZ domains, but are plotted on the same figure for convenience.

For the SPCZ all data within the box 150.0°-220.0°E, 30.0°S-0.0° (black box in figure 2.1b) are taken into account. The patterns found for the SPCZ variability are comparable to the patterns found by Matthews (2012), which were based on the same analysis but the data covered a shorter period of time. The first EOF accounts for 12.2% of the total variance and corresponds to what was named the 'southwestward shifted' mode. The pattern shows enhanced convection to the southwest of the mean precipitation axis and reduced convection to the northeast of the mean precipitation axis. The second EOF was described as the 'enhanced' mode. A similar pattern is found in this analysis (8.8% of the total variance), with enhanced convection on the

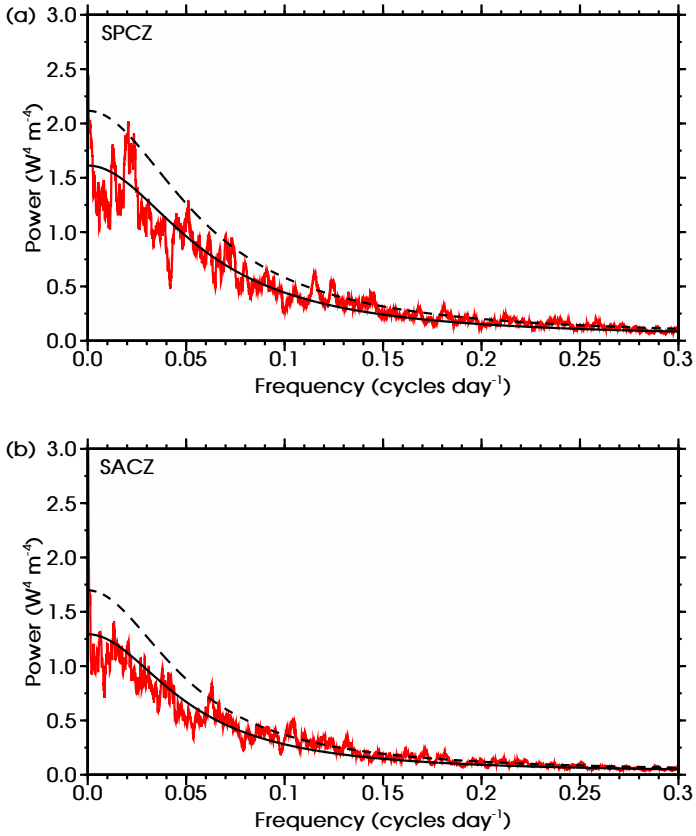

Figure 2.2: The 31-point smoothed power spectrum of daily OLR anomalies averaged over a box in the centre of the (a) SPCZ (175.0°-180.0°E, 15.0°-10.0°S) and the (b) SACZ (50.0°-45.0°W, 20.0°-15.0°S). The locations are indicated in figure 2.1b. A red noise background spectrum and its 95% confidence limit are shown in black lines; solid and dashed respectively.

mean precipitation axis and reduced convection on either side.

The patterns found over South America (SACZ region, box 80.0°−20.0°W, 35.0°S - 0.0°) are comparable to those of the SPCZ. The first EOF (10.1% of the total variance) shows enhanced convection to the southwest of the mean precipitation axis and reduced convection to the northeast, as described in the southwestward shifted mode. The second EOF (7.0% of the total variance) is the enhanced SACZ, with enhanced convection over the coastal and oceanic portion of the SACZ mean precipitation axis and reduced convection to the southwest and northeast. Note that in this case the largest variability is not located over the region of most intense precipitation, the Amazon, within the box.

Figures 2.3c and 2.3d show time series of the Principal Components (PCs) associated with the EOF patterns for the sample season of November 2000 to April 2001. These are daily amplitudes scaled to have standard deviation $\sigma = 1.0$. In

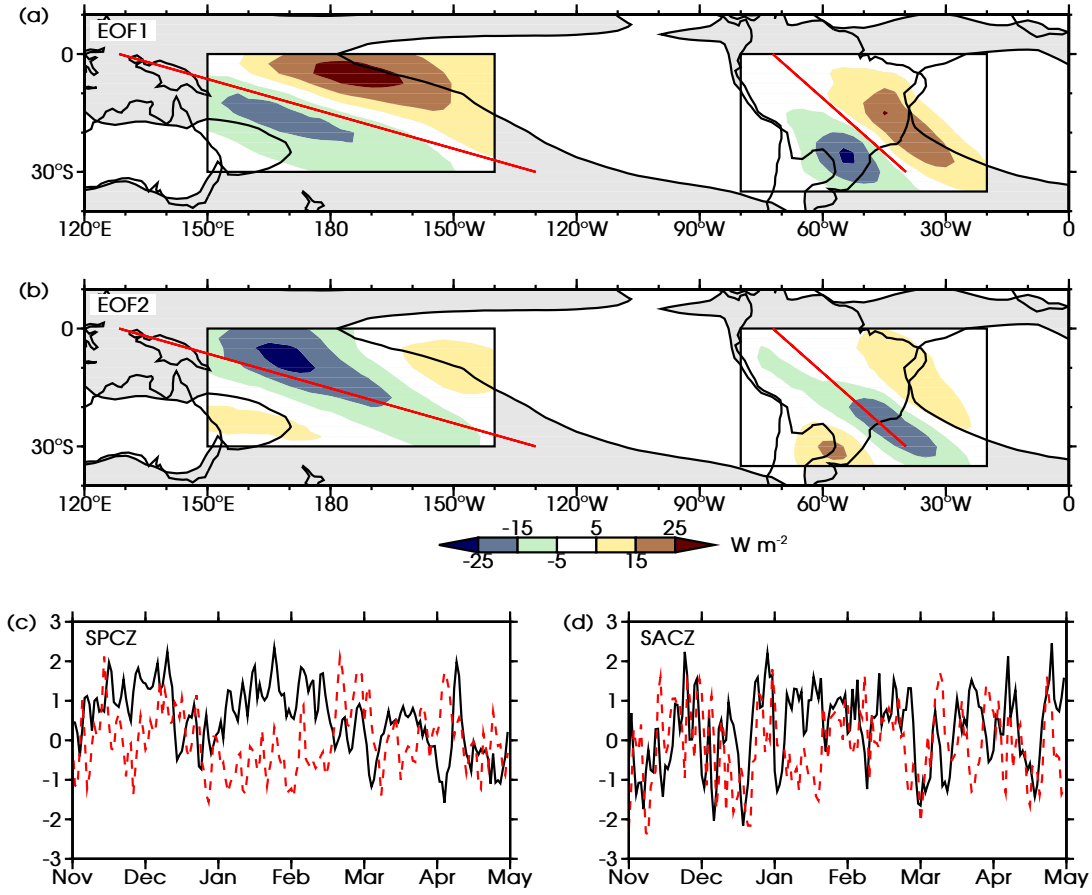

Figure 2.3: EOF patterns (a) 1 and (b) 2 in shaded colours (W m^{-2}) in the rectangular boxes, overlayed on the November to April time mean OLR field (grey shading is < 250 W m^{-2}, as in figure 2.1b). Red diagonal lines indicate the position of the mean precipitation axis of the SPCZ and the SACZ. Time series of the PCs associated with EOF 1 (black, solid line) and EOF 2 (red, dashed line) during November-April 2000-01 for the (c) SPCZ and (d) SACZ.

both SPCZ and SACZ the dominant mode of variability is on short, synoptic time scales. Variability on intraseasonal time scales is only visible in the SPCZ region as was concluded from the power spectra earlier. Lagged correlations between the time series of PC 1 and PC 2 in the SPCZ (calculated over all years) do not exceed $r = 0.02$ for lags up to a week. This is not significant at a $p = 95\%$ level according to the Pearson correlation coefficient statistical test. Therefore there is no evidence of a phase relationship between the patterns of EOF 1 and EOF 2, i.e. the southwestward shifted SPCZ mode does not develop into the enhanced SPCZ mode. For the SACZ there are weak significant cross-correlations from PC 1 to PC 2. For lags of one to three days these are $r = 0.320$, 0.271 and 0.130 respectively. This indicates that the OLR anomalies propagate towards the northeast, as the southwestward

shifted mode develops into the enhanced mode. Hence, both the SPCZ and SACZ experience variability at submonthly periods associated with Rossby wave activity. The spatial patterns associated with this variability are comparable for both regions, with respectively a southwestward shifted mode and an enhanced mode for EOFs 1 and 2. For the SPCZ these are similar to the patterns found in earlier analysis (Matthews, 2012).

Even though the variability patterns for the SPCZ and SACZ are similar, the temporal evolution is different. In the SPCZ there is no evidence of propagation from EOF 1 to EOF 2. In the SACZ significant lagged correlations are found from the time series of EOF 1 to EOF 2. The OLR anomalies of the southwestward shifted SACZ mode propagate northeastward in about 1-2 days to form the enhanced mode. In the next section these differences in temporal evolution will be discussed in more detail.

2.4 WAVE PROPAGATION

Events of the southwestward shifted SPCZ and SACZ modes are investigated by means of composite analysis. A 'convective event' is defined when two criteria are met:

1. PC 1 > 1.0 σ and
2. PC 1 is a maximum relative to five days before and five days after the event.

In total 204 months were taken into account (November-April, 1979-80 to 2012-13). In this period there were 197 SPCZ convective events and 361 SACZ convective events based on the above criteria. Composites were computed by taking the mean of a field over all event days.

Figure 2.4a shows the SPCZ composites of OLR, 200 hPa vorticity and 200 hPa wind anomalies; negative OLR anomalies (enhanced convection) lie to the southwest of the mean precipitation axis and positive OLR anomalies (reduced convection) to the northeast. More enhanced convection is found over the maritime continent. The vorticity anomalies form a wave-like structure of cyclones (negative anomalies in the Southern Hemisphere) and anticyclones (positive anomalies). This is the Rossby wave train propagating from the subtropical jet stream towards the equatorial westerly duct which has been related to transient convection in the SPCZ (e.g Kiladis & Weickmann, 1992a; Widlansky *et al.*, 2011). Deep anomalous convection is found southwest of the mean precipitation axis, in the same location as the poleward,

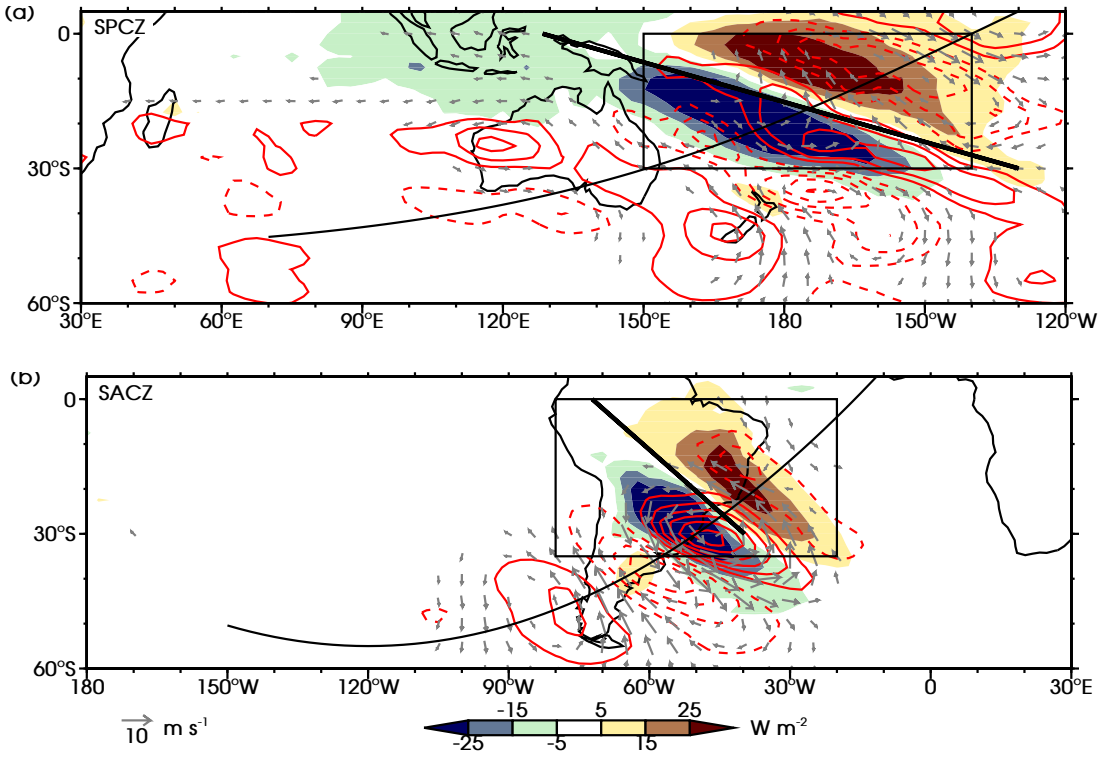

Figure 2.4: Composite anomalies of OLR in shaded colours (W m^{-2}), 200 hPa vorticity in red contours (3×10^{-6} s^{-1} contour interval for SPCZ (a) and 6×10^{-6} s^{-1} for SACZ (b), zero contour omitted, negative contours dashed) and 200 hPa wind in vectors (m s^{-1}, reference vector bottom left). The rectangle indicates the EOF region, the thick diagonal line the mean precipitation axis and the curved line an approximate wave propagation path.

ascending flow ahead of a cyclonic anomaly. Northeast of the mean precipitation axis equatorward, descending flow ahead of an anticyclonic anomaly coincides with reduced convection. The precipitation anomalies associated with this pattern (not shown) are +5.3 mm d^{-1} southwest of the mean precipitation axis and −6.3 mm d^{-1} northeast of the mean precipitation axis.

Over South America the composite mean shows a similar combination of events (figure 2.4b). A Rossby wave train propagates from the Pacific towards the Atlantic westerly duct, with vorticity anomalies that are stronger than in the SPCZ region (note the different red contour intervals in the figures). Ahead of the cyclonic vorticity anomaly poleward wind is associated with convection southwest of the mean precipitation axis. To the northeast and southwest of this region, anticyclonic vorticity centers and equatorward flow weaken convection. The associated precipitation anomalies are weaker than in the SPCZ region: in the enhanced convection an additional 2.4 mm d^{-1} of precipitation is generated, the reduced convection

decreases precipitation by 2.3 mm d^{-1}. This is despite similar sized OLR anomalies and is because mean precipitation in the SACZ is less than in the SPCZ (see figure 2.1a).

In the next two sections the SPCZ and SACZ will be discussed seperately. Analysis has shown the mechanism forcing the SACZ is simpler than the mechanism for the SPCZ, therefore the SACZ will be discussed before the SPCZ. Based on the lagged composite analysis the temporal evolution of the equatorward propagating wave and the convection will be investigated. To separate the synoptic scale variability of interest from variability at longer time scales (e.g. MJO and ENSO) all subsequent data have been high-pass filtered before the composites are computed. See section 2.2 for details.

2.5 A FRAMEWORK FOR DIAGONAL SACZ DEVELOPMENT

2.5.1 OBSERVATIONAL OVERVIEW

Lagged composites of the days before and after the selected convective events give information on the temporal evolution of the wave train and convection anomalies (figure 2.5). The Rossby wave train in the SACZ region can be tracked back into the central Pacific Ocean. In the days leading up to the convective event quasi-circular vorticity anomalies propagate eastward. The vorticity anomalies are refracted equatorwards toward the upper-tropospheric mean westerlies over the equatorial Atlantic (figure 2.1c). In this process the circular vorticity centres are deformed and obtain a northwest-southeast diagonal orientation.

In front of the cyclonic anomaly, anomalous poleward wind is found. Following quasi-geostrophic dynamics poleward wind is associated with ascent and reduced static stability. In the conditionally unstable tropical atmosphere this could provide the trigger to overcome the convective inhibition and start deep convection 2 days before the main convective event. This region of enhanced convection (negative OLR anomaly) travels with the wave along the propagation path and remains ahead of the cyclone at all times, intensifying with time. The opposite mechanism gives reduced convection ahead of anticyclonic vorticity. On the day of the convective event (figure 2.5b) the vorticity anomalies lie parallel to the mean SACZ precipitation axis.

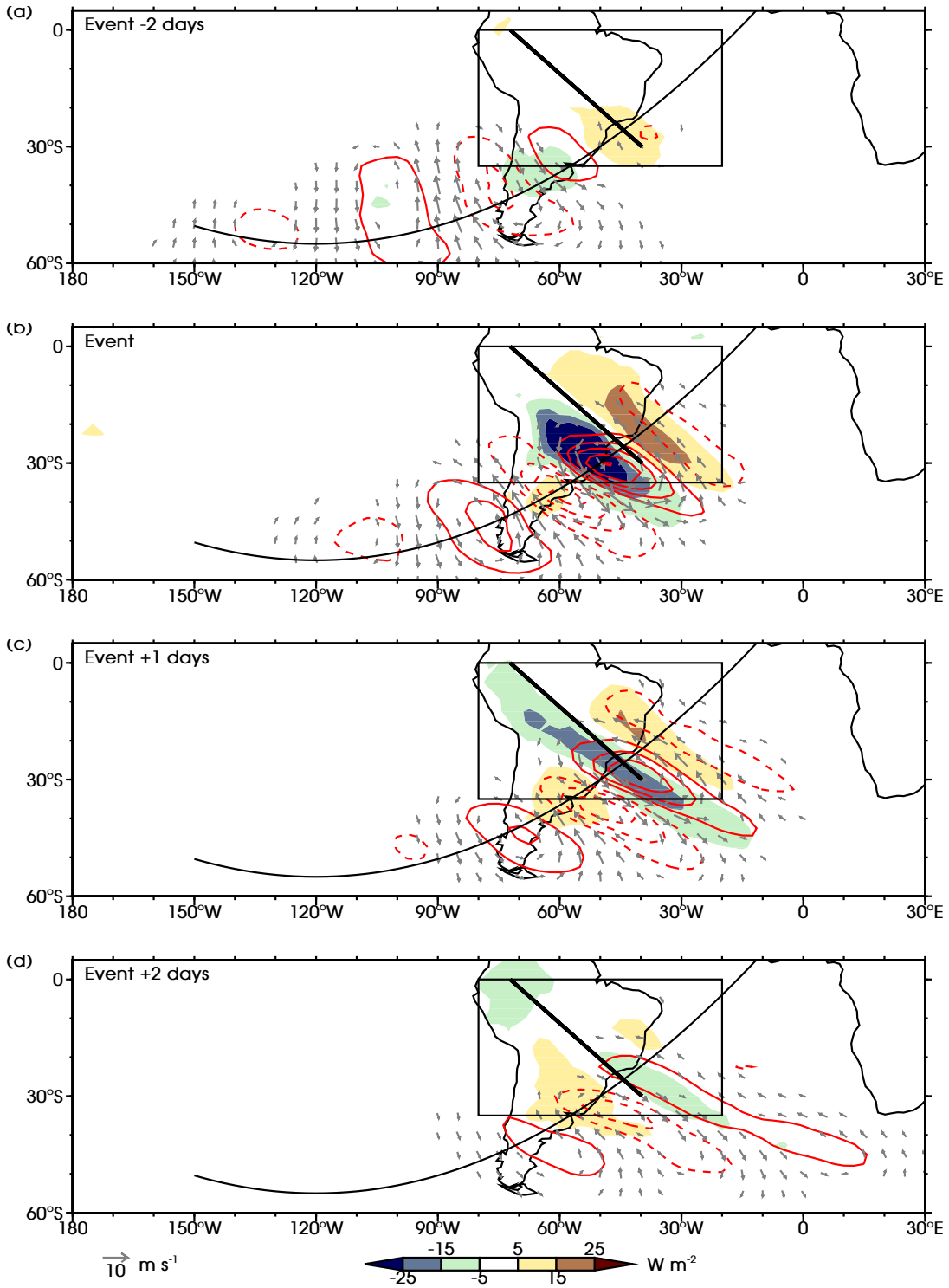

Figure 2.5: As figure 2.4b, but now for lagged composites of 20 day high-pass filtered data. Time lags shown: (a) event −2 days, (b) event, (c) event +1 days and (d) event +2 days.

By design of the composites the convection peaks at the event date, southwest of the mean precipitation axis. The precipitation rate that day (not shown) is 1.1 mm d^{-1}. A day after the event the convective anomaly is located at the mean precipitation axis and reflects the enhanced SACZ mode. This is in agreement with previously found cross-correlations between the PCs of EOFs 1 and 2 (section 2.3). At event +2 days the convection has weakened and now lies to the northeast of the mean precipitation axis, the pattern resembles a weak negative southwestward shifted mode.

2.5.2 DEVELOPMENT OF THE DIAGONAL ORIENTATION FROM ROSSBY WAVE DYNAMICS

Rossby wave propagation from the subtropics towards the equator and coincident deformation of the vorticity centres is a core mechanism in the development of the diagonal band of convection forced along the SACZ. Over the central Pacific the vorticity centres inititally have an approximately circular shape; a northwest-southeast orientation is subsequently developed during their travel eastward and equatorward (e.g. figure 2.5b). Here, two different models are used to test possible mechanisms for this deformation. First, the role of simple horizontal advection by the mean background wind ($\overline{u}$,$\overline{v}$, with v the meridional wind component) is determined. Thirty points in a circle around 105°W, 45°S form a circular patch that models a vorticity centre in the jet (figure 2.6a). Vorticity is advected only, there is no refraction by a Rossby wave mechanism. The advection and changing location of the tracer in time has been computed by means of a fourth order Runge-Kutta scheme with a time step of 60 seconds. The plotted daily location of the vorticity tracer shows that in time the circular shape does evolve into a diagonally orientated shape due to shear on the northern side of the jet. There is however no discernible equatorward propagation due to the weak meridional wind.

The second model demonstrates the role of nondivergent barotropic Rossby wave dynamics. The ray-tracing technique of Karoly (1983) for low-frequency Rossby waves is applied; scale separation between waves and mean flow is assumed. Rossby waves with initial zonal wavenumber $k_0 = 1.2 \times 10^{-6}$ m^{-1} and meridional wavenumber $l_0 = 6.9 \times 10^{-7}$ m^{-1} are initiated at $X_0 = 105°W$ and six different latitudes across the jet between 35°S and 60°S (figure 2.6b). The change of the ray position and

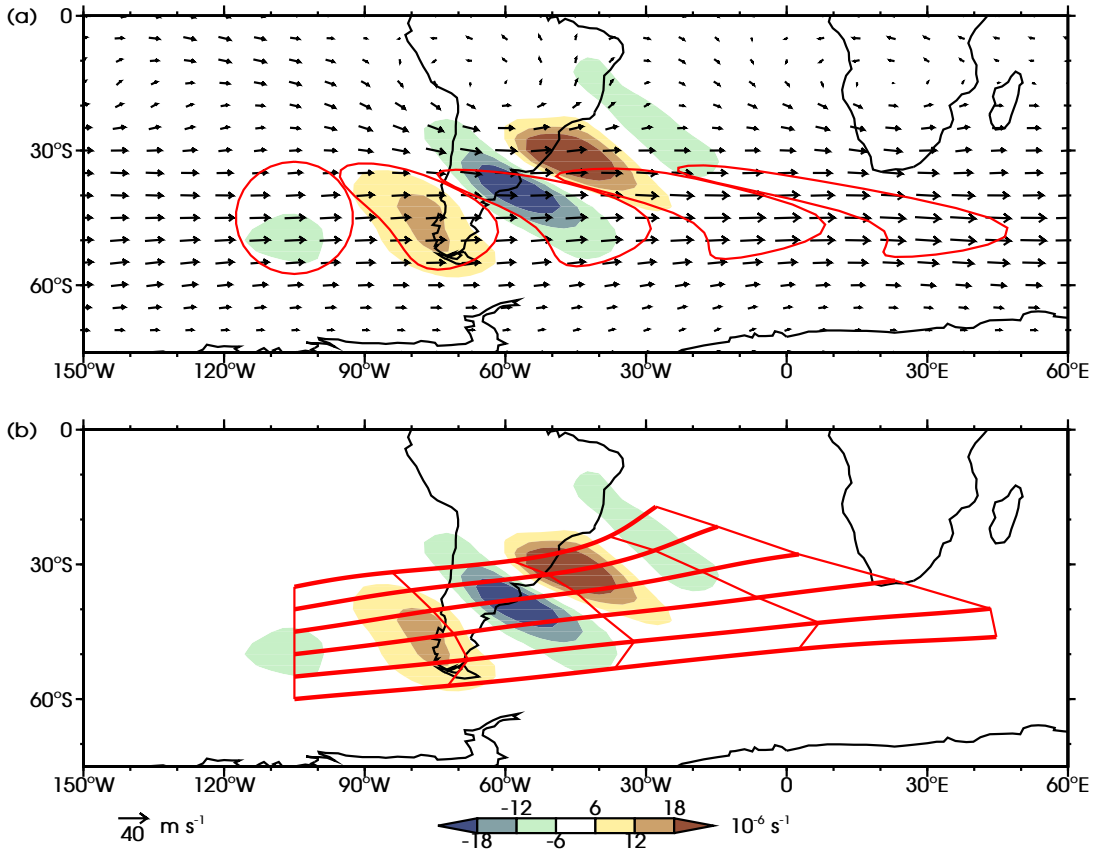

Figure 2.6: Two different wave propagation models for the SACZ. (a) Horizontal advection of a tracer by the 200 hPa November-April mean wind, tracer positions for consecutive days in red contours, wind in vectors (m s^{-1}, reference vector bottom left). (b) Rossby ray propagation on the 200 hPa November-April mean wind, thicker red lines show ray paths, thinner red lines connect these at daily intervals. Vorticity anomalies as in figure 2.5b in shaded colours (s^{-1}).

wavenumbers are integrated forward in time by the same Runge-Kutta scheme as in the first model. From their initial position the Rossby rays take about two days to reach the SACZ area, during this time they become aligned with the vorticity centres that were found in the composite analysis. In contrast to the advection-only model, the meridional movement is strong enough to show clear equatorward propagation of the rays initiated on the northern edge of the jet. Once convection is triggered the nondivergent, dry model becomes a less valid description of the situation. However, during the approach to the SACZ region the Rossby waves are dry and as a first approximation this simple model does show that barotropic Rossby wave dynamics can create the elongated, northwest-southeast oriented vorticity anomalies and equatorward propagation, that lead to SACZ convection.

2.5.3 VERTICAL STRUCTURE

Although barotropic, non-divergent Rossby wave circulations can account for the diagonal orientation of the vorticity anomalies that force the SACZ, the baroclinic component of these circulations and their associated vertical motion then leads to triggering of convection. The vertical structure of the wave train is shown in figure 2.7a, which shows a section along the approximate wave path at the day of the event (curved black line in figure 2.5b). The vorticity anomalies are strongest at 200 hPa and extend down to the surface in the SACZ region (the vertical line denotes the position of the mean precipitation axis). The pressure velocity anomalies are approximately in quadrature with the vorticity anomalies. Rising motions are found ahead of the cyclonic anomaly west of the mean precipitation axis, descending motions in front of anticyclonic anomalies east of the mean precipitation axis. The strong rising motion is accompanied by convergence in the lower-troposphere and divergence in the upper-troposphere. The anticyclones up- and downstream of the cyclone are weaker but do give downward motion. Therefore convection is inhibited and upper-level convergence is found ahead of those.

The temporal development of the wave train and the associated convection anomaly along the curved propagation path is shown in a Hovmöller diagram (figure 2.7b). Grey dashed lines indicate an approximate group velocity based on the Rossby ray tracing results. The main region of vorticity activity lies within this group velocity envelope, consistent with the wave being governed by Rossby wave dynamics. The effects of phase and group velocity are visible. The leading edge of the wave packet propagates at the faster group velocity of approximately 29 m s^{-1} (dashed grey line in figure 2.7b passing through 100°W, lag -5 days). Individual vorticity anomalies are initiated at this leading edge, e.g. the anticyclonic positive vorticity anomaly that begins around 110°W, lag -5 days (yellow shading). These vorticity anomalies propagate at the slower phase speed of approximately 7 m s^{-1}, increasing in amplitude as the centre of the energy envelope that defines the wave packet passes through them. Finally the trailing edge of the wave packet passes through, also at the group velocity of 29 m s^{-1}. At this point, the individual vorticity anomalies decay (around 65°W, lag +2 days for the positive vorticity anomaly) and eventually disappear.

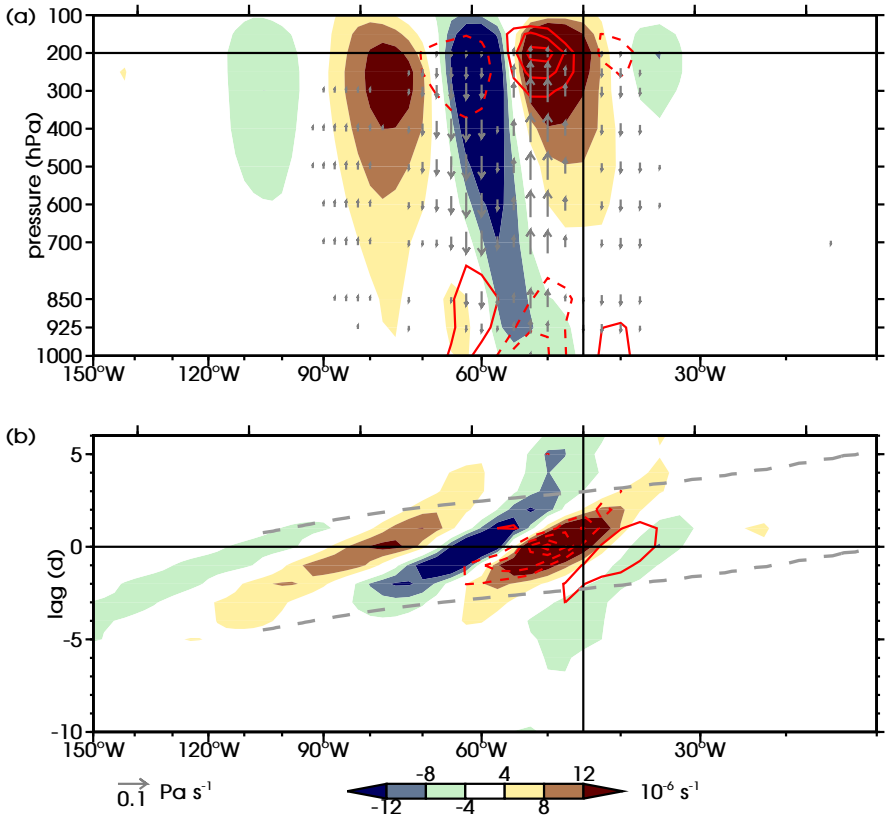

Figure 2.7: (a) Vertical cross section at the convective event along the curved propagation path (curved line in figure 2.5b), vorticity in shaded colours (s^{-1}), divergence in red contours (2×10^{-6} s^{-1} contour interval, zero contour omitted, negative contours dashed) and pressure velocity in vectors (Pa s^{-1}, reference vector bottom left). (b) Hovmöller diagram of lagged composites along the curved propagation path. 200 hPa vorticity in shaded colours (s^{-1}) and OLR in red contours (10 W m^{-2} contour interval, zero contour omitted, negative contours dashed). Grey dashed lines indicate an approximate group wave speed, taken from figure 2.6b. All data are 20 day high-pass filtered. Horizontal axes are irregular longitude (bottom) or regular distance (top, 2000 km intervals) along the path. Vertical line indicates the position of the mean SACZ precipitation axis.

Two days before the event the cyclonic anomaly triggers convection. Together, the vorticity and convection anomaly propagate onwards. Two days after the event both anomalies weaken and the convective anomaly disappears.

A hypothesis of a possible link between wave propagation and the convection triggered by the wave was proposed in Matthews (2012): ascent in the Rossby wave triggers convection and precipitation. The diabatic heating released is substantial and enhances the ascent and upper-level divergence (figure 2.7a). Divergence is a source of anticyclonic vorticity. As discussed before, the convection signal is in quadrature with the vorticity anomalies in the wave, with enhanced convection

ahead of a cyclonic anomaly. The eastward propagating cyclone that triggered convection therefore encounters the generated anticyclonic vorticity when it moves along the wave path. The relative size of these two opposite vorticity terms ultimately determines whether or not the Rossby wave propagation can continue downstream of the triggered convection.

2.5.4 VORTICITY BUDGET

A quantitative analysis of the size of the different vorticity influences is needed to find the strength of the proposed negative feedback between wave dynamics and diabatic heating. Therefore all terms in the vorticity equation have been computed:

$$\underbrace{\frac{\partial \zeta}{\partial t}}_{I} = \underbrace{-u\frac{\partial \zeta}{\partial x} - v\frac{\partial \zeta}{\partial y}}_{II} \quad \underbrace{-\omega\frac{\partial \zeta}{\partial p}}_{III} \quad \underbrace{-fD - \zeta D}_{IV} \quad \underbrace{-\beta v}_{V} \quad \underbrace{-\frac{\partial \omega}{\partial x}\frac{\partial v}{\partial p} + \frac{\partial \omega}{\partial y}\frac{\partial u}{\partial p}}_{VI} \tag{2.1}$$

where ζ is relative vorticity, t is time, x and y are the horizontal axes in the eastward and northward direction, respectively, ω is pressure velocity, p is pressure, f is the Coriolis parameter or planetary vorticity, D is divergence and $\beta = \frac{df}{dy}$ is the meridional gradient of planetary vorticity. (Holton, 2004, pp. 103). The relative vorticity tendency (term I) is the result of the sum of the effects of horizontal (term II) and vertical (term III) advection of relative vorticity, vortex stretching (term IV), meridional advection of planetary vorticity (term V) and the tilting and twisting terms (term VI). Using 6 hourly NCEP-DOE reanalysis data at three levels (150, 200, 250 hPa) all terms in the vorticity equation have been computed at the 200 hPa level. Partial derivatives in time and pressure have been computed using centered differences. The residual balance from this computation is smaller than the main terms of interest and does not show a large scale pattern. For reference the residual will be plotted alongside the other terms.

In figure 2.8 composites of the separate vorticity budget terms are shown for the day of the convective event. The budget is dominated by the horizontal advection terms and the vortex stretching terms. Horizontal advection (term II) of the wave pattern by both transient and background winds is the driving force for forward movement. The signal of horizontal advection is in quadrature with the wave pattern. Total horizontal advection of the cyclonic anomaly is partly balanced by the

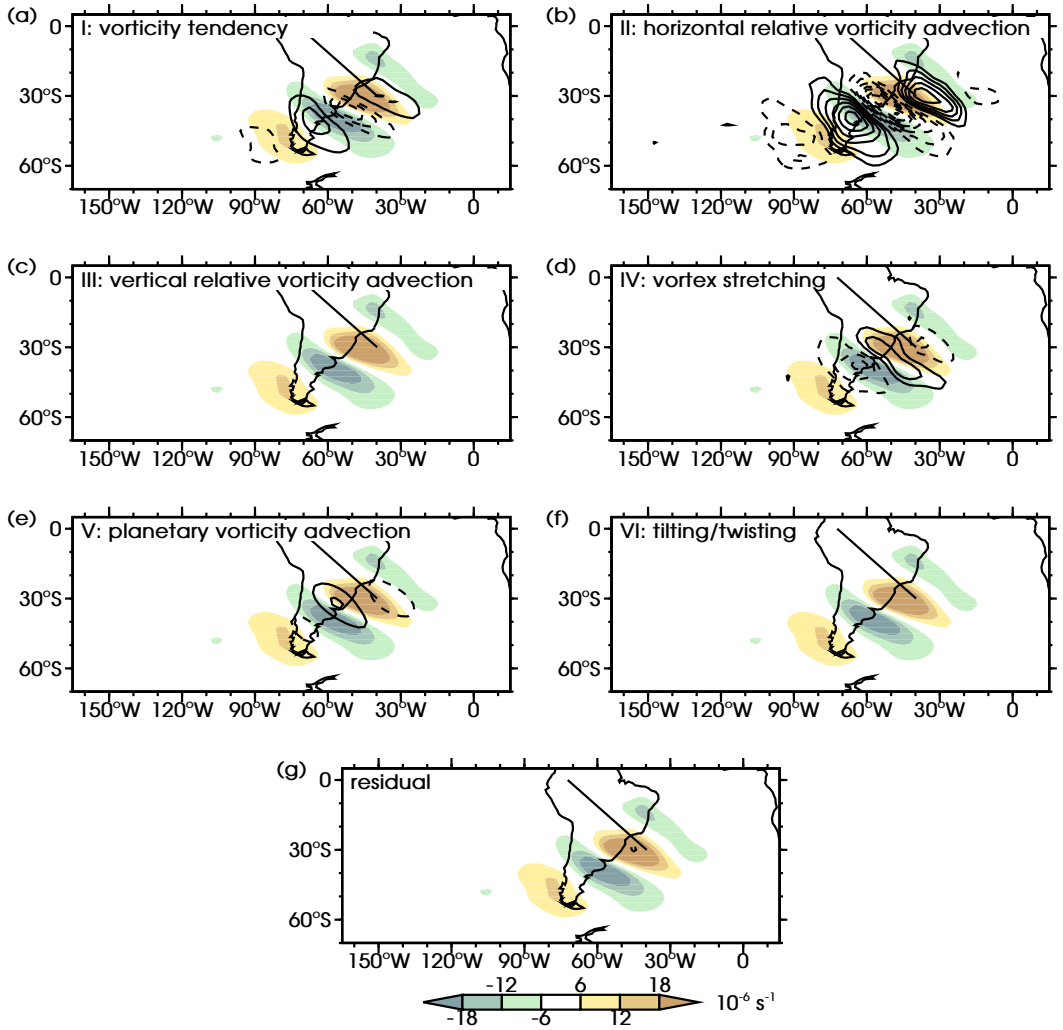

Figure 2.8: Composites of all terms in the full vorticity budget (equation 2.1) for the SACZ at 200 hPa in contours (1×10^{-5} s^{-1} d^{-1} contour interval, negative contours dashed, zero contour omitted) and vorticity anomalies as in figure 2.4b in shaded colours (s^{-1}). The diagonal line indicates the position of the mean precipitation axis.

vortex stretching term (term IV) which has its maximum ahead of the cyclone where convection is triggered. This is the location of rising motion, enhanced convection and upper-level divergence forced by the wave (figure 2.7a). The divergent outflow of air in the upper-troposphere is a source of anticyclonic vorticity. The vorticity tendency (term I) is in quadrature with the vorticity pattern (quarter cycle ahead of the vorticity anomaly), resulting in continued propagation of the wave pattern.

The same composite analysis has been done for the enhanced SACZ mode (EOF 2, 397 selected events). The interaction between transient Rossby waves and convection is similar. The SACZ in its climatological position can be seen as the sum of all

individual southwestward shifted and enhanced SACZ events. The atmospheric basic state gives rise to the equatorward refraction of Rossby waves that eventually leads to diagonal bands of deep convection and precipitation.

2.6 A FRAMEWORK FOR DIAGONAL SPCZ DEVELOPMENT

A similar analysis, as undertaken for the SACZ, is presented here for the SPCZ. In figure 2.9 lagged composites of the propagating wave and convection anomalies are shown. A wave train can be tracked to originate in the Indian Ocean. The vorticity anomalies are refracted equatorwards toward the upper-tropospheric mean westerlies over the equatorial Pacific (figure 2.1c). As was found in the SACZ originally quasi-circular vorticity centres get elongated in the northwest-southeast direction. On the day of the convective event the vorticity centres lie parallel to the mean SPCZ precipitation axis. Ahead of the cyclonic anomaly poleward ascending wind triggers deep convection in the tropical conditionally unstable atmosphere. The anomalous precipitation from this deep convection is maximum +1.9 mm d^{-1}. Northeast of the mean precipitation axis a combination of anticyclonic vorticity and equatorward descending flow results in a diagonal band of reduced convection. Two days after the event the OLR anomalies have mostly vanished. The wave train has not propagated further equatorward, downstream of the SPCZ region the vorticity anomalies have disappeared. This is in contrast to the SACZ region where the convective anomalies travelled with the wave train and passed over the mean precipitation axis.

In the unfiltered composite of the SPCZ (figure 2.4a) there is enhanced convection over the maritime continent. This signal has disappeared (figure 2.9c) in the composites using 20 day high-pass filtered data because it is forced at longer time scales than the synoptic time scales at which the diagonal SPCZ convection is forced.

As was done for the SACZ, the role of horizontal advection in the wave propagation is investigated by means of a simple model. A circular patch centered around 50°E, 45°S is advected by the November-April mean 200 hPa wind (figure 2.10a). As observed in the composites (figure 2.9b) the originally circular patch deforms and becomes elongated in the northwest-southeast direction. However, the observed equatorward propagation is not found.

This equatorward refraction is found when non-divergent barotropic Rossby wave

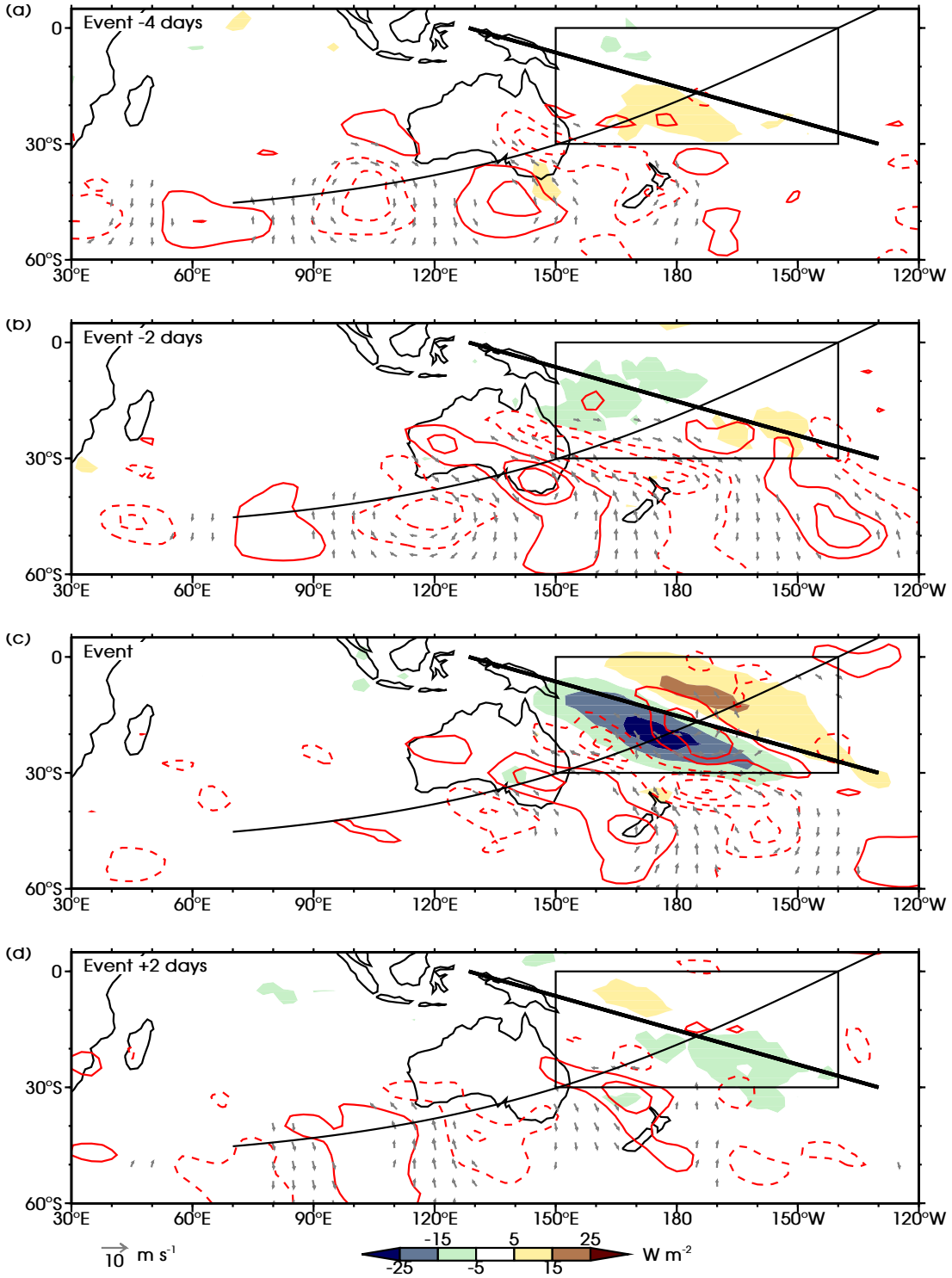

Figure 2.9: As figure 2.4a, but now lagged composites of 20 day high-pass filtered data. Time lags shown: (a) event −4 days, (b) event −2 days, (c) event and (d) event +2 days.

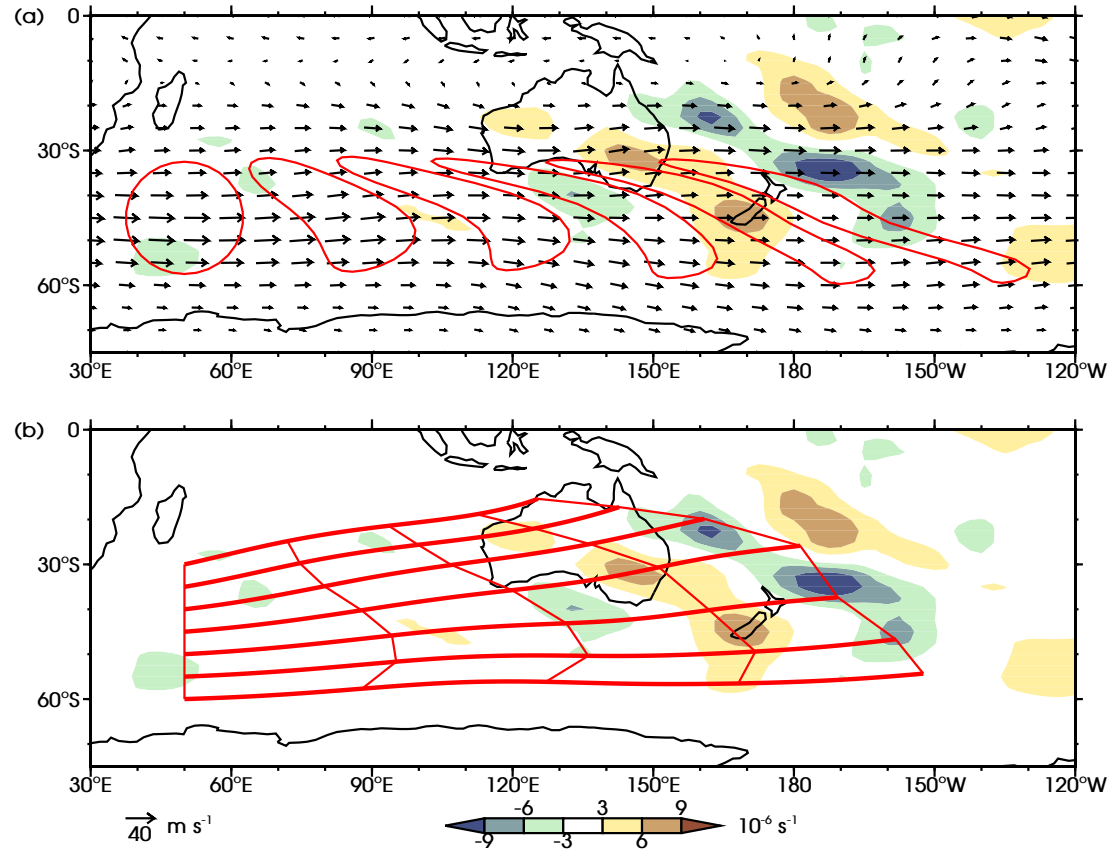

Figure 2.10: As figure 2.6 but now for SPCZ.

dynamics are added to the model (figure 2.10b). Rossby rays starting at 50°E, across seven different latitudes (30°S-60°S) with initial wavenumbers $k_0 = 1.2 \times 10^{-6}$ m^{-1} and $l_0 = 4.4 \times 10^{-7}$ m^{-1} take about four days to propagate to the SPCZ region and acquire the diagonal orientation found in the composite analysis. The ray tracing is stopped there, as this is where the Rossby wave in the composites disappears. The mechanisms involved in setting up the diagonal vorticity centres at the base of the diagonal convection are similar for the SACZ and the SPCZ. Vorticity centres become elongated with a northwest-southeast tilt due to the zonal wind shear at the equatorward flank of the jet stream. Equatorward propagation is primarily due to refraction.

The vertical section (figure 2.11a) through the wave shows a similar structure to the SACZ wave. The wave train of cyclones and anticyclones is strongest at about 200 hPa, with the main cyclonic anomaly reaching to the surface. Ahead of the cyclone there are strong rising motions which are accompanied by convergence at the surface and divergence aloft. The anticyclone upstream of the cyclone gives

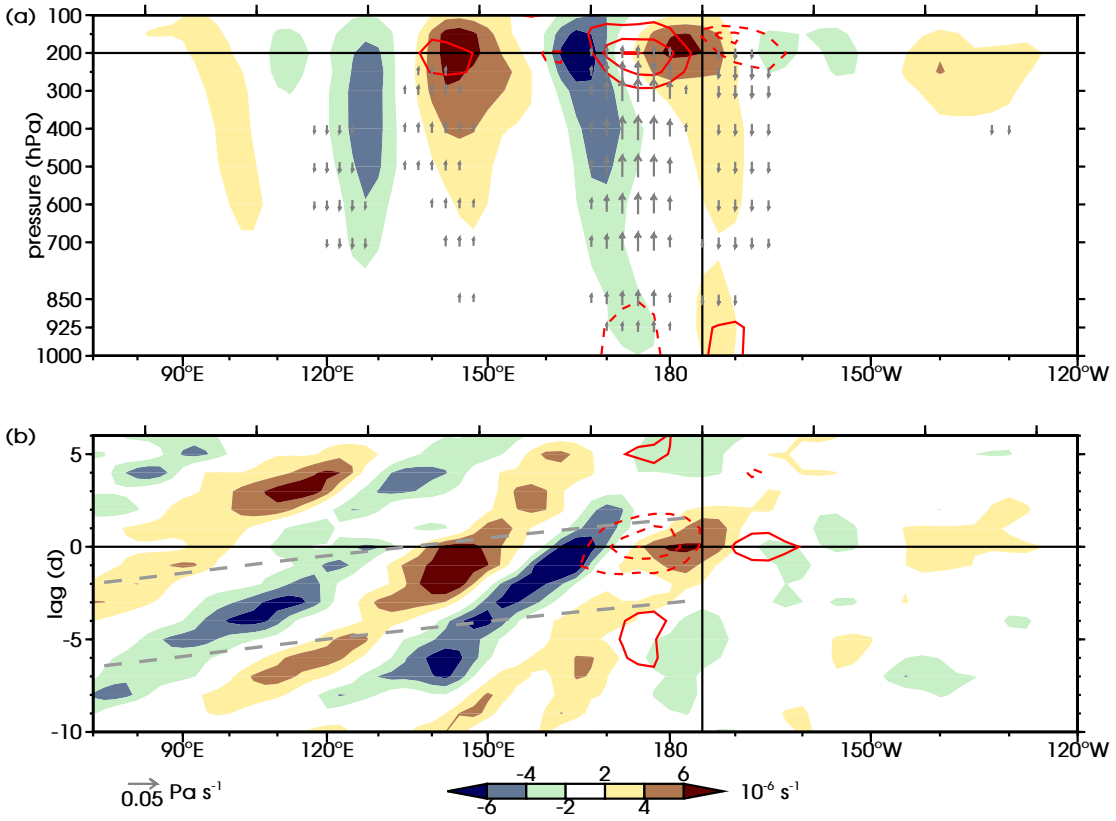

Figure 2.11: As figure 2.7, but now for the curved propagation path of the SPCZ (figure 2.9). Notice different vector scaling, colourbar and contour interval for divergence (1×10^{-6} s^{-1}).

downward motion, therefore convection is inhibited and upper-level convergence is found ahead of this anticyclone.

The propagation of vorticity and OLR anomalies are shown in a Hovmöller diagram (figure 2.11b). West of the mean precipitation axis and before the convective event there is clear eastward propagation of the vorticity anomalies at approximately 6 m s^{-1}. The grey dashed diagonal lines show the approximate group velocity which is derived from the ray paths in figure 2.10b. Again, this energy envelope confines the wave packet. Near the mean precipitation axis shortlived OLR anomalies appear, with enhanced convection ahead of the cyclonic vorticity centre and reduced convection ahead of the anticyclonic vorticity. These convective anomalies do not propagate along the wave path and the vorticity anomalies do not propagate downstream of the mean SPCZ precipitation axis. Instead, the Rossby wave loses coherence and decays at the convective event.

It seems the SPCZ area forms a barrier for the Rossby waves, this is different from the wave propagation that was found in the SACZ area. The feedback between wave

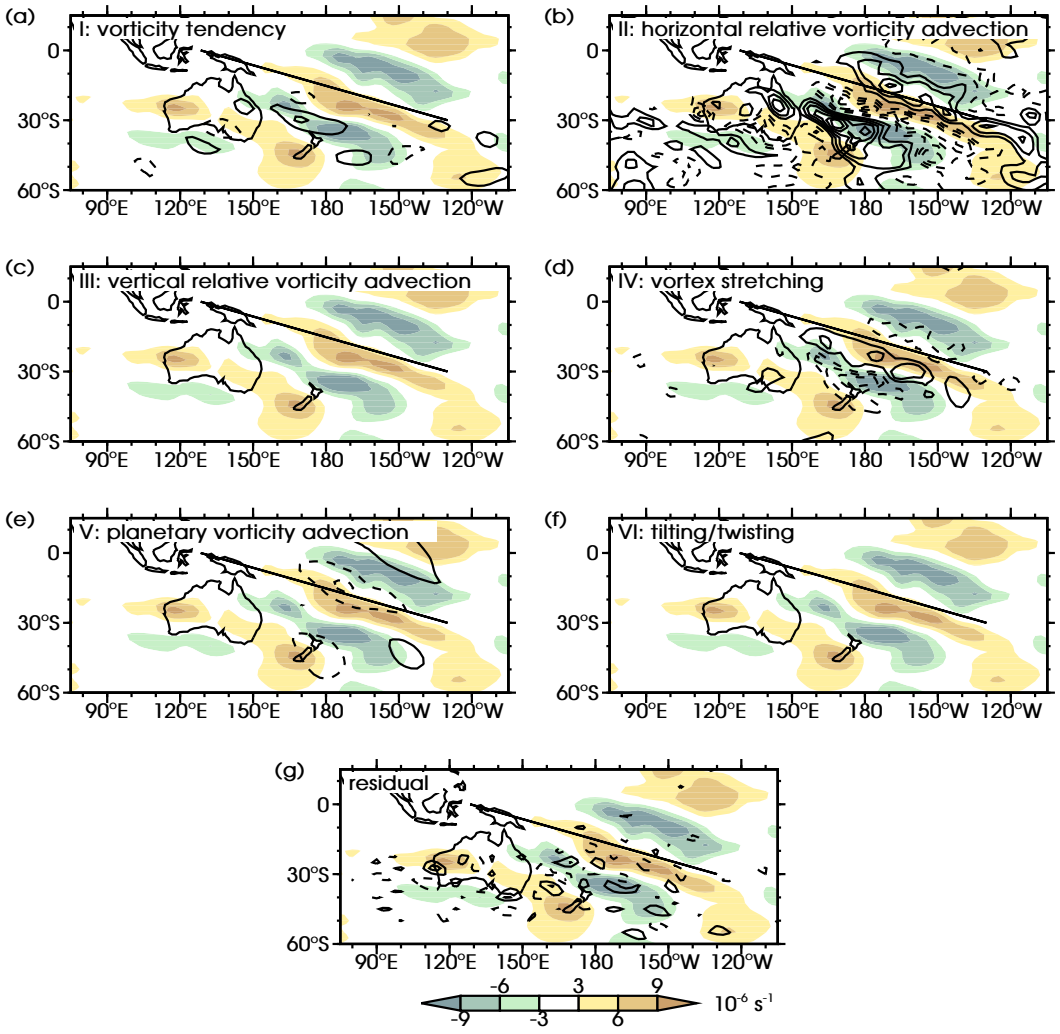

Figure 2.12: As figure 2.8 but now for the SPCZ. Note different contour interval (0.5×10^{-5} s^{-1} d^{-1}).

propagation and diabatic heating from triggered deep convection must therefore be different. Quantitative evidence for the relative strength of the negative feedback is provided by the computation of the vorticity budget (equation 2.1). In figure 2.12 all separate terms and the residual are plotted for the day of the convective event. In the SACZ region horizontal advection of relative vorticity was dominant and forced continued propagation of the wave. Also in the SPCZ region the horizontal advection term (term II) shows northeastward propagation of the wave pattern, ahead of the cyclone negative vorticity tendency is found. However, vortex stretching (term IV) largely cancels this propagation. The anticyclonic tendency ahead of the cyclone relates to upper-troposheric divergence found ahead of the cyclonic anomaly (figure 2.11a). The sum of the two effects, the vorticity tendency (term I), is close to

zero so the cyclone does not move. This is the key SACZ/SPCZ difference. Meanwhile, the upstream anticyclonic anomaly does move forward into the stationary cyclonic anomaly. The negative feedback between Rossby wave and transient convection stops and dissipates the Rossby wave.

As in the SACZ region the diagonal convection band of the SPCZ is forced by equatorward propagating Rossby waves originating in the southern jet. In contrast to the SACZ the latent heat released in the convection is strong enough to stop the wave propagation. The vorticity centres in the SPCZ wave train are much weaker than those of the wave train in the SACZ region. As a result the forced poleward wind and upward motion are also weaker in the SPCZ. However, the SPCZ precipitation that is induced is, in contrast, greater than in the SACZ. The additional latent heat from condensation is therefore relatively more important and the additional upper-tropospheric divergence and anticyclonic vorticity tendency it generates is strong enough to dissipate the wave *in situ*. This is consistent with the non-significant cross-correlations that were found between the PC time series of EOF 1 and 2 for the SPCZ.

2.7 DISCUSSION

Observationally based data products have been used to investigate patterns of variability in the SPCZ and SACZ regions, the focus has been on variability at synoptic time scales. Two spatial patterns of variability have been found in both the SPCZ and SACZ regions. The main mode is a 'southwestward shifted' convection pattern, the second mode is an 'enhanced' convection pattern. The EOF patterns and associated PC time series have been used for composite analysis to find the temporal development of these modes.

The chain of events leading to a diagonal precipitation band in the SPCZ region is shown in schematic form in figure 2.13. A wave train originating in the southern subtropical jet refracts northeastward towards the east Pacific equatorial westerly duct (1). The originally quasi-circular vorticity anomalies get an elongated diagonal structure due to shear on the northern edge of the jet. Ray tracing techniques have shown dry non-divergent barotropic Rossby dynamics provides the equatorward propagation, as has been suggested by Hoskins & Ambrizzi (1993). Ahead of a cyclonic vorticity anomaly poleward wind ascends and triggers convection (2). This

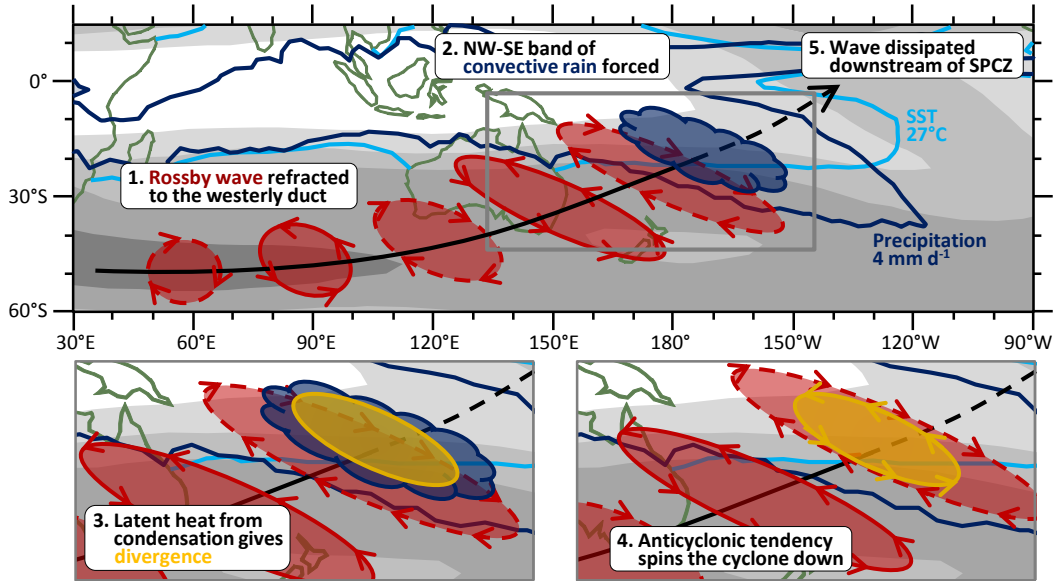

Figure 2.13: Schematic of mechanism for the development of a diagonal SPCZ. A Rossby wave train from the southern tropical jet is refracted towards the equatorial Pacific westerly duct (1). Originally quasi-circular vorticity centres deform to have a northwest-southeast elongation. Ahead of a cyclonic vorticity anomaly, poleward wind is associated with destabilisation and ascending motions that trigger deep convection in a diagonal band (2). Latent heat from condensation gives additional ascent and upper-tropospheric divergence (3). This leads to an anticyclonic vorticity tendency through vortex stretching ahead of the cyclone, however continued horizontal propagation of the cyclone brings it over this area and spins the cyclone down (4). The cyclone is dissipated *in situ* and hence Rossby wave propagation stops in the SPCZ area (5).

convection anomaly has a northwest-southeast orientation similar to the vorticity anomalies, parallel to the mean precipitation axis. The mechanism is similar to that which causes transient convection in the ITCZ during austral summer (Kiladis & Weickmann, 1992a,b). Condensation and subsequent latent heat release in the convection force additional ascent and upper-tropospheric divergence (3). Through vortex stretching this results in an anticyclonic vorticity tendency which acts to weaken the initial cyclonic anomaly (4). Depending on the strength of the negative feedback the wave can propagate onwards or dissipate. The computation of a full vorticity budget allows for a quantitative analysis of the relative importance of different vorticity tendency terms in the propagation of the transient wave. In the SPCZ this has shown that the feedback is strong enough to dissipate the wave within a day and propagation stops in the SPCZ region (5). This is in agreement with the proposed hypothesis and scale analysis of Matthews (2012).

Figure 2.14 shows the mechanism for the development of the diagonal SACZ.

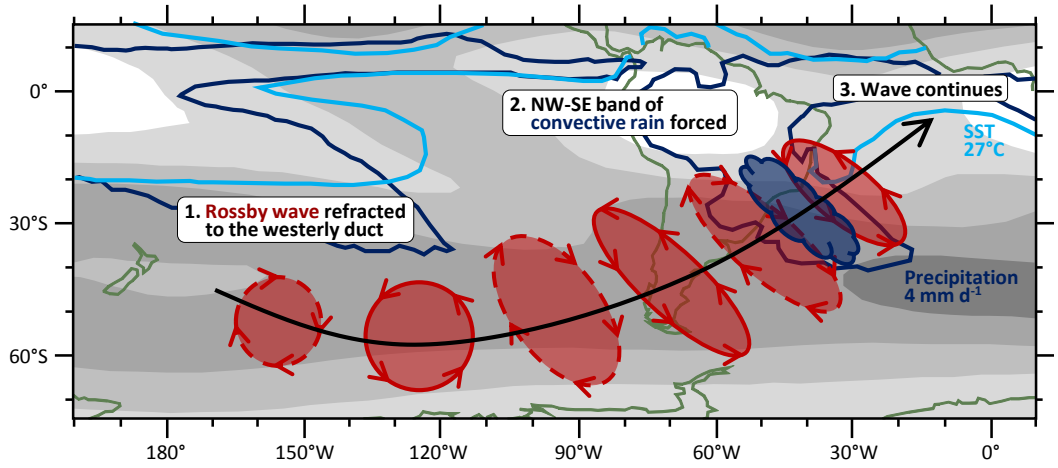

Figure 2.14: Schematic of mechanism for the development of a diagonal SACZ. A Rossby wave train from the central south Pacific is refracted towards the equatorial Atlantic westerly duct (1). Originally quasi-circular vorticity centres deform to have a northwest-southeast elongation. Ahead of a cyclonic vorticity anomaly, poleward wind is associated with destabilisation and ascending motions that trigger deep convection in a diagonal band (2). Though latent heat from condensation gives additional ascent and upper-tropospheric divergence, the associated anticyclonic vorticity tendency is not strong enough to dissipate the wave. The Rossby wave therefore continues propagating equatorward after forcing convection (3).

Over South America a comparable wave train propagates equatorwards towards the Atlantic westerly duct (1). The same mechanisms that provided the northwest-southeast tilt and equatorward propagation in the SPCZ act here. A cyclone triggers diagonally oriented convection (2) and forces upper-level divergence as was also the case in the SPCZ region. However, the vorticity budget calculations in this case show that the divergence forced by the wave is not strong enough to dissipate the wave in situ. The wave and convection therefore propagate past the mean precipitation axis (3). This is in agreement with the cross-correlations found between the PCs of the shifted and enhanced modes that were found in the SACZ only.

The existence of both the SPCZ and SACZ is due to the atmospheric basic state. Following the conceptual framework of Meehl *et al.* (2001), processes at longer time scales and larger spatial scales, including ENSO and MJO, set the base state upon which the transient Rossby waves get refracted equatorward. The accumulated effect of individual waves and short-lived pulses of convection then feeds back on to the mean state.

In chapter 3 the interaction between transient Rossby waves and convection will

be tested in an AGCM. In an specially designed experiment the negative feedback, that has been shown to play a crucial role in the interaction, is isolated and cancelled. That way the influence of convection in SPCZ convective events is tested.

3

THE INFLUENCE OF DIABATIC HEATING IN THE SOUTH PACIFIC CONVERGENCE ZONE ON ROSSBY WAVE PROPAGATION AND THE MEAN FLOW

3.1 INTRODUCTION

In chapter 2 observational-based data products were used to develop a framework to describe a mechanism that forces diagonal bands of convective precipitation in the South Pacific Convergence Zone (SPCZ). It described how Rossby waves from the Australian subtropical jet are refracted towards the upper-tropospheric westerlies over the equatorial eastern Pacific (the 'westerly duct'). In this process, initial circular vorticity centres are elongated and develop a northwest-southeast, diagonal, orientation. Ahead of a cyclonic vorticity centre poleward flow enhances ascent in a band parallel to the diagonally oriented cyclone. In the tropical conditionally unstable atmosphere this triggers deep convection. Latent heat release caused by condensation then enhances the ascending motions. The upper-tropospheric divergence associated with the convection and ascent is a source of anticyclonic vorticity through vortex stretching. The propagating cyclonic vorticity centre

encounters this anticyclonic tendency; consequently the cyclone is weakened and dissipated in situ. The climatological SPCZ is the sum of many Rossby wave forced convection events.

In this framework, Rossby waves ultimately dissipate themselves by means of a negative feedback involving convection and diabatic heating. This is consistent with the observation of Trenberth (1976) that the SPCZ area acts as *"a 'graveyard' region for fronts moving from the southwest"* and the deceleration of Rossby waves over the SPCZ area discussed in Widlansky *et al.* (2011). Here, the validity of the proposed framework will be tested in an Atmospheric General Circulation Model (AGCM) of intermediate complexity. Furthermore, the influence of diabatic heating from convective events in the SPCZ on the regional mean flow will be investigated.

Tropical convection and associated heating is a substantial source of energy. Dynamical responses to such forcing have been the topic of many studies. Theoretically, the Matsuno-Gill model explains the generation and development of an equatorial Kelvin and Rossby wave response to localised tropical heating (e.g. as observed in the Madden-Julian Oscillation, MJO, Matsuno, 1966; Gill, 1980). However, the dynamical response to tropical heating is not limited to the tropics (e.g. Qin & Robinson, 1993; Jin & Hoskins, 1995; Matthews *et al.*, 2004). The explicit influence of diabatic heating within the SPCZ has so far not been a topic of many investigations.

Following the SPCZ mechanism in the framework of chapter 2, an AGCM experiment has been designed in which the thermodynamic response to dynamical Rossby wave forcing is removed in the SPCZ region. Potential changes to the Rossby wave and the south Pacific mean flow will be investigated. In section 3.2 the AGCM used in the experiments is described. The perturbation experiment is explained in more detail in section 3.3. The results are described in section 3.4 and finally the findings are summarised in section 3.5.

3.2 MODEL DESCRIPTION

The Intermediate General Circulation Model version 4 (IGCM4, Joshi *et al.*, 2015) has been used in this study. It is a AGCM of intermediate complexity, i.e. within the hierarchy of climate models it has simpler parametrisation schemes than state-of-the-art AGCMs (e.g. the AGCMs in the Coupled Model Intercomparison Project phase

5, CMIP5). This makes the model well-suited for idealised experiments to increase process-level understanding.

IGCM4 is part of the 'Reading IGCM' family of models, based on the spectral model of Hoskins & Simmons (1975). IGCM4 is a spectral, primitive equation model. Diabatic processes include hyperdiffusion and moist processes, i.e. moisture transport, evaporation and convection. It is a full atmospheric model; orography and surface processes are included as well as parametrisations of convection and radiation. Here the model formulation of IGCM4 is described; in section 3.2.1 the dynamical core is described, in section 3.2.2 a more detailed description of all physical parametrisations in IGCM4 is given. Given the fact that this thesis considers the large-scale organisation of convective precipitation, the convection scheme is described in extra detail. Joshi *et al.* (2015) and Forster *et al.* (2000) provide full descriptions of the physics in IGCM4.

3.2.1 DYNAMICAL CORE

IGCM4 solves the primitive equations; these include the horizontal momentum equation:

$$\frac{D\mathbf{V}}{Dt} + f(\mathbf{k} \times \mathbf{V}) = -\nabla\Phi, \tag{3.1}$$

the hydrostatic approximation:

$$\frac{\partial\Phi}{\partial p} = -\frac{1}{\rho},$$

the continuity equation:

$$\nabla \cdot \mathbf{U} = 0$$

and the thermodynamic equation:

$$\frac{D\theta}{Dt} = \frac{J}{C_p}\frac{\theta}{T}.$$

In these equations, $\mathbf{V} = (u, v)$ is the horizontal velocity, t is time, f is the Coriolis parameter, $\mathbf{k}$ is the unit vector along the vertical axis, Φ is the geopotential, p is pressure, ρ is density, $\mathbf{U} = (u, v, \omega)$ the three dimensional velocity, θ is potential temperature, J is diabatic rate of heating, C_p is the specific heat of dry air at

constant pressure and T is temperature. To solve these equations IGCM4 uses the spectral method in the horizontal and finite differencing in the vertical. The vertical coordinate system is based on σ coordinates, with $\sigma = \frac{p}{p_s}$ and p_s the surface pressure. IGCM4 is used here in its T42L20 configuration, i.e. spectral triangular truncation at total wavenumber 42 (128×64 cells in the horizontal Gaussian grid) and 20 layers in the vertical up to 50 hPa.

Vorticity, ζ, and divergence, D, are used as prognostic variables, rather than the vector wind $\mathbf{V}$. Hence, equation 3.1 is transformed to an equation for vorticity, $\zeta = \mathbf{k}\cdot(\nabla\times$ 3.1$)$, and divergence, $D = \nabla\cdot$ 3.1. Because IGCM4 is based on σ coordinates, all equations are then transformed from pressure coordinates to σ coordinates, $\nabla_p = \nabla_\sigma - \sigma\frac{\partial}{\partial\sigma}\nabla\ln(p_s)$. Temperature is modelled as a departure from a mean profile: $T = T_0(\sigma) + T'$, all variables are non-dimensionalised. The resulting equations after these transformations were derived by Hoskins & Simmons (1975). These are the two horizontal momentum equations:

$$\frac{\partial\zeta}{\partial t} = \frac{1}{1-\mu^2}\frac{\partial}{\partial\lambda}\mathscr{F}_v - \frac{\partial}{\partial\mu}\mathscr{F}_u,$$

and

$$\frac{\partial D}{\partial t} = \frac{1}{1-\mu^2}\frac{\partial}{\partial\lambda}\mathscr{F}_u + \frac{\partial}{\partial\mu}\mathscr{F}_v - \nabla^2\left(\frac{U^2+V^2}{2\left(1-\mu^2\right)} + \Phi + T_0\ln(p_s)\right),$$

the hydrostatic approximation:

$$\frac{\partial\Phi}{\partial\ln(\sigma)} = -T,$$

the continuity equation:

$$\frac{\ln(p_s)}{\partial t} = -\mathbf{V}\cdot\nabla\ln(p_s) - D - \frac{\partial\dot{\sigma}}{\partial\sigma},$$

and the thermodynamic equation:

$$\frac{\partial T'}{\partial t} = -\frac{1}{1-\mu^2}\frac{\partial}{\partial\lambda}\left(UT'\right) - \frac{\partial}{\partial\mu}\left(VT'\right) + DT' - \dot{\sigma}\frac{\partial T}{\partial\sigma} + \kappa\frac{T\omega}{p}.$$

Here $\mathscr{F}_u = V\zeta - \dot{\sigma}\frac{\partial U}{\partial\sigma} - T'\frac{\partial\ln(p_s)}{\partial\lambda}$, $\mathscr{F}_v = -U\zeta - \dot{\sigma}\frac{\partial V}{\partial\sigma} - T'\left(1-\mu^2\right)\frac{\partial ln(p_s)}{\partial\mu}$, $\dot{\sigma}$ is the material derivative of σ, λ is longitude, $\mu = \sin\phi$, ϕ is latitude, U and V are the zonal

and meridional wind components multiplied by $\cos\phi$ and the horizontal advection operator is

$$\mathbf{V}\cdot\nabla = U\frac{1}{1-\mu^2}\frac{\partial}{\partial\lambda} + V\frac{\partial}{\partial\mu}.$$

The remaining unknown variables, ζ, D, T', Φ and $\ln(p)$ are then represented by truncated series of spherical harmonics. During model integration, in each time step, diabatic and adiabatic processes are computed separately. In this split time step approach, the diabatic changes are computed first, followed by the non-linear adiabatic terms. The resulting tendencies are then transformed to the spectral grid and used in the adiabatic forward time step.

3.2.2 PARAMETRISATION SCHEMES

A monthly mean climatological seasonal cycle of Sea Surface Temperature (SST) is prescribed. IGCM4 linearly interpolates the monthly SST fields onto the relevant model Julian day. For all model integrations in chapters 3 and 4 of this thesis, the standard IGCM4 SST climatology has been replaced by one based on NOAA's Optimum Interpolation V2 dataset (Reynolds *et al.*, 2002, mean over 1982-2009). Surface fluxes are calculated using temperature and humidity differences between the surface and the lowest model layer and an effective wind speed based on atmospheric stability. Land surface temperatures are then computed self-consistently from these fluxes (Forster *et al.*, 2000; Joshi *et al.*, 2015).

To parametrise convective processes the scheme of Betts (1986) is used. It is assumed that, in convective regions, environmental buoyancy and buoyancy within clouds are similar, therefore the observed thermodynamic profile of the atmospheric column can be used as a basis for the parametrisation of convective adjustments. By taking this approach, it is not necessary to implement a separate cloud vapour model. All adjustments due to dry or moist convection are thus based on local atmospheric stability and parcel buoyancy.

First, a column is checked for dry unstable layers which are then adjusted to a neutral state in a single time step. For moist convection, based on an estimated convection height, either a shallow convection parametrisation or a deep convection parametrisation is chosen. For each scheme a separate reference profile of moisture, q_R, is computed. The convective adjustment is then computed as the difference

of the current profile and the reference profile and applied over a relaxation time (τ), representative of the convective time scale. This time scale is 3 hours for deep convection and 6 hours for shallow convection. The adjustment to the moisture field (q) is then computed and applied, such that the moisture tendency from the convective parametrisation is:

$$\frac{\partial q}{\partial t} = \frac{q_R - q}{\tau}. \tag{3.2}$$

Effectively, moisture is redistributed in the atmospheric column and transported from low-levels to the mid-troposphere. Following the moisture adjustment, the temperature profile (T) is adjusted in a consistent manner, such that the amount of diabatic heating from moisture adjustment is equivalent to the temperature adjustment. Within an atmospheric column, multiple dry and/or moist convective layers are allowed (Betts, 1986). After computation of the convective adjustments the precipitation amounts are calculated, any excess moisture is assumed to rain out (Joshi *et al.*, 2015).

Cloud cover is computed to match observed profiles of convective clouds (Slingo, 1987). Stratiform cloud fractions are calculated from relative humidity values; in case of supersaturation, IGCM4 precipitates all excess moisture. Marine stratocumulus clouds are computed following Kawai & Inoue (2006). IGCM4 runs a modified Morcrette radiation scheme (Zhong & Haigh, 1995) once for each model day, computed fluxes are then constant over the next 24 model hours. Two radiation bands in the visible part of the spectrum are included, five bands in the infrared part. A zonally averaged climatology of O_3 is prescribed, which absorbs ultraviolet radiation between 0.12 and 0.25 μm. The current version of IGCM4 does not include aerosol forcing.

The November to April time mean precipitation for observations and in the IGCM4 control integration are in good agreement (figures 3.1a and 3.1b). The Climate Prediction Center Merged Analysis of Precipitation (CMAP) has been used here as observations (Xie & Arkin, 1997, mean over 1979-2008, section 2.2). The SPCZ location and orientation are simulated well; the simulated precipitation rate within the SPCZ is slightly lower than observed. The bottom two panels of figure 3.1 show that most of the simulated precipitation in the tropics results from the convective moist adjustment scheme.

Appendix B includes further model evaluation with climatological mean maps

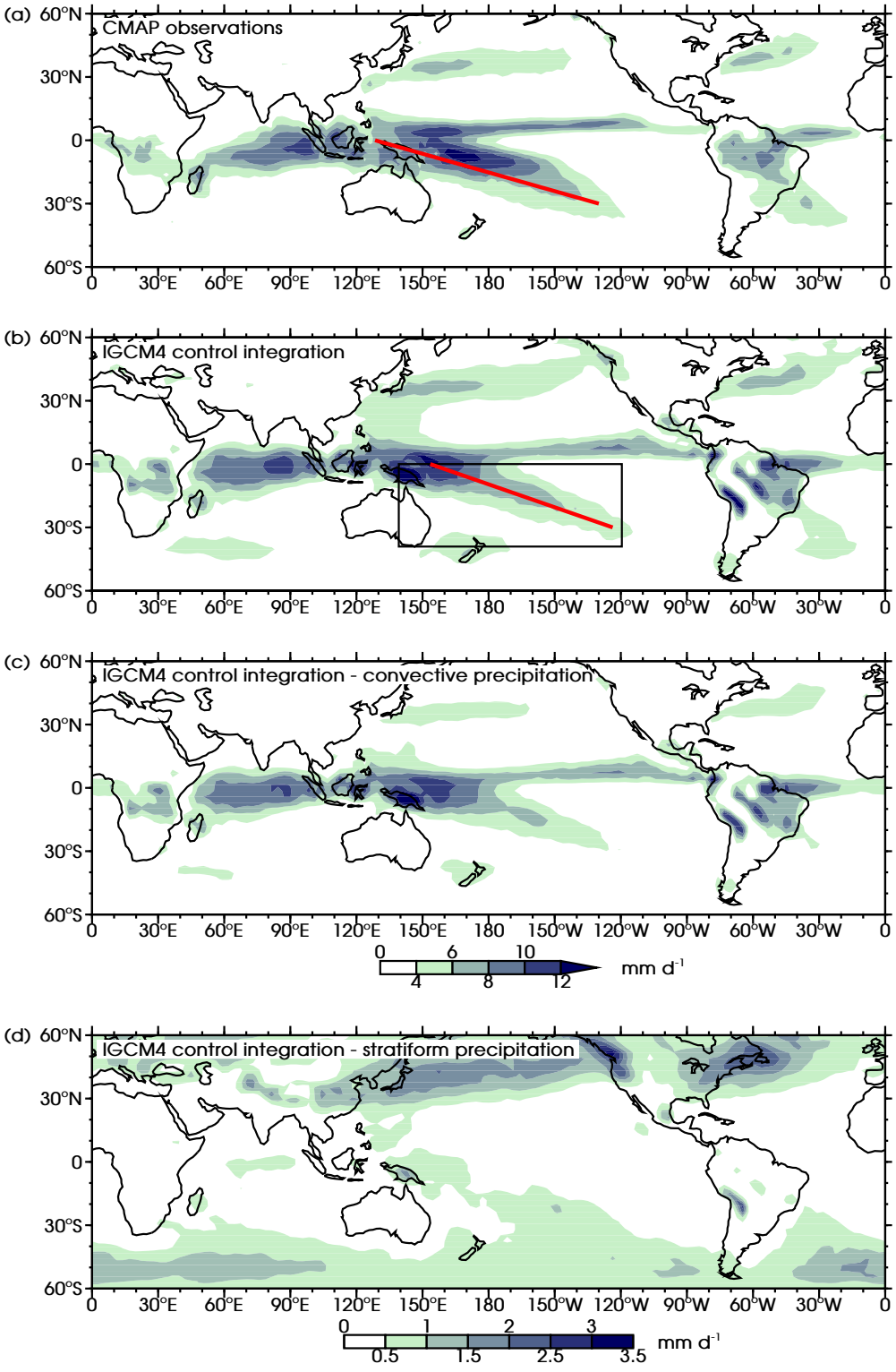

Figure 3.1: Time mean precipitation rate (November to April) in (a) CMAP and (b) the IGCM4 control integration (mm d^{-1}). Simulated precipitation in IGCM4 is split in (c) convective precipitation and (d) stratiform precipitation. The thick diagonal red lines in (a,b) show the position of the SPCZ mean precipitation axis, the rectangle in (b) shows the region for the perturbation experiment. Note different colour scale for (d).

of other variables and a comparison of simulated precipitation in IGCM4 with the CMIP5 atmosphere-only ('AMIP') models. Model biases in the spatial patterns in surface temperatures and Outgoing Longwave Radiation (OLR) are small. Vertical profiles of the zonal mean zonal wind indicate the subtropical jets are of the approximate right strengths, though the Southern Hemisphere jet is displaced equatorward by about 10°. Precipitation biases in IGCM4 are compared to the inter-model variability of the models in the CMIP5 archive; the precipitation field in IGCM4 is of similar quality as the precipitation fields from state-of-the-art AGCMs.

3.3 EXPERIMENTAL SETUP

3.3.1 CONTROL INTEGRATION

The aim of the current chapter is to investigate the influence of diabatic heating from convective activity in the SPCZ on other aspects of the Pacific climate. With this in mind a perturbation experiment was designed in which SPCZ convective events are removed. The experiment is based on the transient wave - convection framework (chapter 2). Figure 3.2 shows a flow diagram that depicts the consecutive steps in the experiment, each described in more detail below.

First, an IGCM4 control integration was conducted. This integration was 17 years long, from which the first year was removed as spin-up. The remaining 16 years of data contained 15 full November to April seasons (step 1 in figure 3.2). Within these seasons, 140 SPCZ 'convective events' were selected, based on Empirical Orthogonal Functions (EOFs). EOF spatial patterns of variability were computed from anomalies of OLR in a box over the SPCZ region (180°-120°W, 5°-30°S, rectangle in figure 3.3). In the tropics, OLR can be used as a proxy for precipitation; lower values are associated with colder temperatures, higher cloud tops and enhanced deep convection, higher values with warmer temperatures, lower cloud tops and reduced deep convection. The Principle Component (PC) time series associated with EOF 1 is then used for the selection of the convective events. If the value of the PC was above 1 standard deviation and was a local maximum relative to 5 days before and 5 days after that day, it was selected as a convective event (step 2 in figure 3.2).

In the control integration, the computed temperature tendencies in the deep

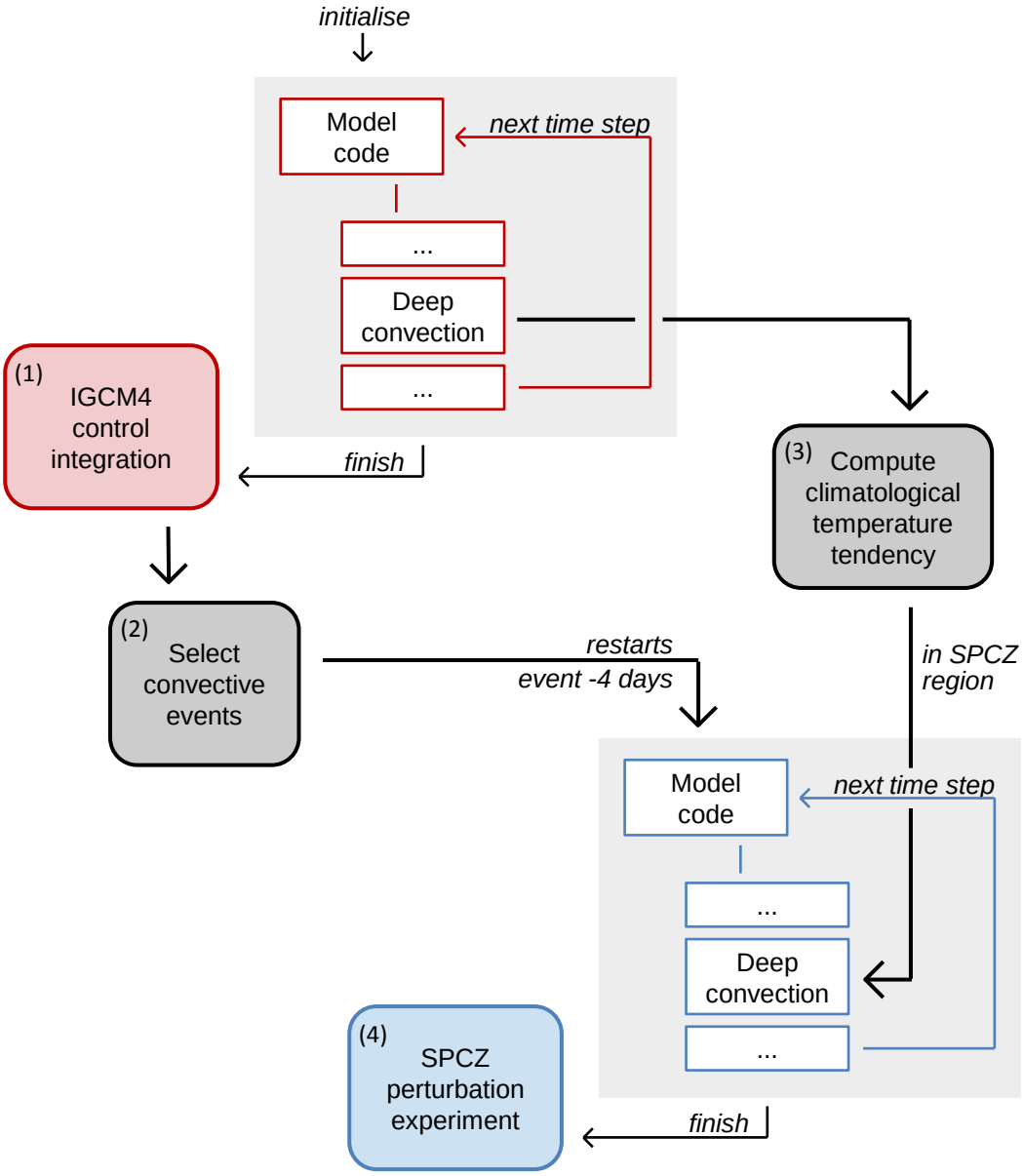

Figure 3.2: Flow diagram of experimental setup. Numbers (1) – (4) are references to detailed explanations in the main text (section 3.3).

convection routine were saved at every timestep. These temperature tendency data were used to compute a three-dimensional monthly varying climatology (step 3 in figure 3.2), to be used in the perturbation experiment.

3.3.2 PERTURBATION EXPERIMENT

The perturbation experiment aims to prevent dynamical forcing from Rossby waves from generating the observed anomalous diabatic heating response in the SPCZ

region (chapter 2). The experiment is based on 140 restart integrations started 4 days before each of the 140 selected convective events in step 2. At this time (event −4 days) the dynamical transient Rossby wave forcing is present, but the convective response in the SPCZ region has not commenced. From this atmospheric state a modified IGCM4 was integrated for 14 days (i.e. up to 10 days after the event). In the modified model all grid cells overlying ocean in the SPCZ region (140°E-120°W, 0°-40°S, rectangle in figure 3.1b) have the deep convective temperature tendency prescribed from the precalculated climatological tendency in step 3 rather than computed self-consistently within the model code; i.e. instead of allowing the the deep convection scheme to compute temperature tendencies, the climatological values were used

$$\frac{\partial T}{\partial t} = \left(\frac{\partial T}{\partial t}\right)_{clim}. \tag{3.3}$$

Moisture tendendies and precipitation were computed as normal to avoid an unrealistic build up or removal of moisture. Outside the SPCZ region the model code was integrated as normal. The perturbation experiment is the composite mean of all restart integrations (step 4 in figure 3.2).

In the next section results from the different steps are discussed separately. Steps 1 and 2 will be discussed in section 3.4.1, step 3 in 3.4.2 and finally step 4 in 3.4.3 and 3.4.4.

3.4 EXPERIMENTAL RESULTS

3.4.1 TRANSIENT WAVE - CONVECTION FEEDBACK IN CONTROL INTEGRATION

The first mode of variability from EOF analysis (7.8% of total variance) shows enhanced convection (negative OLR anomalies) shifted to the southwest, however it remains parallel to the SPCZ mean precipitation axis (figure 3.3a). To the northeast a parallel band of reduced convection is found. The second mode of variability (7.3%, not shown) shows enhanced convection over the mean precipitation axis and reduced convection to the southwest. These 'southwestward shifted' and 'enhanced' convection patterns are comparable to patterns found in observational data (figure 2.3).

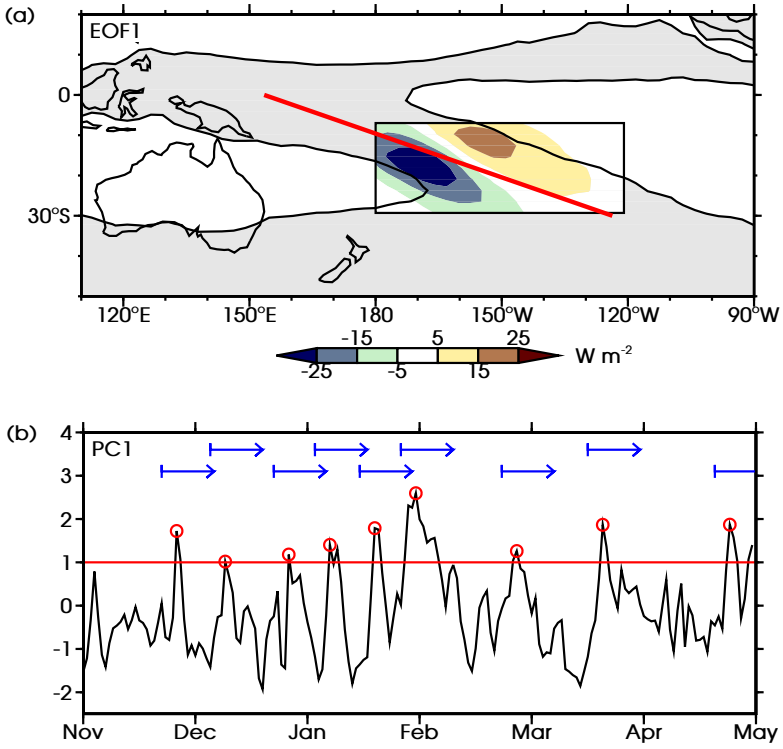

Figure 3.3: (a) EOF pattern 1 in shaded colours (W m^{-2}) in the rectangular box, overlaid on the time mean OLR field (November to April, grey shading is < 250 W m^{-2}). The thick diagonal red line shows the position of the SPCZ mean precipitation axis. (b) Sample time series of the PC associated with EOF 1 during November-April of model integration year 10. The red line and circles show the selection of SPCZ convective events, blue arrows show the duration of the associated restart integrations.

Following the criteria presented in section 3.3, 140 events of the southwestward shifted mode have been selected from the EOF 1 PC time series (figure 3.3b). Composite means were computed by taking the mean of a field over all event days. Anomalies of 200 hPa vorticity and precipitation for these convective events are shown in figure 3.4. Four days before the event a Rossby wave train is present south of Australia. As was found in observational-based data, over the following days, the wave is refracted along a curved path towards the equatorial east Pacific. During this process advection by the mean wind, shear on the equatorward edge of the jet and Rossby wave refraction reform the vorticity centres (chapter 2); the centres develop a northwest-southeast diagonal orientation, parallel to the SPCZ mean precipitation axis (figure 3.4b).

Two days before the convective event the Rossby wave initiates enhanced precipitation. Ahead of a cyclonic vorticity anomaly, poleward wind ascends and

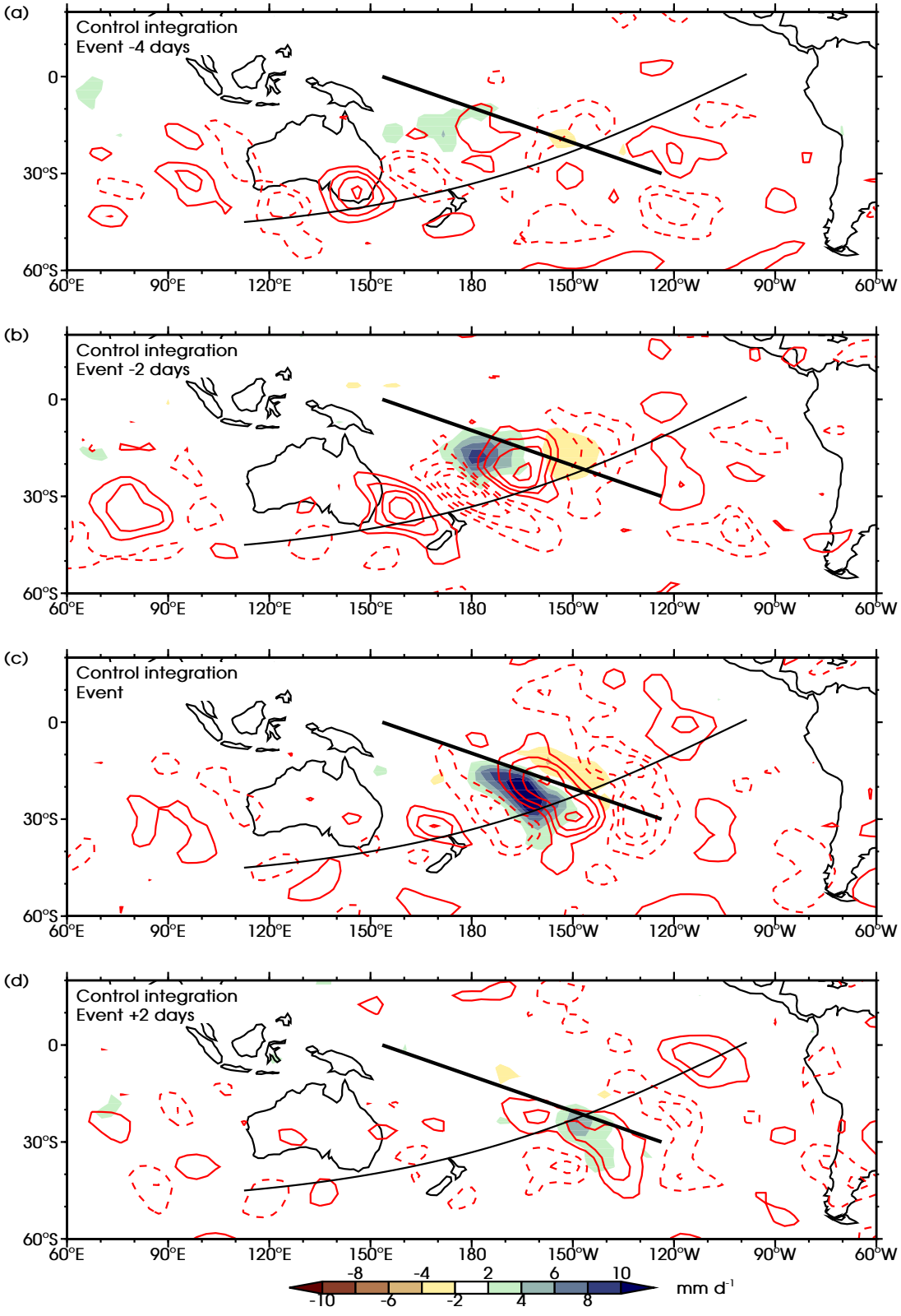

Figure 3.4: Composite mean anomalies over the 140 shifted SPCZ events of precipitation rate in shaded colours (mm d^{-1}), and 200 hPa vorticity in red contours (4×10^{-6} s^{-1} contour interval, zero contour omitted, negative contours dashed) for the IGCM4 control integration. The thick diagonal line indicates the position of the SPCZ mean precipitation axis, the curved line an approximate wave propagation path. Time lags shown: (a) event −4 days, (b) event −2 days, (c) event, and (d) event +2 days.

in the tropical conditionally unstable atmosphere this triggers deep convection. The vorticity centre propagates northeastward with the Rossby wave, the associated precipitation signal remains ahead of the cyclone at all times. At the day of the convective event, by design of the composite method, the precipitation anomaly reaches a maximum ($\sim$ 10 mm d^{-1}) and the pattern resembles the southwestward shifted pattern of EOF 1; there is a diagonal band of enhanced precipitation to the southwest of the SPCZ mean precipitation axis and reduced precipitation to the northeast. Two days after the convective event the precipitation anomalies have mostly disappeared (figure 3.4d).

The diabatic heat release from convection is substantial and enhances ascending motions and upper-tropospheric divergence. Through vortex stretching this acts as a negative feedback, $\frac{\partial \zeta}{\partial t} = -fD$, and results in an anticyclonic tendency: the propagating cyclone in the Rossby wave is dissipated. Consequently, Rossby wave propagation is disturbed downstream of the SPCZ region. The effect is clear in the evolution of the vorticity centres in the Rossby wave in figure 3.4, at the moment precipitation anomalies are triggered propagation of the upstream cyclonic vorticity centre slows down and weakens. The Rossby wave favours a more southern propagation path where both precipitation anomalies and the negative feedback effect are weaker. Two days after the convective event the wave is mostly dissipated.

The sequence of events forcing diagonally oriented bands of precipitation in the IGCM4 control integration is similar to the sequence found using observational-based data products (chapter 2). A transient Rossby wave forces a diagonal band of convection and precipitation that, through a vortex stretching negative feedback, dissipates the Rossby wave over the SPCZ region. The realistic representation of this process makes IGCM4 a suitable AGCM for the perturbation experiment.

3.4.2 DIABATIC HEATING FROM DEEP CONVECTION

The simulated November to April time mean mid-tropospheric climatological heating due to deep convection is shown in figure 3.5a. Higher values of diabatic heating are found at locations with frequent convective precipitation, lower values in areas of less precipitation (figures 3.1b, 3.5a). The SPCZ, Intertropical Convergence Zone (ITCZ), South Atlantic Convergence Zone (SACZ) and South Indian Convergence Zone can all

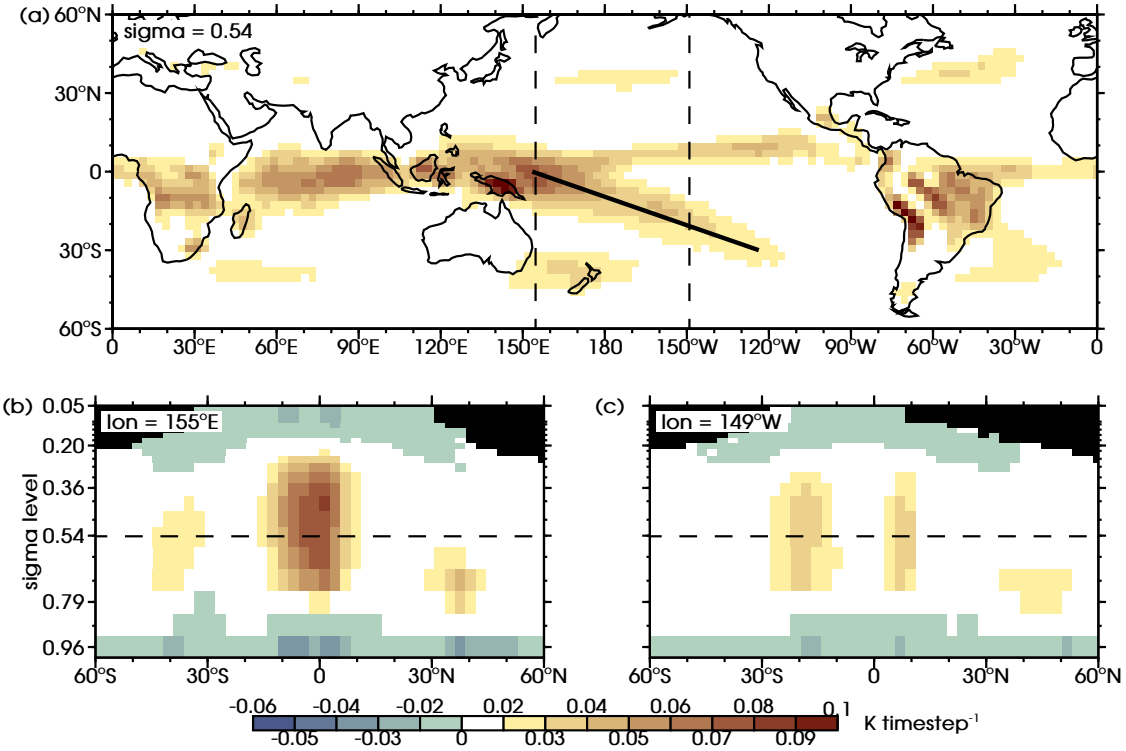

Figure 3.5: Time mean temperature tendency due to deep convection (November to April) in IGCM4 at (a) $\sigma = 0.54$, and vertical sections at (b) 155°E and (c) 149°W in shaded colours (K timestep^{-1}). Dashed lines in (a) show the locations of the vertical sections in (b,c), dashed lines in (b,c) show the level of the map in (a). The thick diagonal line in (a) shows the position of the SPCZ mean precipitation axis. Black areas signify areas where data is not available.

be identified as areas of enhanced diabatic heating from deep convection. The south Pacific dry zone has very weak diabatic heating from deep convection.

Figures 3.5b,c show vertical sections of the same quantity. The black areas on the cross-section show the grid cells where the IGCM4 deep convection scheme has not once been initiated in the 15 seasons included in the control integration (effectively the stratosphere). For these cells a climatological heating of 0 K timestep^{-1} is assumed in the experimental integration. Along 155°E (figure 3.5b) the region of most intense heating lies over the equator, where the SPCZ and ITCZ merge. In this region, there is a slight negative temperature tendency at the surface, in the mid-troposphere there is substantial diabatic heating and near the model top (σ=0.05) there is a negative temperature tendency. Further west at 149°W (figure 3.5c) the heating profiles related to the SPCZ and ITCZ are weaker and separated and found at about 20°S and 8°N respectively.

These climatological temperature tendency data are used in the perturbation

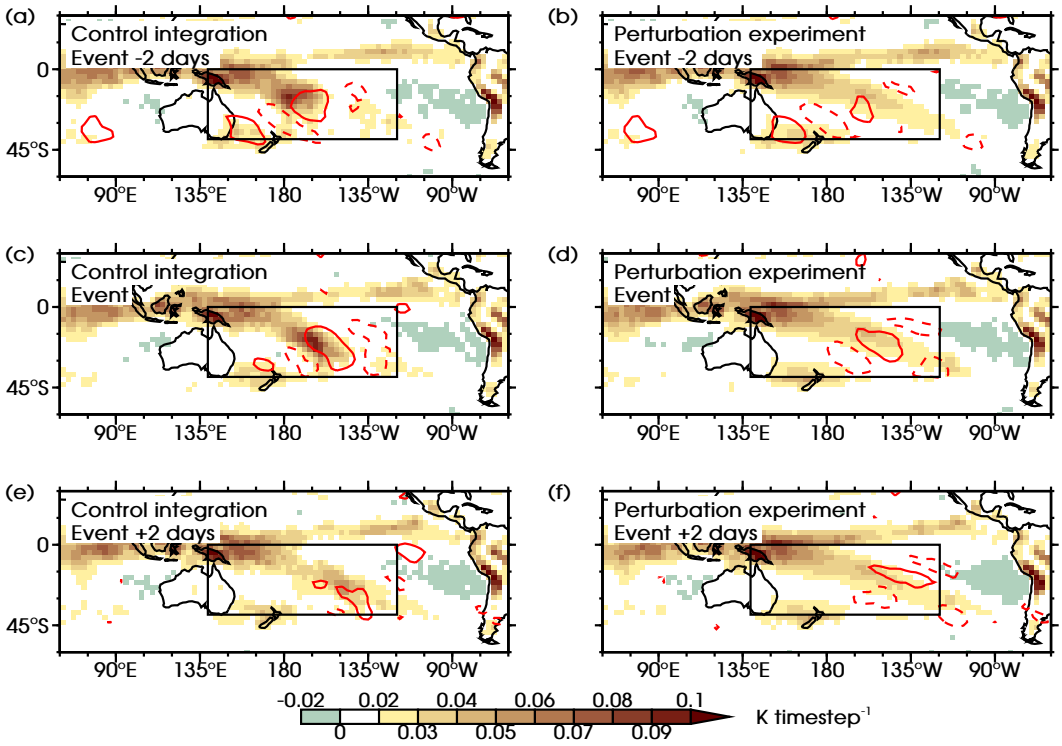

Figure 3.6: Composite mean temperature tendency due do deep convection at $\sigma = 0.54$ in shaded colours (K timestep^{-1}). (a,c,e) show the instantaneous, self-consistent model computed tendency in the control integration. In the perturbation experiment this is replaced by the climatological tendency within the experiment region (black rectangle) as shown in (b,d,f). Red contours show 200 hPa vorticity anomalies (the 8×10^{-6} s^{-1} contour as a solid line, the -8×10^{-6} s^{-1} contour as a dashed line).

experiment. Instantaneous, self-consistent temperature tendencies are used in the control integration (left column of figure 3.6). This heating pattern is more irregular than in the climatology, changes fast in time and has larger extremes. Following the earlier discussion, it can be seen that ahead of upper-tropospheric cyclonic vorticity anomalies convective heating is strongest. As the cyclone propagates northeastward this region of enhanced heating also moves northeastward, similar to the progression of precipitation anomalies (figure 3.4). Ahead of anticyclonic vorticity anomalies convective heating is weaker. In the perturbation experiment, as discussed in section 3.3, in the SPCZ region this instantaneous, self-consistent temperature tendency is replaced by the relevant climatological value from the seasonal cycle appropriate for each of the 140 restart integrations, i.e. if the restart integration is for a day in January, the January mean climatology is prescribed. The composite mean temperature tendencies as used in the experimental model integration are shown in

the right column of figure 3.6. Outside the rectangular SPCZ region there has been no change from the control integration (small differences due to separate integrations in control and experiment), inside the rectangular region instantaneous values have been replaced by climatological values (compare horizontal rows in figure 3.6).

3.4.3 IMPACT OF DIABATIC HEATING ON ROSSBY WAVE PROPAGATION

As described in section 3.3, the restart integrations are initiated from the control integration at 4 days before the 140 selected convective events. At this moment a Rossby wave train is present south of Australia (figure 3.7a). Two days into the perturbation experiment, the Rossby wave has propagated northeastward into the SPCZ region (figure 3.7b). Ahead of the cyclonic anomaly is an anomalous poleward flow that leads to ascent along the sloping mean isentropes. There is a small anomalous precipitation signal associated with this ascent (~ 2 mm d^{-1}). However, the associated anomalous diabatic heat release is removed in the experiment so no additional ascending motions are forced. This results in a much weaker precipitation rate in the perturbation experiment than in the control integration at this point (~ 8 mm d^{-1}, figure 3.4b).

In the following days this process continues. Vorticity centres in the wave propagate northeastward. Ahead of the cyclonic vorticity anomaly and along the SPCZ mean precipitation axis there is some anomalous precipitation. However, the precipitation rates are constant around ~ 2 mm d^{-1}; there is no distinct peak in precipitation rates at the convective event as was found in the control integration.

In the sequence of events that ultimately triggers diagonal bands of convective precipitation over the SPCZ region in the control integration, the negative feedback from vortex stretching starts influencing Rossby wave propagation two days before the convective event. When the convective heating response is taken out of the sequence, diabatic heating, ascending motions and upper-tropospheric divergence are all significantly weaker than in the control integration. The maximum composite-mean upper-tropospheric divergence in the perturbation experiment is 4×10^{-6} s^{-1}, only 30% of the divergence in the control integration (13×10^{-6} s^{-1}). The negative feedback, $\frac{\partial \zeta}{\partial t} = -fD$, is therefore much weaker and has a smaller effect on the transient Rossby wave.

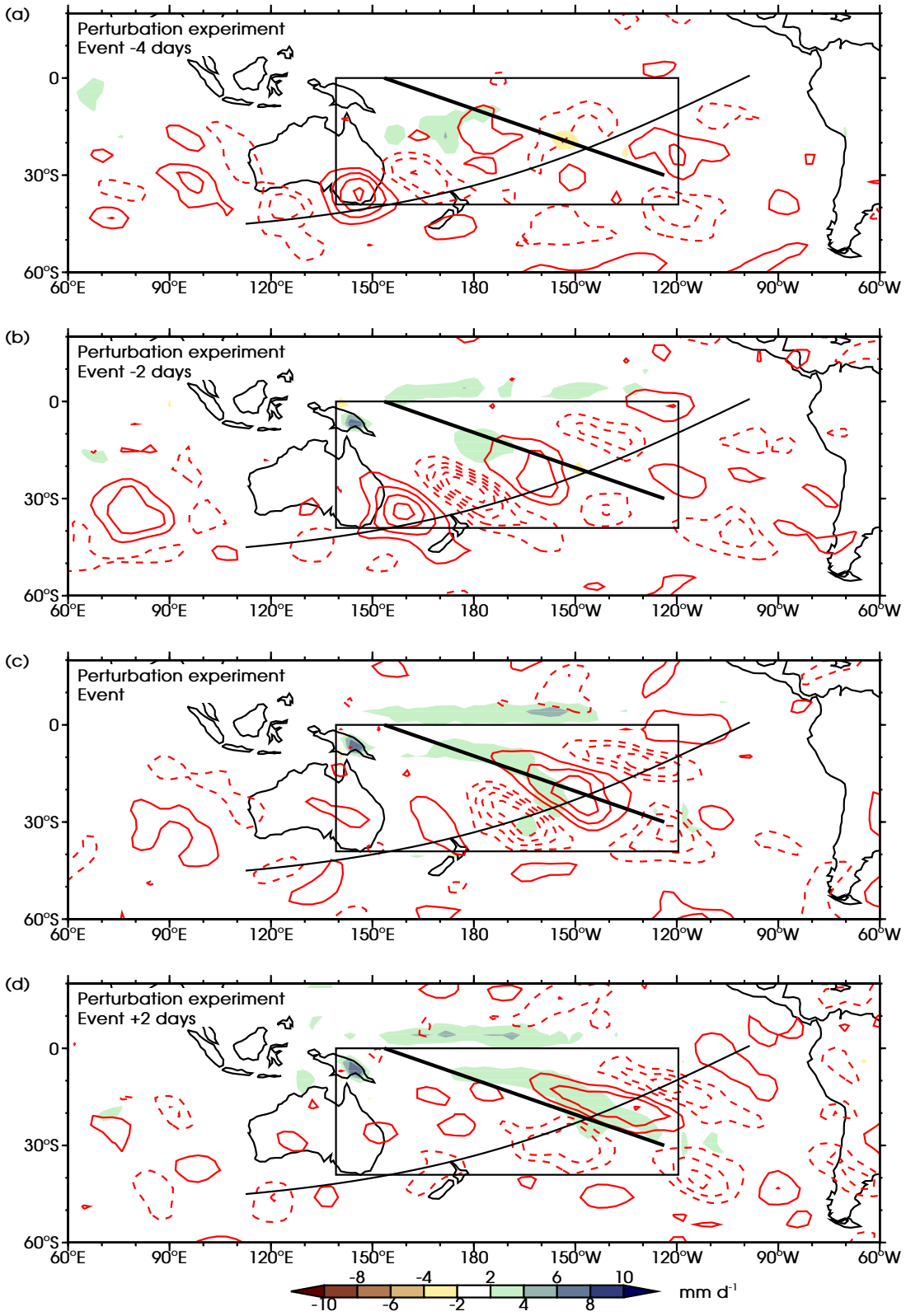

Figure 3.7: As figure 3.4, but now for the perturbation experiment. Note (a) is the same as figure 3.4a, the starting point of the pertubation experiment. The rectangle indicates the region for the perturbation experiment.

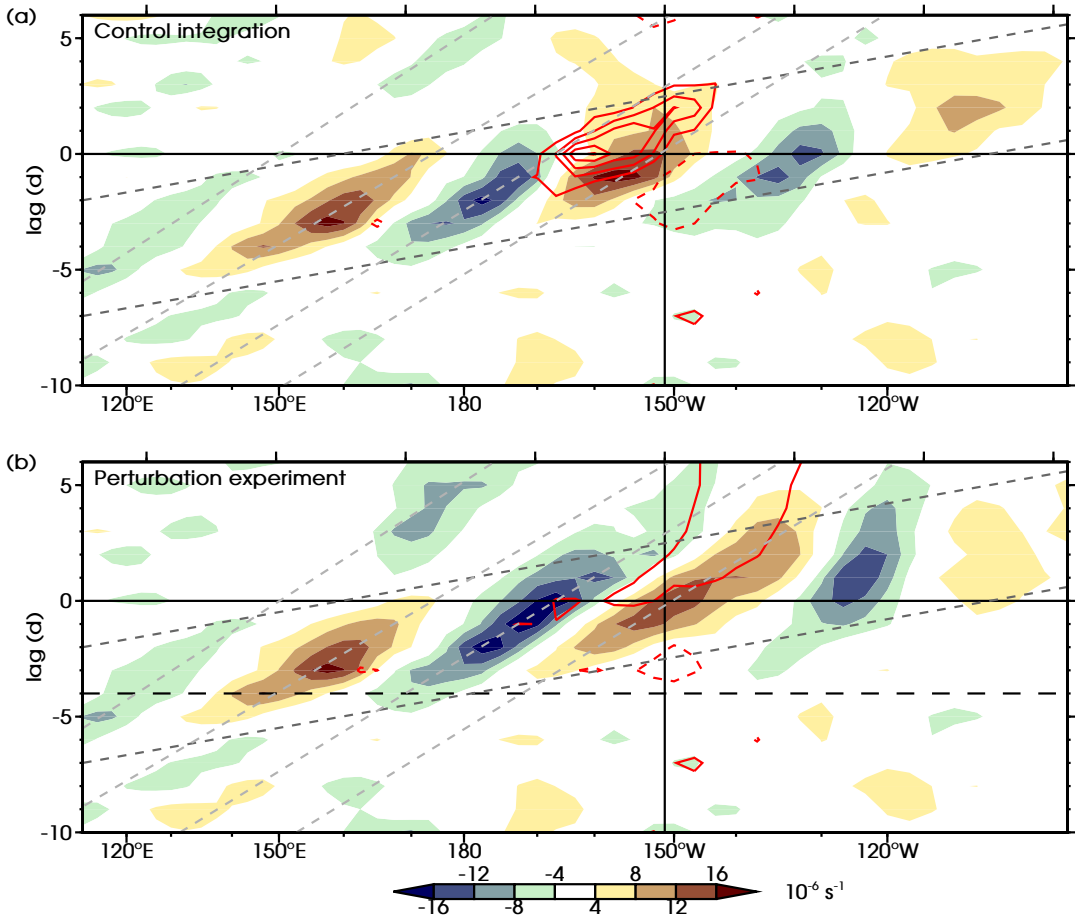

Figure 3.8: Hovmöller diagram of lagged composite anomalies along the curved propagation path in the (a) control integration (figure 3.4) and (b) perturbation experiment (figure 3.7). The 200 hPa vorticity is shown in shaded colours (10^{-6} s^{-1}) and precipitation in red contours (2 mm d^{-1} contour interval, zero contour omitted, negative contours dashed). The vertical solid line denotes the position of the SPCZ mean precipitation axis, the horizontal dashed line in (b) is the beginning of the restart integrations at event −4 days. Light grey dotted lines show the approximate phase speed, dark grey dotted lines the approximate group speed. Horizontal axes are irregular longitude (bottom) or regular distance (top, 2000 km intervals) along the path.

The northeastward propagation of the Rossby wave is undisturbed in the perturbation experiment. The vorticity centres are reformed due to shear and Rossby refraction as in the control integration, though the effects are more obvious in the experiment. Vorticity centres become elongated and rotate from a diagonal orientation (northwest-southeast) to a zonal orientation at the equator (figure 3.7c). The southward tendency of the wave pattern in the control integration is not found in the experiment, instead Rossby wave propagation continues across the equator.

The propagation speed of the Rossby wave can be estimated from a Hovmöller

diagram (figure 3.8). The vorticity centres move eastward steadily at the phase speed; wave energy moves through the region at the faster group speed. In the perturbation experiment the phase speed is about 7 m s^{-1}, the group speed approximately 23 m s^{-1} (grey dotted lines in figure 3.8). These values are comparable in the control integration, however wave propagation near the SPCZ mean precipitation axis is disturbed. The cyclone at 180° weakens when precipitation is triggered 2 days before the convective event, in the perturbation experiment the cyclone is present for longer and propagates further eastward. The same effect appears for the anticyclone at 160°W. In both model integrations propagation slows down close to the equator at about 130°W.

As precipitation rates decrease significantly in the perturbation experiment, there is a slight build up of moisture in the experimental region of up to 2 g kg^{-1} in specific humidity at 850 hPa. This moisture is advected by horizontal winds out of the experimental region. It results in enhanced precipitation over New Guinea and in a zonal line just north of the experimental region (figures 3.7c,d), these are grid cells where the model computes convective temperature tendencies self-consistently. The increased moisture content does increase modelled low level clouds and through a radiative feedback lowers surface temperatures in the SPCZ region slightly. The impact of this side effect on Rossby wave propagation in the experimental region is small.

3.4.4 IMPACT OF DIABATIC HEATING ON THE MEAN FLOW

Six days after the convective event the Rossby wave has disappeared in both the control integration and in the perturbation experiment. In the control integration the upper-troposphere has returned to its 'normal' state (figure 3.9a); anomalies of zonal wind speed are very small (less than 2 m s^{-1}). There is no coherent pattern to these anomalies over most of the Pacific Ocean, though there is a hint of a wave train over South America, from the southeast Pacific towards the equatorial Atlantic. A similar wave train has been linked to enhanced SACZ activity (e.g. Liebmann *et al.*, 1999; Robertson & Mechoso, 2000, chapter 2). By means of influence functions, Grimm & Silva Dias (1995) found a link between convection in the SPCZ and in the SACZ. However, no significant lagged correlations were found between convective events

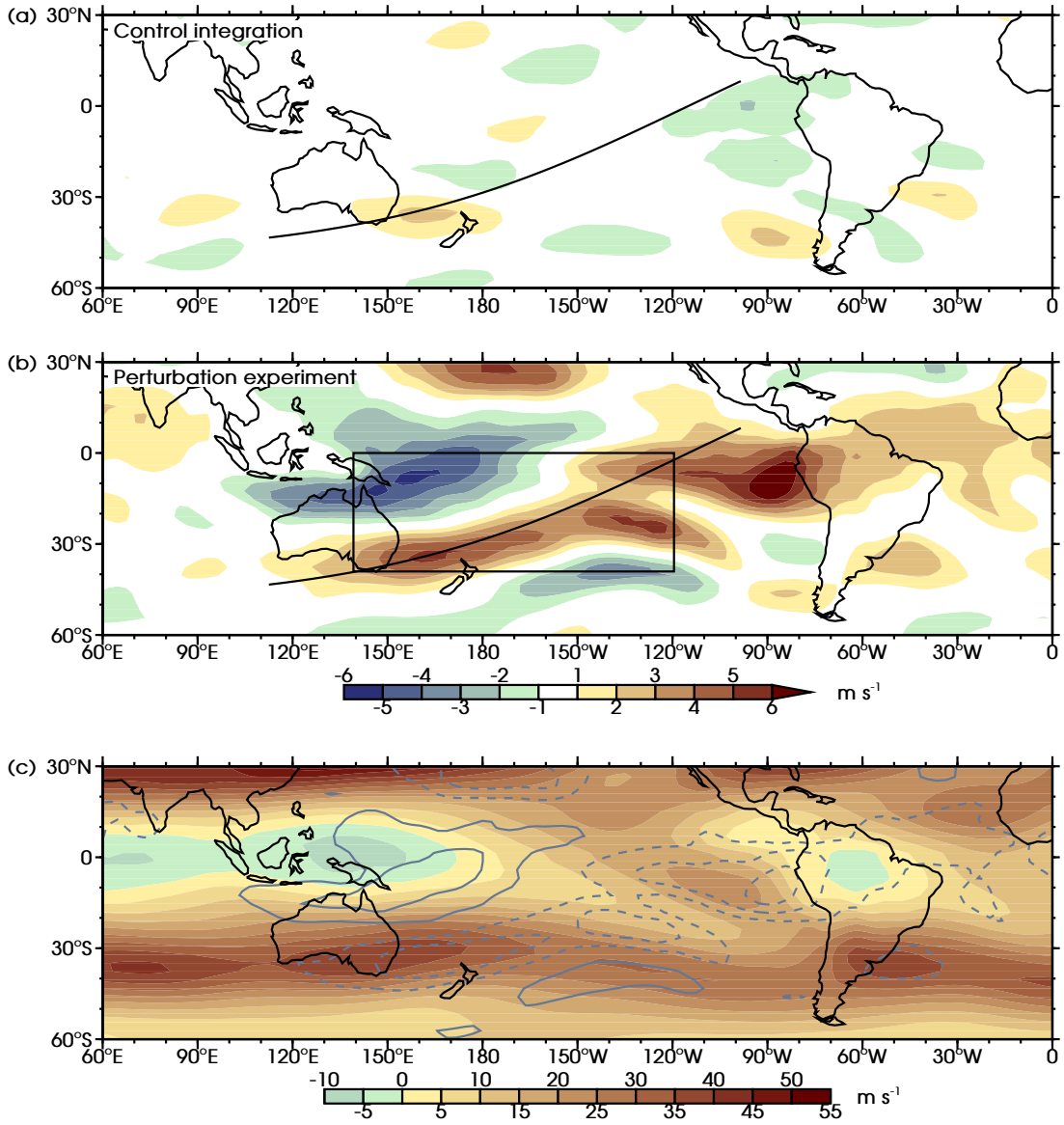

Figure 3.9: Mean 200 hPa zonal wind anomaly (m s^{-1}) over composite days event +6 days to event +10 days for the (a) control integration, and (b) the perturbation experiment. The curved line an approximate wave propagation path, the rectangle in (b) indicates the region for the perturbation experiment. (c) Time mean 200 hPa zonal wind (November to April) in the control integration in shaded colours (m s^{-1}) and SPCZ convective event wind anomaly (b) overlaid in grey contours, note the sign has been changed from (b) (2 m s^{-1} contour interval, zero contour omitted, negative contours dashed).

in the SPCZ and subsequent convective events in the SACZ in the IGCM4 control integration.

The post-convective event upper-tropospheric zonal wind anomalies in the perturbation experiment are much larger (figure 3.9b). Along the Rossby wave propagation path and over the equatorial east Pacific there are strong positive

(westerly) anomalies. To the north and south of the propagation path there are negative (easterly) anomalies. The anomaly pattern is approximately southwest-northeast, perpendicular to the prescribed heating pattern, which suggests it is not a side effect of the perturbation experiment but rather has a dynamical origin.

Figure 3.9b shows the change in zonal winds when the feedback from convective events in the SPCZ has been switched off. The climatic influence of the SPCZ is therefore the exact opposite (contours in figure 3.9c). Dashed contours show areas where the climatological westerly winds are decreased in strength, solid contours areas of increased westerly/decreased easterly winds. Convective events in the SPCZ act to decrease the strength of the westerly duct over the equatorial eastern Pacific. This suggests there is a negative feedback, as the westerly duct is partially responsible for the initial equatorward propagation of the Rossby waves. In the IGCM4 control integration the zonal windspeed in the westerly duct is ~20 m s^{-1} (colours in figure 3.9c), a change of ~ -4 m s^{-1} due to SPCZ convection is therefore an important factor in determining its strength.

3.5 DISCUSSION

The influence of convective events in the SPCZ on local Rossby wave propagation and the Pacific mean flow has been tested by means of an AGCM experiment. In observational data and in the control integration, Rossby waves trigger deep convection and precipitation in the SPCZ. In a perturbation experiment the dynamical Rossby wave forcing is decoupled from a potential thermodynamic response: instantaneous diabatic heating during SPCZ convective events is removed and replaced by a climatological value. Experimental results show continued Rossby wave propagation from the subtropical jet towards the eastern equatorial Pacific and across the equator. In the control integration and in observations these Rossby waves are dissipated in the SPCZ region due to diabatic heat release in the convection and a negative feedback due to vortex stretching. The continued Rossby propagation in the experiment provides additional evidence for the feedback mechanism in the transient wave-convection framework proposed in chapter 2.

Besides influencing transient Rossby waves locally, the experiment shows convective events in the SPCZ region have a significant impact on the south Pacific

upper-tropospheric zonal wind climate. As discussed, in the control integration and in observations, convective events in the SPCZ stop Rossby wave propagation in the region. Consequently the transport of eastward momentum towards the equatorial east Pacific is decreased, as transient Rossby waves are an important factor in the tropical momentum balance (Kiladis, 1998). The SPCZ acts as a negative feedback in the local climate system: Rossby waves are refracted equatorwards due to the equatorial westerlies; these equatorial westerlies decrease in strength due to SPCZ convection forced by these waves. In IGCM4 this decrease is ~ 4 m s^{-1} on the climatological value of ~ 20 m s^{-1}.

These results can be interpreted within the general framework of Meehl *et al.* (2001), where atmospheric processes on longer time scales and larger spatial scales set a mean atmospheric state on which synoptic waves propagate (the Rossby waves in the SPCZ in this example). In the general framework, processes on synoptic scales then influence atmospheric processes on longer time and larger spatial scales. Here, this corresponds to the band of convection that is triggered in the SPCZ feeding back on this basic state through decreased momentum transport towards the equatorial eastern Pacific.

SST biases in coupled models in the CMIP5 force a too zonal tropical part of the SPCZ, the simulated SPCZ is more discontinuous than observed (J R Brown *et al.*, 2011, 2013; Niznik *et al.*, 2015). Based on the results presented here, biases in the represented SPCZ lead to further biases in the representation of convective heating, Rossby wave propagation, momentum transport and the mean upper-tropospheric wind climate. Projections of changes in atmospheric processes in a future warmer climate are often based on these CMIP5 models, it is therefore of importance to improve the representation of the SPCZ in such models.

In chapter 4 IGCM4 is used to investigate the atmospheric boundary conditions that lead to a diagonal SPCZ. The influence of land-sea contrasts, orography and SSTs are tested. The processes that create a wrongly oriented SPCZ can be identified and maybe give information on which processes in coupled climate models need refining.

4

BOUNDARY CONDITIONS FOR A DIAGONAL SOUTH PACIFIC CONVERGENCE ZONE

This chapter is based on a paper that has been accepted for publication in Climate Dynamics with the title 'Why the South Pacific Convergence Zone is diagonal' (Van der Wiel *et al.*, 2015b). The text in the chapter is largely unchanged from the submitted paper, apart from the introduction and the model description section which have been shortened to avoid repetition of chapter 1 and section 3.2. K. van der Wiel was responsible for the work, under supervision by A.J. Matthews, M.M. Joshi and D.P. Stevens, who provided scientific input and helped revise the text for publication. The comments of two anonymous reviewer also helped to improve the manuscript.

4.1 INTRODUCTION

In chapter 3 the influence of convective events in the South Pacific Convergence Zone (SPCZ) is investigated. It is shown that changes to Rossby wave propagation and the transport of eastward momentum can be linked to these events and ultimately feedback on the Pacific mean flow. It is therefore important that the SPCZ and its variability is captured in climate models. Coupled climate models have difficulty

simulating a diagonal SPCZ. The collection of state-of-the-art models in the Coupled Model Intercomparison Project phase 5 (CMIP5) generally model a SPCZ that is too zonal and where the subtropical portion is displaced (J R Brown *et al.*, 2013; Niznik *et al.*, 2015).

There are many atmospheric processes and feedbacks that have been linked to the SPCZ; these need to be well represented in the climate models in order for them to simulate a realistic SPCZ. Low-level inflow by easterly trade winds (Lintner & Neelin, 2008; Niznik & Lintner, 2013) and orographically forced subsidence (Takahashi & Battisti, 2007b) set the location of the eastern margin of the SPCZ. Tropical-extratropical interactions by means of Rossby waves have long been associated with the SPCZ (e.g. Streten, 1973; Trenberth, 1976; Widlansky *et al.*, 2011). The framework developed in chapter 2 shows that convection in the SPCZ is forced by the equatorward propagation and the diagonal orientation of Rossby wave trains. This framework depends on a background climatological state to facilitate all aspects of the mechanism. How robust the SPCZ mechanism is to changes in the background state and what aspects of the background state cause changes to the SPCZ are still open questions.

The aim of this chapter is to determine how boundary conditions influence the background state, atmospheric dynamic and thermodynamic processes and what their effect is on the diagonal SPCZ, using an Atmospheric General Circulation Model (AGCM). Any climatological differences between the Northern and Southern Hemisphere (Intertropical Convergence Zone, ITCZ, vs. SPCZ) must be forced by differences in boundary conditions, i.e. differences in continental configuration (land-sea contrasts), orography and Sea Surface Temperatures (SSTs). In an AGCM, as used here, SSTs are an externally specified boundary condition. Of course, in a coupled model and in the actual climate system, SSTs are set by the combined effects of ocean circulation and atmosphere-ocean interactions.

The SST pattern over the Pacific has strong zonal and meridional gradients. Changes in the distribution of tropical SSTs, e.g. due to El Niño-Southern Oscillation (ENSO), have been related to changes in the position of the SPCZ (e.g. Folland *et al.*, 2002; Juillet-Leclerc *et al.*, 2006; Vincent *et al.*, 2011; Haffke & Magnusdottir, 2013). During El Niño events, when warm water from the equatorial warm pool moves eastward, decreasing the zonal SST difference, the SPCZ moves eastward and

equatorward. During La Niña events, when zonal SST asymmetries in the equatorial Pacific are magnified, the SPCZ moves westward and poleward (figure 1.4). For strong El Niño events the SPCZ disappears in favour of a zonal precipitation band close to the equator (Vincent *et al.*, 2011). These 'zonal SPCZ' events are predicted to occur more frequently in future warmer climates (Cai *et al.*, 2012; Borlace *et al.*, 2014).

The direct influence of orography on the SPCZ is not as clear. Takahashi & Battisti (2007a,b) and Kitoh (2002) tested this by means of coupled model experiments. Though the SPCZ proved to be sensitive to adding/removing orography, it was not possible to separate the direct effect of the Andes on atmospheric processes from the indirect effect of the Andes through altered SSTs on atmospheric processes. The role of southern Pacific land-sea contrasts was tested in experiments by Kiladis *et al.* (1989), though again Pacific SSTs were altered as well. It was concluded that the presence of Australia alters precipitation rates in the western part of the SPCZ and that South America has no influence. The experiments in this study have been designed to test the direct effects of all boundary conditions separately. Indirect effects of orography and land-sea contrasts, through altered SSTs, are not be considered.

The remainder of the chapter is organized as follows: in section 4.2 the ability of the Intermediate Global Circulation Model version 4 (IGCM4) to simulate the diagonal SPCZ is discussed. In section 4.3 the different experiments are described. Experimental results are shown in section 4.4 and a final discussion of the findings is given in section 4.5.

4.2 MODEL VERIFICATION

As in chapter 3 IGCM4 (Joshi *et al.*, 2015) is used here, see section 3.2 for a detailed model description. A quantitative comparison of the SPCZ orientation is obtained following the approach of J R Brown *et al.* (2011, 2012, 2013). In the domain where the SPCZ is well defined (155°E to 140°W, 0° to 30°S), the latitude of maximum precipitation is found for each band of longitude. A linear least-squares fit to the resulting points gives an objective estimation of the latitudinal position of the SPCZ mean precipitation axis and its slope (in °N/°E). There is no threshold of minimum precipitation for the selected points, as the focus here is mostly on investigating the diagonal orientation of the SPCZ, independent from its strength. Therefore, the SPCZ

strength is defined separately as the mean precipitation rate in a parallelogram along the fitted mean precipitation axis. The width of the parallelogram is 10° of latitude (see black boxes in figures 4.1a and 4.1b).

First, the characteristics of the SPCZ in a control experiment are described. The November to April time mean precipitation for observations and in the IGCM4 control integration is shown in figures 4.1a and 4.1b. The observations are based on the precipitation product from the Climate Prediction Center Merged Analysis of Precipitation (CMAP) project (Xie & Arkin, 1997), from 1979 to 2008 on a 2.5°×2.5° grid (see section 2.2). In the climate of the IGCM4 control integration, the position of the 4 mm d^{-1} contour, a proxy for the SPCZ margin, is simulated well at the northern boundary of the SPCZ, although the simulated SPCZ southern boundary is located too far east. The slope of the SPCZ mean precipitation axis is −0.37°N/°E in the control integration, which is slightly more slanted than the observed SPCZ (−0.27°N/°E). The precipitation rate is underestimated in the more tropical part of the SPCZ, resulting in a mean SPCZ strength of 7.50 mm d^{-1} instead of 9.25 mm d^{-1} in CMAP. The computed SPCZ strength is plotted against SPCZ slope in figure 4.1c. For a quality comparison of the modelled SPCZ in IGCM4, the data from 23 CMIP5 models are also included (more details on the CMIP5 models and climatological mean maps are included in appendix A). The quality of the SPCZ based on strength and slope in the IGCM4 control integration is within the range of CMIP5 atmosphere only ('AMIP') experiments. The coupled version of these models ('historical' experiment) simulate an SPCZ that is too zonal (J R Brown *et al.*, 2013), from the models taken into account here only MIROC5 and CMCC-CM simulate a diagonal SPCZ in coupled mode (slope < −0.1°N/°E).

A second diagonally oriented precipitation band can be found over South American continent and the southern Atlantic Ocean. The South Atlantic Convergence Zone (SACZ) is formed by a comparable dynamical mechanism as the SPCZ (chapter 2). In the control integration (figure 4.1b) the SACZ slope is similar to the observed slope. Simulated precipitation values are higher in the continental part of the SACZ and lower in the oceanic part. Precipitation in the ITCZ over the Pacific is slightly weaker than observed.

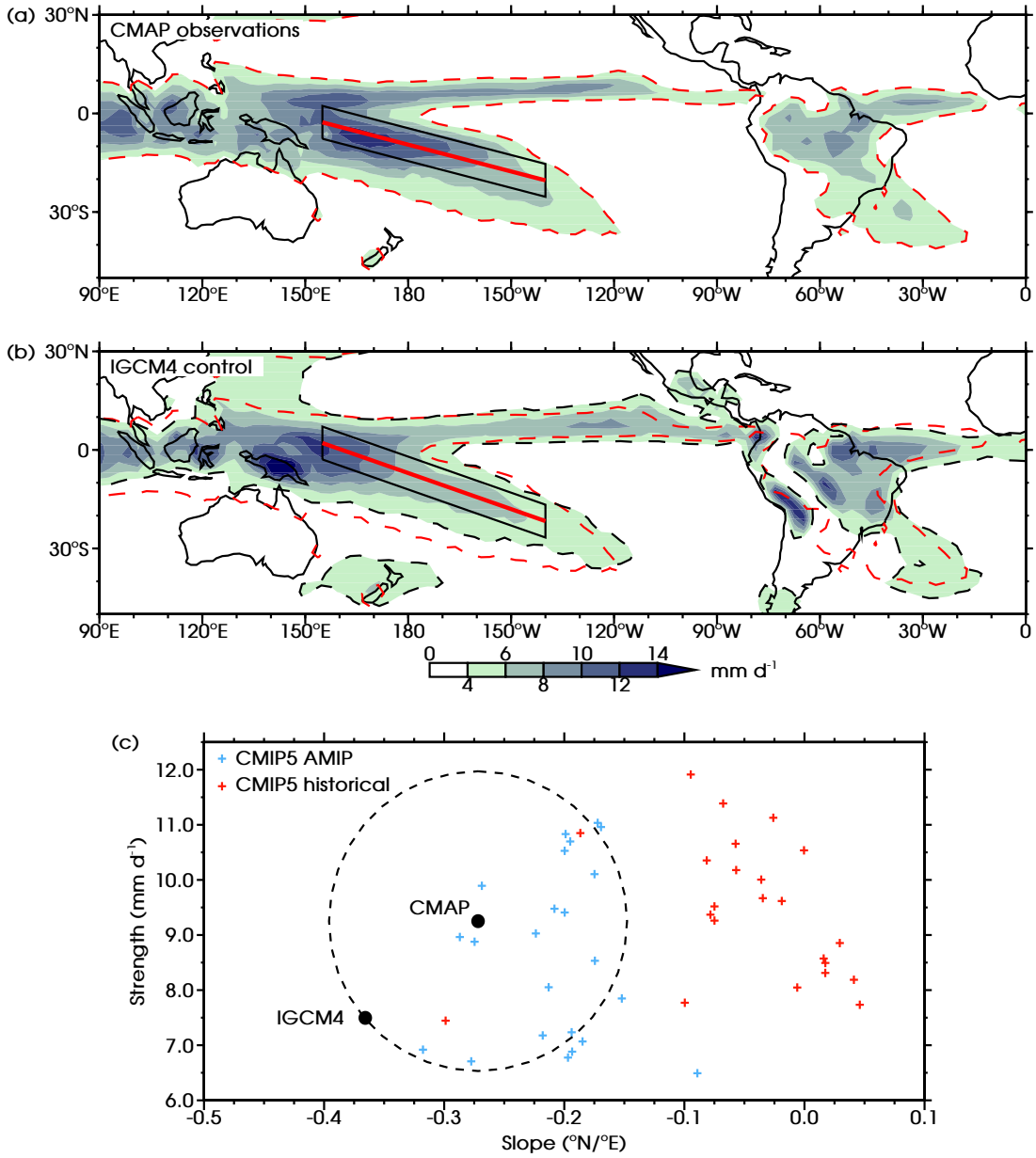

Figure 4.1: Time mean precipitation rate (November to April) in (a) CMAP and (b) IGCM4 control integration (shaded colours, mm d^{-1}). The thick diagonal red lines in (a,b) show the computed SPCZ mean precipitation axis locations, the red dashed lines in (a,b) show the 4 mm d^{-1} contour in CMAP, the black dashed line in (b) shows this contour in the IGCM4 control integration, black parallelograms in (a,b) are the area for the computation of the SPCZ strength (see text). (c) SPCZ strength (mm d^{-1}) plotted against SPCZ slope (°N/°E). Black dots are the CMAP observations and the IGCM4 control integration, additionally CMIP5 AMIP experiments (blue crosses) and CMIP5 historical experiments (red crosses) are shown. The dashed line in (c) is the circle centred on the CMAP observations that passes through the point of the IGCM4 control integration.

4.3 EXPERIMENTAL SETUP

Four different sets of experiments were designed to separately test the influence of SST asymmetries, absolute SST values, orography and land-sea contrasts on the diagonal SPCZ orientation and strength. The model setup for each of these experiments is described below (see also table 4.1).

Table 4.1: Overview of IGCM4 experiments conducted.

Experiment	Description
Control	Standard IGCM4
SST asymmetry	Zonal mean SSTs + SST asymmetry (α)
Absolute SST	Standard SST patterns + absolute change (β)
No orography	Earth without mountains
No land	- No Australia, New Zealand and maritime continent - No South America

4.3.1 SST ASYMMETRY

This set of model integrations varies the strength of the zonally asymmetric part of the SST field, i.e. the zonal SST gradients. First, the zonal mean SST field (SST_{zm}) is calculated. For a given latitude, the zonal mean SST is the mean SST over all the ocean grid points along that particular latitude. The asymmetric part of the SST field (SST_{asym}) is the difference between the total (SST_{ctrl}) and zonal mean fields:

$$SST_{asym} = SST_{ctrl} - SST_{zm}. \tag{4.1}$$

These calculations are carried out globally, for each month in the seasonally varying SST climatology. Finally, the strength of the zonally asymmetric SST field used in the experiments is determined by the dimensionless parameter α:

$$SST_{exp} = SST_{zm} + \alpha \times SST_{asym}. \tag{4.2}$$

The model linearly interpolates the monthly SST fields onto the relevant model Julian day. Integrations were carried out for α in the range $-0.5 \leq \alpha \leq 2$. Here, $\alpha = 0$

corresponds to the zonal mean SST field, $\alpha = 1$ corresponds to the control integration, $0 < \alpha < 1$ and $\alpha > 1$ corresponds to weaker and stronger SST gradients, respectively, and $\alpha < 0$ corresponds to reversed SST gradients.

4.3.2 ABSOLUTE SST

This is a series of integrations with globally increasing or decreasing SST values, set by the parameter β (°C):

$$SST_{exp} = SST_{ctrl} + \beta. \tag{4.3}$$

A range of IGCM4 integrations has been completed for β in the range $-12°C \leq \beta \leq +8°C$. Note that by definition $\beta = 0°C$ is the control integration.

4.3.3 NO OROGRAPHY

This experiment was run with all mountains removed; all land surface is flat.

4.3.4 NO LAND

Some of the land surface is changed into ocean. Instead of calculating surface temperatures interactively, monthly mean surface temperatures are prescribed, by linearly interpolating east to west from (former) coast to coast. Orography is preserved as in the control integration, i.e. mountains on the removed continents are now 'aqua mountains'. Two separate integrations have been done: (i) removing Australia, New Zealand and the maritime continent and (ii) removing South America.

4.4 EXPERIMENTAL RESULTS

4.4.1 SST ASYMMETRY

LARGE-SCALE IMPACT ON THE SPCZ

Zonal and meridional SST gradients have been linked to the diagonally oriented SPCZ in many studies (e.g. Widlansky *et al.*, 2011, 2013; Nieto Ferreira & Chao, 2013). Hence ten integrations with either increased zonal SST asymmetry ($\alpha > 1$) or decreased asymmetry ($\alpha < 1$) are conducted. The SST fields forcing the model are shown in

figure 4.2. Note that $\alpha = 1$ is the control integration and $\alpha = 0$ has zonally symmetric SST forcing. For $\alpha = 2$ any departures from the zonal mean SST values are doubled, the west Pacific warm pool is warmer, the east Pacific cold tongue is colder. For each longitudinal band the zonal mean SST value remains constant.

For increasing asymmetry the SPCZ remains in position; the slope is $-0.26°\text{N}/°\text{E}$ and the strength increases up to 12.00 mm d^{-1} for $\alpha = 2$. The precipitation rate increases along the entire length of the SPCZ, consequently the southeastern tip extends about 10° further eastward. In the Northern Hemisphere the ITCZ is weaker compared to the control integration. In figure 4.3a the mean precipitation mid-SPCZ (15°-25°S) is shown for all integrations in the SST asymmetry experiment. For $\alpha \geq 1$ the strength increases steadily and the longitude at which maximum precipitation is found does not shift.

Zonally symmetric SST forcing ($\alpha = 0$) does not support any form of a diagonally oriented SPCZ. Precipitation over the Pacific Ocean is focused in one broad band situated over the equator (figure 4.2d). The strongest precipitation rate is just north of the equator. Three model integrations were performed spanning the range from the control integration to the zonally symmetric SST integration. For $\alpha = 0.75$ (not shown) both SPCZ strength and orientation are very close to the SPCZ in the control integration. For $\alpha = 0.5$ (figure 4.2f) the SPCZ strength is much weaker. Though there is a weak sign of diagonally oriented precipitation, the SPCZ identification criteria from J R Brown *et al.* (2011, 2012, 2013) fail to identify it, precipitation just south of the equator is stronger and therefore selected as the SPCZ mean precipitation axis. Finally, for $\alpha = 0.25$ (not shown) there is no evidence of a diagonally oriented precipitation pattern. The critical value required for a diagonal SPCZ lies therefore somewhere around $\alpha = 0.5$. The shift of the SPCZ at $\alpha = 0.5$ is also visible in figure 4.3a.

For the integration with $\alpha = -0.5$ the zonal SST gradients are reversed, the warmest water is now over the equatorial east Pacific. The strongest precipitation rates are found over the warmest waters; there is no diagonal SPCZ.

Figure 4.3b shows the zonal mean precipitation rate over the Pacific Ocean (150°E-90°W). In the control integration, the maximum precipitation rate is in the ITCZ at 5°N. In the Southern Hemisphere there is no clear maximum, instead there is a steady decrease in precipitation rate towards a minimum at 30°S. Between 12°and 25°S the

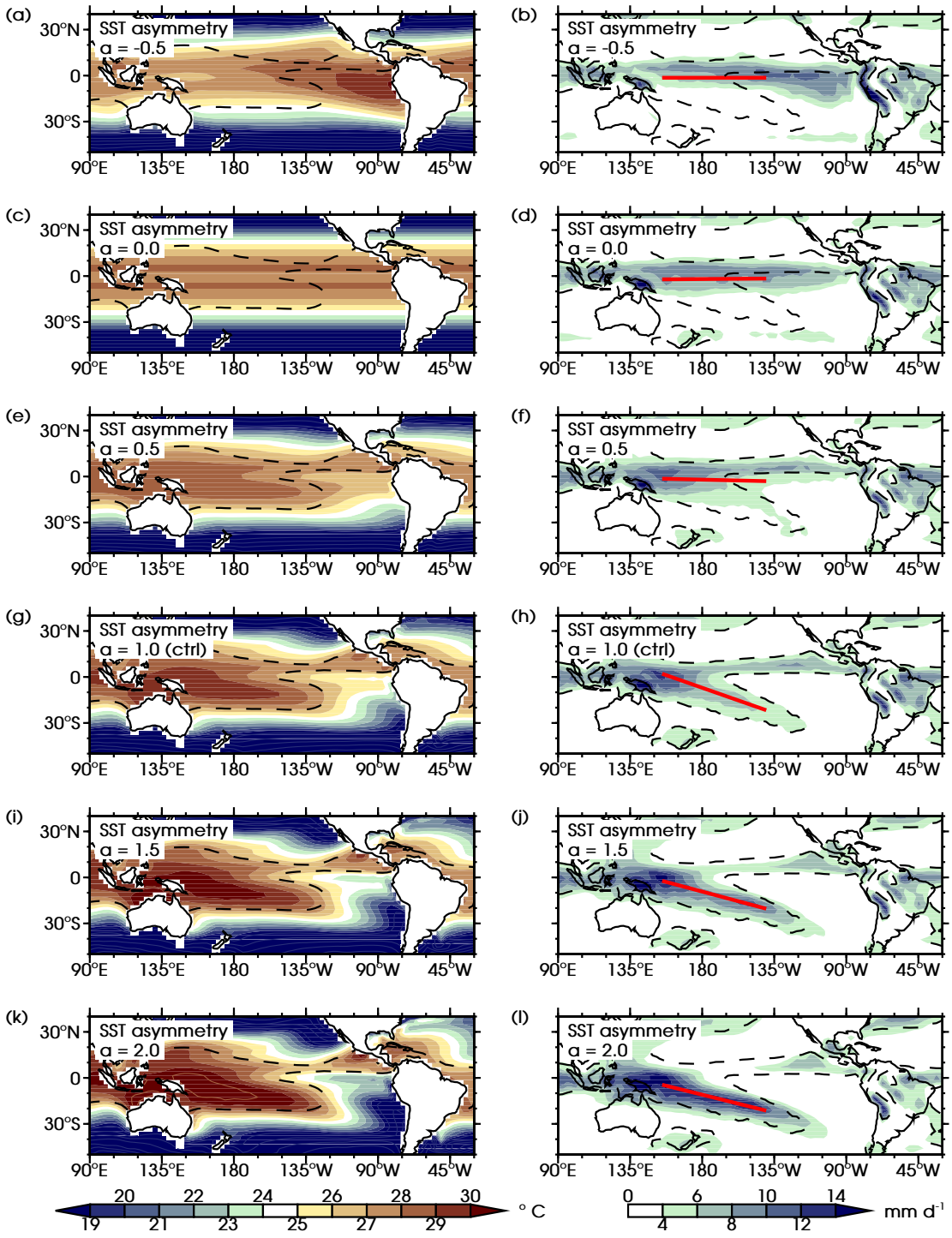

Figure 4.2: SST asymmetry experiments. (Left) Time mean SST forcing (November to April, shaded colours, °C), black dashed line shows the 27°C contour of the IGCM4 control integration (as in g), brown line contours show SST contours for 31°C and warmer (+1°C contour interval), blue line contours show SST contours for 17°C and colder (-2°C contour interval). (Right) The corresponding time mean precipitation rate (shaded colours, mm d^{-1}), the thick diagonal red line shows the computed SPCZ mean precipitation axis location, the black dashed line shows the 4 mm d^{-1} contour of the IGCM4 control integration (as in h). (a,b) $\alpha = -0.5$, (c,d) $\alpha = 0$, (e,f) $\alpha = 0.5$, (g,h) $\alpha = 1$, control integration, (i,j) $\alpha = 1.5$, (k,l) $\alpha = 2$.

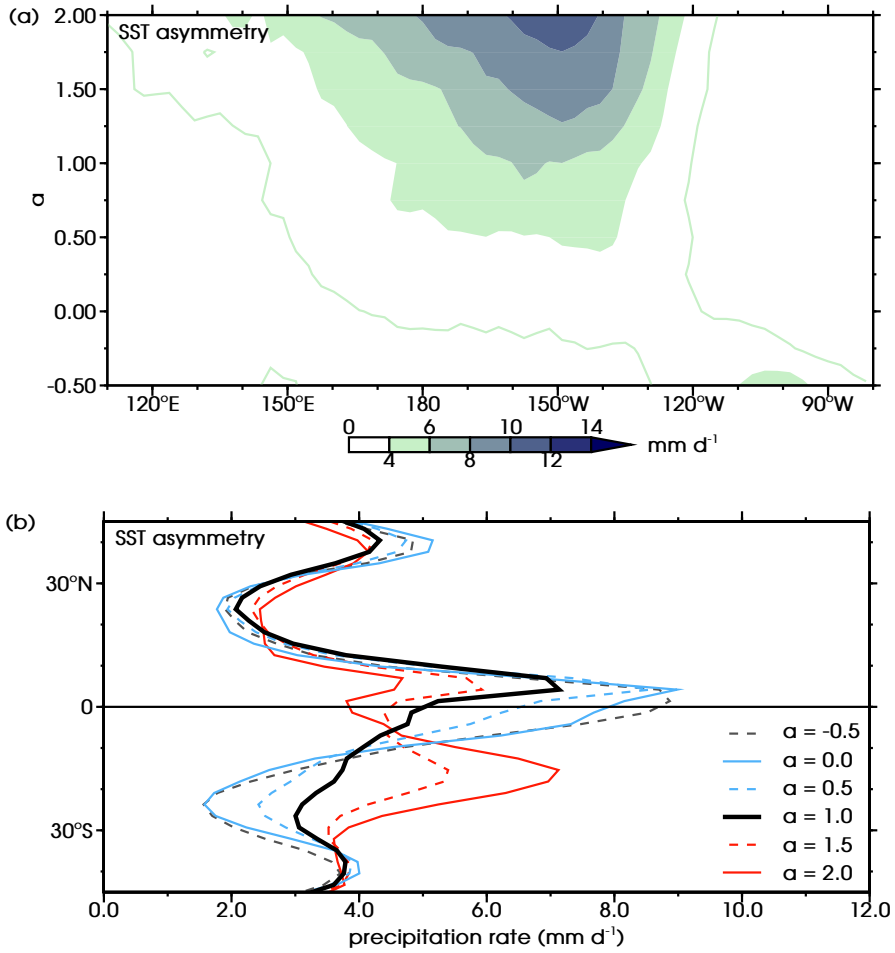

Figure 4.3: SST asymmetry experiments. (a) Time mean precipitation rate (November to April) between 15°–25°S (shaded colours, mm d^{-1}). The green line shows the 2 mm d^{-1} contour. (b) November to April time-mean longitude-mean (150°E–90°W) precipitation rate (mm d^{-1}). Grey dashed line $\alpha = -0.5$, blue solid line $\alpha = 0$, blue dashed line $\alpha = 0.5$, black solid line $\alpha = 1$, control integration, red dashed line $\alpha = 1.5$, red solid line $\alpha = 2$.

SPCZ reduces the decrease of the precipitation rate with latitude. The integrations with a weakened zonal SST asymmetry (low α, blue lines) show an accentuation of this pattern. The SPCZ bump decreases in strength, the near-equatorial maxima increase in strength. For integrations with an increasing SST asymmetry (high α, red lines), the near-equatorial maxima are weaker and the SPCZ bump increases in strength, such that by $\alpha = 1.5$ it becomes a distinct local maximum. For $\alpha = 2$ the overall maximum is no longer in the Northern Hemisphere ITCZ, instead it is at about 15°S in the SPCZ. In these experiments, the precipitation rate in the SPCZ is inversely related to the precipitation rate in the ITCZ: increasing SST asymmetry result in stronger SPCZ and weaker ITCZ precipitation (figure 4.2).

IMPACT ON TRANSIENT WAVE-CONVECTION SPCZ FRAMEWORK

As the zonal asymmetry (α) is decreased, the diagonal SPCZ disappears. However, the SPCZ is not a direct convective response to the underlying SST distributions. As discussed in chapter 2 the climatological SPCZ arises from the superposition of many individual synoptic events, where extratropical Rossby waves are refracted and take on a diagonal orientation, triggering convection in a diagonal band ahead of the cyclonic vorticity axis. In this section, it is investigated which of the links in this mechanism are sensitive to the SST changes and ultimately cause the SPCZ to disappear as the SST zonal asymmetry is reduced.

Adapting the methodology of chapter 2, composite cycles of the transient wave – convection SPCZ framework were constructed for the control experiment (figure 4.4, left) and the zonally symmetric SST experiment (figure 4.4, right). Composites were defined to find whether dynamic changes, thermodynamic changes or a mix of the two cause the diagonal SPCZ to disappear when the model is forced with zonal SSTs.

These composites are based on time series of 200-hPa vorticity anomalies (mean values in a box southwest of the SPCZ, 20°–30°S, 180°–170°W, southwest blue box in figure 4.4e). Events are then selected based on two criteria: (i) the vorticity anomaly is more negative than -1 standard deviation, and (ii) the vorticity anomaly is a relative minimum compared to five days before and after the event. Based on the above criteria 157 events were selected in the control integration and 158 events in the zonally symmetric SST integration. Composites were computed by taking the mean of a field over all event days.

In the control integration ($\alpha = 1$), four days before the event a wave train originating in the subtropical jet is refracted towards the SPCZ area (figures 4.4a and 4.4c). At the day of the event (figure 4.4e), ahead of a cyclonic vorticity anomaly precipitation is formed within the SPCZ. The wave train then weakens and deflects to the southeast (figures 4.4g and 4.4i). This is in agreement with the physical mechanism and the negative feedback between Rossby wave propagation and precipitation discussed in chapter 2.

In the zonally symmetric SST integration ($\alpha = 0$) a comparable wave train propagates over the SPCZ region (figures 4.4b and 4.4d). However, here it does not trigger significant convection and precipitation over the SPCZ region (figure 4.4f). The negative feedback does not act and wave propagation continues towards the equator

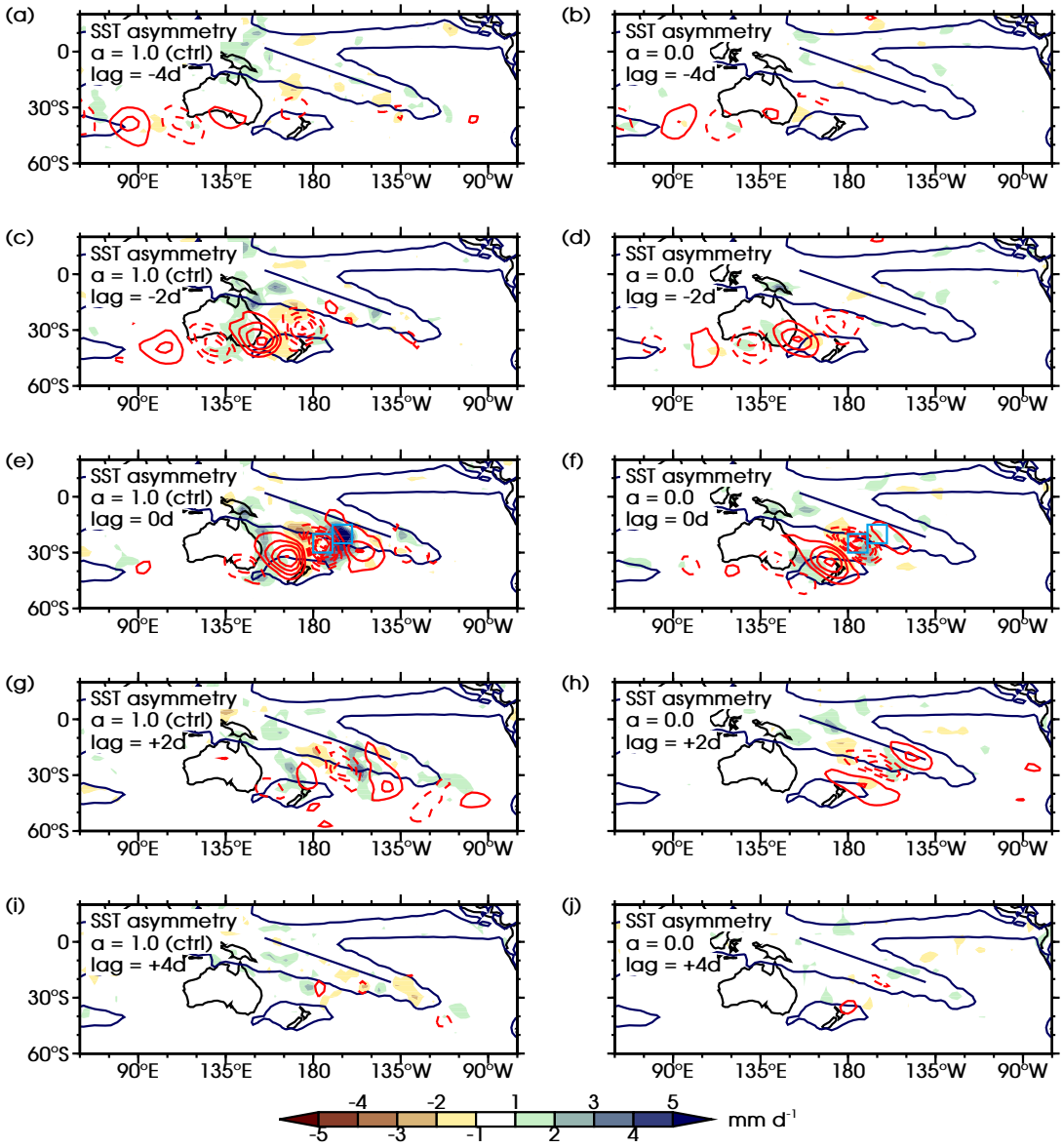

Figure 4.4: SST asymmetry experiments. Lagged composites of anomalies of 200 hPa vorticity (contours, interval 7.5×10^{-6} s^{-1}, negative contours dashed, zero contour omitted) and precipitation rate (shaded colours, mm d^{-1}). Dark blue lines show the SPCZ mean precipitation axis and the 4 mm d^{-1} contour in the control integration (as in figure 4.1b), light blue boxes in (e,f) are area for the vorticity time series and vertical profiles (see text). (a,c,e,g,i) $\alpha = 1$, control integration, (b,d,f,h,j) $\alpha = 0$. Lags: (a,b) event −4 days, (c,d) event −2 days, (e,f) event, (g,h) event +2 days, (i,j) event +4 days.

(figures 4.4h and 4.4j), as was also found in the perturbation experiment in chapter 3. The Rossby wave forcing up to the event is similar between the two integrations. Therefore, there must be a difference in the thermodynamics that causes the SPCZ to disappear when the model is forced by zonal SSTs.

Vertical profiles of temperature and humidity have been analysed in the location where the dynamical forcing triggers precipitation in the composites in the control integration (northeast light blue box in figure 4.4e, 15°-25°S, 170°-160°W). Both temperature (figure 4.5a) and specific humidity (figure 4.5b) are lower in the zonally symmetric SST integration; the resulting decrease of relative humidity (figure 4.5c) is substantial. Decreased moisture in the lower troposphere results in a smaller convective adjustment (see section 3.2.2) and produces less precipitation.

The difference in atmospheric humidity can be explained by differences in atmospheric moisture supply. In the control integration, the lower-tropospheric flow over the Southern Hemisphere subtropical Pacific is dominated by a strong subtropical anticyclone (wind vectors in figure 4.6a). On the large scale, the lower-tropospheric humidity is characterised by the moist tropics and drier subtropics (shading in figure 4.6a). The subtropical anticyclone advects dry air equatorwards in the eastern Pacific. On its western flank moist air is advected polewards into the SPCZ region. This moisture then converges along the SPCZ mean precipitation axis (figure 4.6c), supplying the moisture for the convection ahead of the transient waves in figure 4.4e.

In the zonally symmetric SST integration, the lower-tropospheric circulation response over the South Pacific is also approximately zonally symmetric. There is no distinct subtropical anticyclone over the eastern Pacific, and the subtropical flow is eastward and equatorward (trade winds) at all longitudes across the Pacific (wind vectors in figure 4.6b). Hence, there is no poleward moisture advection in the southwest Pacific and no moisture convergence to feed an SPCZ (figure 4.6d). Therefore, even though the dynamical forcing from transient waves over the southwest Pacific is still present (figure 4.4f), the moisture supply needed for this to trigger the deep convective events that comprise the SPCZ is absent.

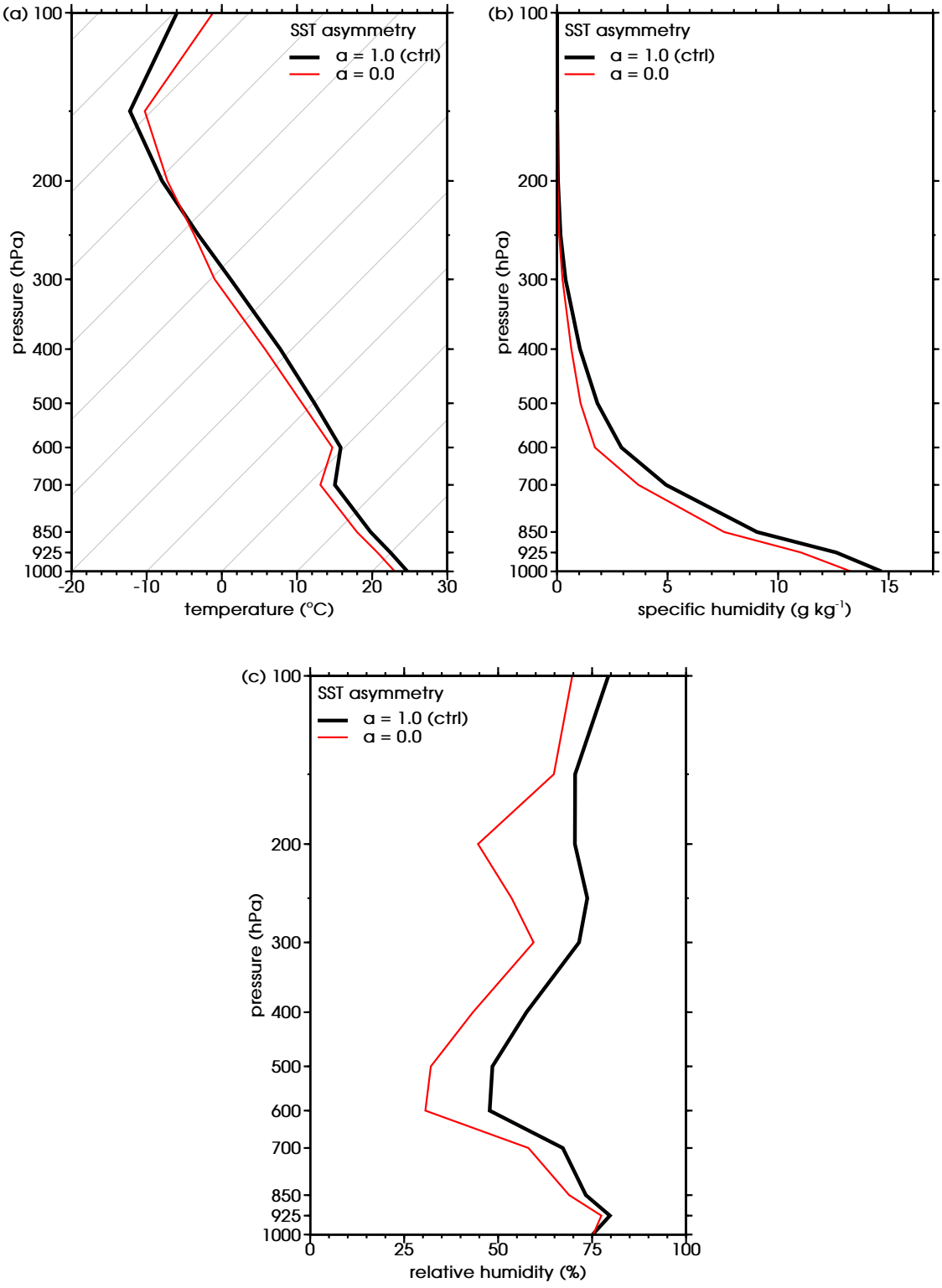

Figure 4.5: SST asymmetry experiments. Vertical profiles of (a) temperature (°C), (b) specific humidity (g kg^{-1}) and (c) relative humidity (%) in the northeastern blue box (see figures 4.4e and 4.4f) in the composites (event, no lag). Temperature is plotted on a Skew T-log P diagram, skew grey lines are isotherms. $\alpha = 1$, control integration, black line and $\alpha = 0$ red line.

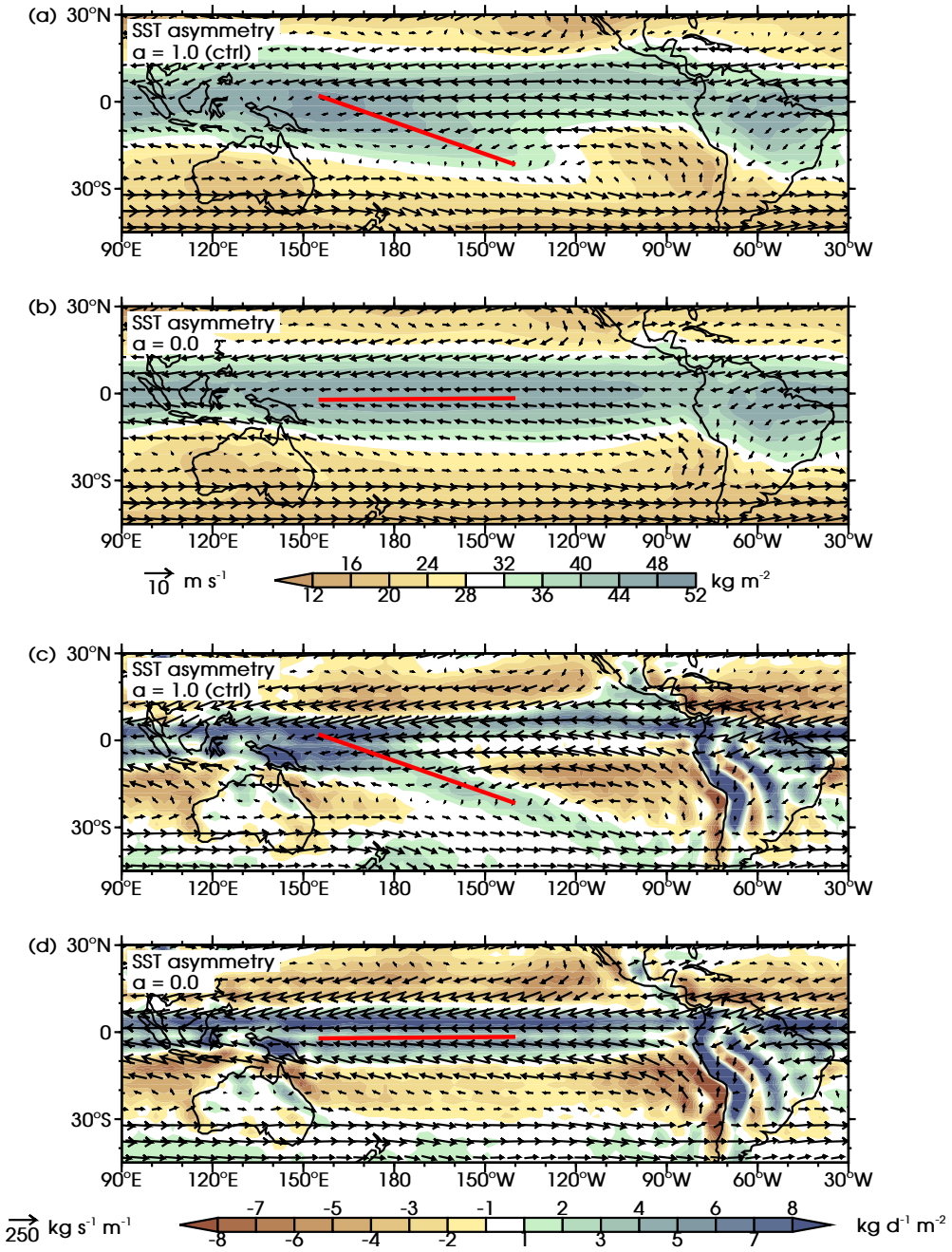

Figure 4.6: SST asymmetry experiments. (a,b) time mean column integrated specific humidity (November to April, shaded colours, kg m^{-2}) and 1000–600 hPa mean wind (vectors, m s^{-1}, reference vector bottom left). (c,d) the corresponding column integrated moisture transport (vectors, kg s^{-1} m^{-1}, reference vector bottom left) and moisture convergence (shaded colours, kg d^{-1} m^{-2}). (a,c) $\alpha = 1$, control integration, (b,d) $\alpha = 0$. The thick diagonal red lines show the computed SPCZ mean precipitation axis location.

4.4.2 ABSOLUTE SST

Ten integrations have been performed in the absolute SST experiment, with SST values changing from $\beta = -12°C$ to $\beta = +8°C$. For a selection of these integrations the new SST fields forcing for the model and the resulting precipitation patterns are shown in figure 4.7. Within this 20°C range of temperatures, the SPCZ is a constant feature over the southern Pacific. For $-4°C \leq \beta \leq +8°C$ its diagonal orientation is stable, with the slope varying between $-0.27°N/°E$ and $-0.37°N/°E$. For the integrations with β decreasing beyond $-6°C$, the slope decreases from $-0.36°N/°E$ to $-0.08°N/°E$ ($\beta = -12°C$) and the SPCZ loses most of its diagonal orientation. Overall, the SPCZ precipitation rate increases with warmer SSTs, from 5.05 mm d^{-1} ($\beta = -12°C$) to 9.39 mm d^{-1} ($\beta = +8°C$). Precipitation over ocean surfaces outside the SPCZ changes in a similar way. The ITCZ, the oceanic portion of the SACZ and precipitation over the maritime continent all decrease or disappear with cooling SSTs.

In IGCM4 the convective precipitation rate is determined by the atmospheric stability and moisture content. Convective Available Potential Energy (CAPE) provides an estimate of the likelihood and the intensity of atmospheric convection (Riemann-Campe *et al.*, 2009). Based on model output, CAPE is computed from vertical profiles of temperature and surface humidity. Figure 4.8 shows mean vertical temperature profiles along the SPCZ for $\beta = -8°C$, $\beta = 0°C$ and $\beta = +8°C$. In the control integration CAPE is 1827 J kg^{-1}. In the warmer experiment both temperature and specific humidity have increased throughout the troposphere. The idealised lifted parcel shows convection is deeper and, as shown before, produces more precipitation (figure 4.7l). The CAPE for this profile is 3047 J kg^{-1}. In the colder experiment temperature and specific humidity decrease and the tropopause height is lower. CAPE decreases to 996 J kg^{-1}, convection is shallower and precipitation is weaker. Other integrations in this experiment show similar trends of temperature, moisture content and CAPE.

The convective inhibition, a measure for the stability of the surface layer, remains approximately constant in all experiments at about 31 J kg^{-1}. Any changes to modelled convection must therefore have been caused by changes to atmospheric temperature, moisture content and CAPE.

In general, the model atmospheric response to globally warming SSTs is an

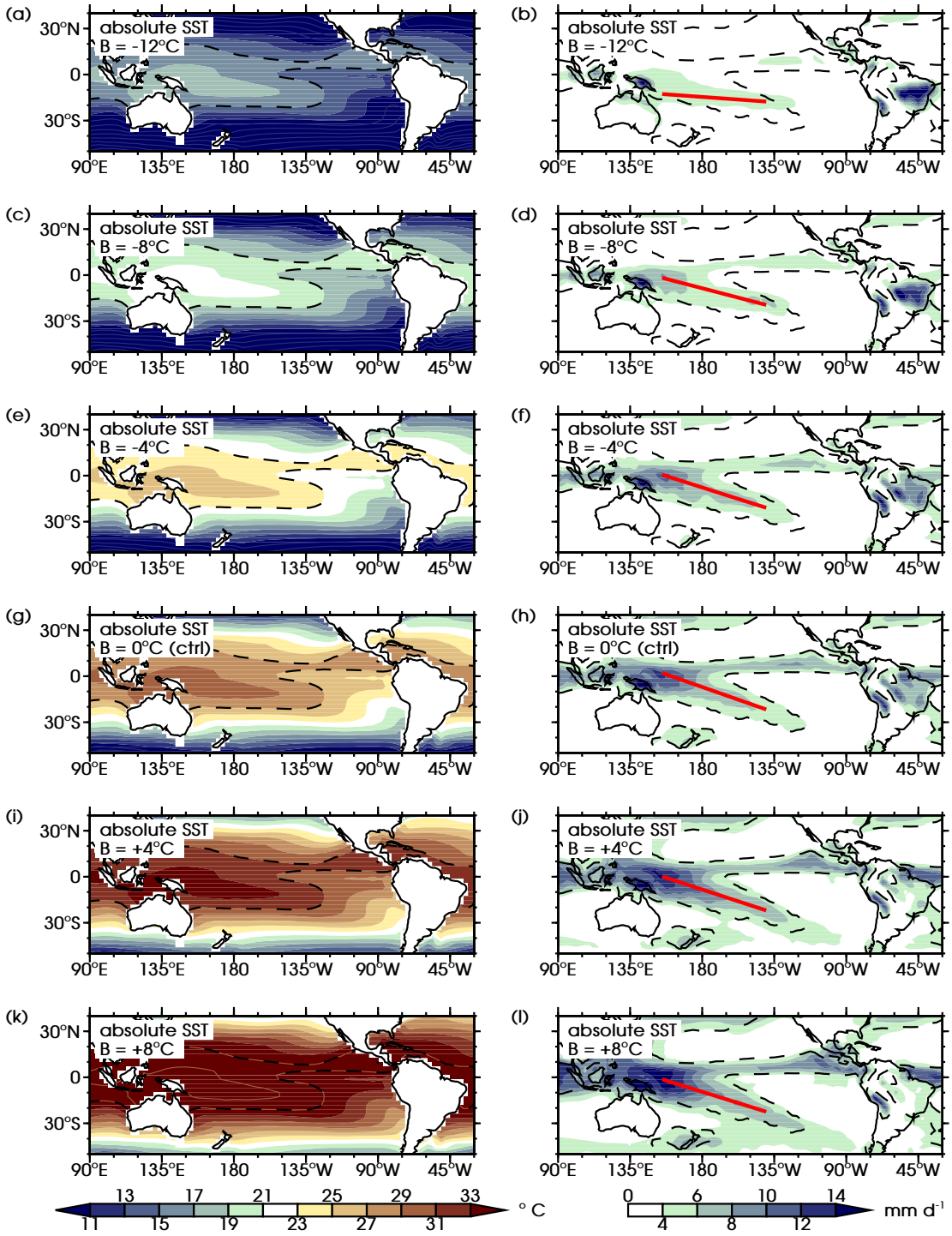

Figure 4.7: Absolute SST experiments. (Left) Time mean SST forcing (November to April, shaded colours, °C), black dashed line shows the 27°C contour of the IGCM4 control integration (as in g), brown line contours show SST contours for 35°C and warmer (+2°C contour interval), blue line contours show SST contours for 9°C and colder (-2°C contour interval). (Right) The corresponding time mean precipitation rate (shaded colours, mm d^{-1}). The thick diagonal red line shows the computed SPCZ mean precipitation axis location, the black dashed line in shows the 4 mm d^{-1} contour of the IGCM4 control integration (as in h). (a,b) $\beta = -12°C$, (c,d) $\beta = -8°C$, (e,f) $\beta = -4°C$, (g,h) $\beta = 0°C$, control integration, (i,j) $\beta = +4°C$, (k,l) $\beta = +8°C$.

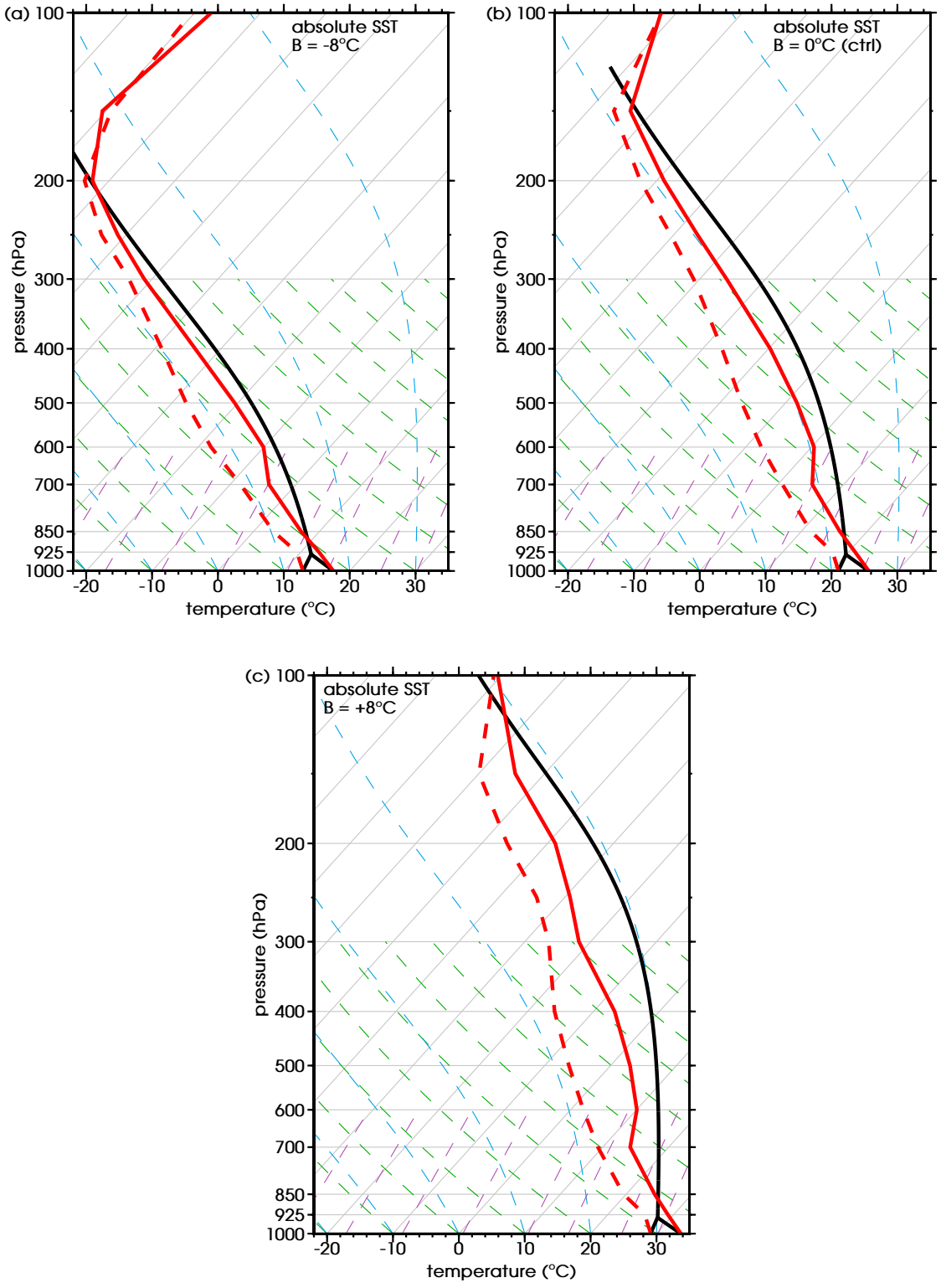

Figure 4.8: Absolute SST experiments. Time mean vertical profiles of temperature (November to April, °C, solid red line) and dewpoint temperature (°C, dashed red line) along the computed SPCZ mean precipitation axis plotted on a Skew T-log P diagram. An idealised lifted air parcel is shown as a black line. Horizontal grey lines are isobars, skew grey lines are isotherms, green dashed lines are dry adiabats, blue dashed lines are saturated adiabats, purple dashed lines are isopleths of saturation mixing ratio. (a) $\beta = -8°C$, (b) $\beta = 0°C$, control integration, (c) $\beta = +8°C$.

increase in atmospheric temperature and moisture content. As a result CAPE increases and modelled convection is deeper and produces more precipitation. The mechanism is similar to that of the 'wet gets wetter' scenario (Held & Soden, 2006) and projections of future warmer climates in CMIP5 (Widlansky *et al.*, 2013, figure 1.5). Lower-tropospheric relative humidity remains constant. The mean precipitation change along the SPCZ is approximately 0.24 mm d^{-1} $°C^{-1}$.

For negative β, CAPE values decrease all over the South Pacific (figure 4.9). The highest values of CAPE are found in two zonal bands just off the equator, separated by a minimum over the equator. Additionally, in the Southern Hemisphere high CAPE values are found further poleward in a slightly diagonal band. The diagonal SPCZ does not follow this band of high CAPE, it is more diagonally oriented (i.e. it has larger slope in °N/°E). The SPCZ slope is still set by northwest-southeast oriented vorticity centres in Rossby wave trains. Ahead of the cyclonic anomalies, static stability is reduced and, when conditions are suitable, deep convection is triggered parallel to the axis of the vorticity centre.

For extremely cold integrations ($\beta < -6°C$) the SPCZ becomes gradually weaker and loses its diagonal orientation (figure 4.7). The colder and drier atmosphere makes conditions less favourable for deep convection. At the southeastern end of the SPCZ, within the 4 mm d^{-1} margin (25-35°S, 120-130°W, light blue box in figure 4.9a), CAPE decreases from 1085 J kg^{-1} in the control integration to 789 J kg^{-1} for $\beta = -4°C$, 485 J kg^{-1} for $\beta = -8°C$ and 342 J kg^{-1} for $\beta = -12°C$. In the extremely cold integrations, the SPCZ starts to align with the highest CAPE values over the South Pacific, as the conditions at the southeastern end of the control SPCZ are no longer suitable for deep convection. In the other integrations, CAPE values are sufficiently high everywhere equatorward of 30°S to support deep convective precipitation. Consequently, the SPCZ is found wherever the dynamic forcing from the equatorward propagating Rossby waves is.

4.4.3 NO OROGRAPHY

In the no-orography experiment, the SPCZ mean precipitation axis remains in approximately the same position as in the control integration and its diagonal orientation is almost unchanged (−0.36°N/°E; figure 4.10). The mean precipitation

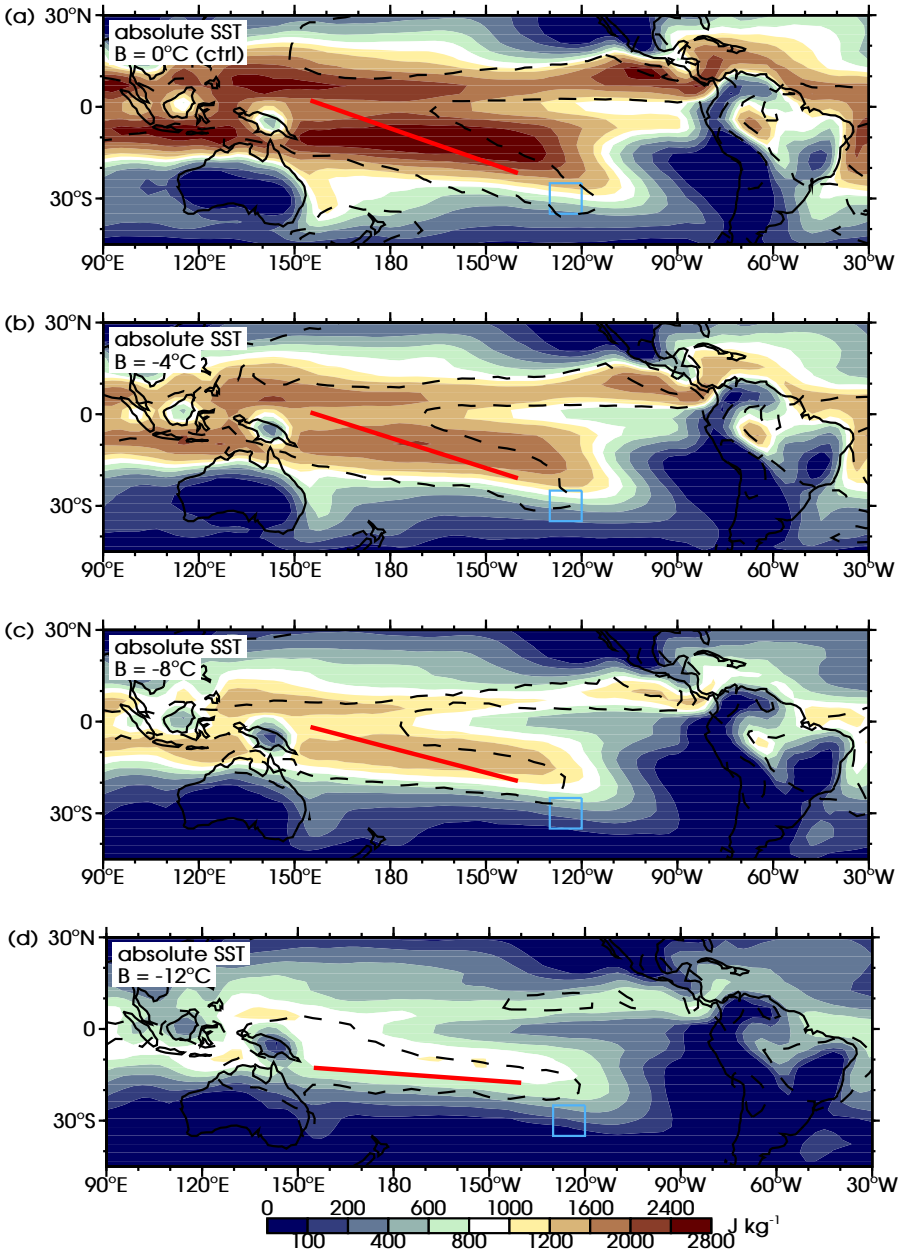

Figure 4.9: Absolute SST experiments. Time mean CAPE (November to April, shaded colours, J kg^{-1}). The thick diagonal red lines show the computed SPCZ mean precipitation axis location, the black dashed line in shows the 4 mm d^{-1} precipitation contour (as in figure 4.7), the light blue boxes are the area for the computation of the mean CAPE value (see text). (a) $\beta = 0°$C, control integration, (b) $\beta = -4°$C, (c) $\beta = -8°$C, (d) $\beta = -12°$C.

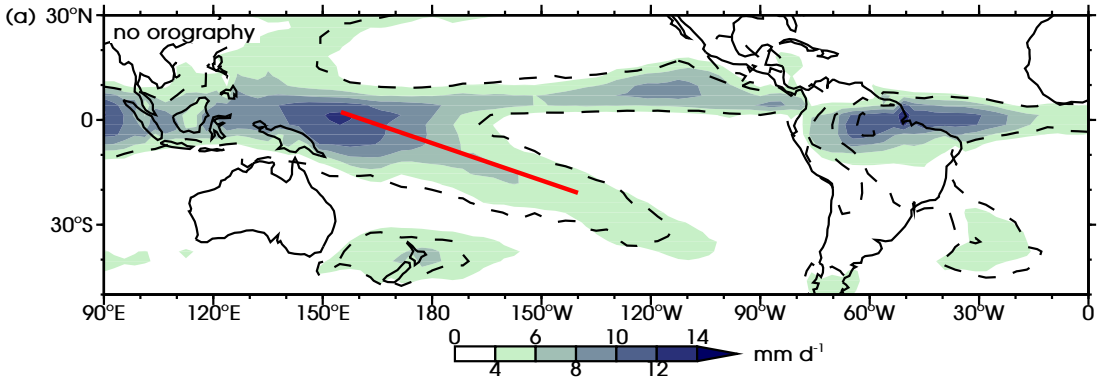

Figure 4.10: No-orography experiment. Time mean precipitation rate (November to April, shaded colours, mm d^{-1}). The thick diagonal red line shows the computed SPCZ mean precipitation axis location, the black dashed line shows the 4 mm d^{-1} contour of the IGCM4 control integration (as in figure 4.1b).

rate along the mean precipitation axis is 7.27 mm d^{-1}, only slightly lower than in the control experiment. The southeastern limit of the SPCZ extends about 10° further eastward. These minimal changes indicate that the direct influence of orography on the SPCZ through changes to the atmosphere is small.

This result agrees with comparable model experiments by Takahashi & Battisti (2007a,b) and Widlansky *et al.* (2011). The Takahashi & Battisti (2007a,b) experiment was designed by adding complexity to an aqua planet rather than decreasing complexity from the full model as has been done here. Their results indicate that the South American continent and the Andes mountain range have a very small influence on the Pacific precipitation pattern. However, if atmosphere-ocean feedbacks are included in this experiment (through an interactive mixed layer or a coupled ocean model) southern Pacific precipitation does change (Kitoh, 2002; Takahashi & Battisti, 2007a,b).

Outside the SPCZ region, precipitation is now mostly focused within the zonal ITCZ. The SACZ disappears, in favour of a zonal ITCZ from the Amazon extending into the Atlantic. Furthermore, the directly orographically forced precipitation west of the Andes and over New Guinea disappears in the experiment. The detailed mechanism for the changes in the SACZ region is beyond the scope of the study presented in this chapter.

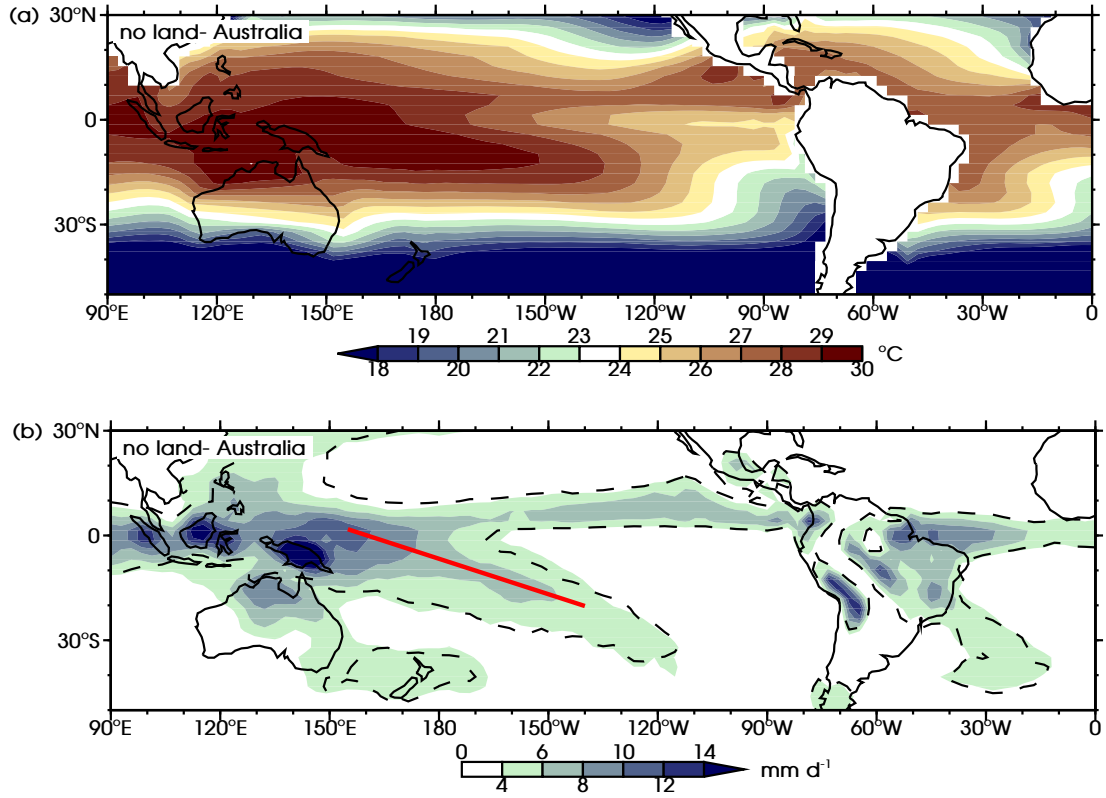

Figure 4.11: No-land experiment, no Australia integration. (a) Time mean SST forcing (November to April, shaded colours, °C) and (b) precipitation rate (shaded colours, mm d^{-1}). The thick diagonal red line in (b) shows the computed SPCZ mean precipitation axis location, the black dashed line in (b) shows the 4 mm d^{-1} contour of the IGCM4 control integration (as in figure 4.1b).

4.4.4 NO LAND

Over the removed continents in the no-land experiments the surface forcing has changed. In the no-land Australia integration, the temperatures over Australia decrease southwards from 29°C to 20°C and the interpolated temperature contours are oriented west-to-east (figure 4.11a). In the no-land South America integration, the interpolated SST contours are oriented in a northwest-southeast direction, due to the upwelling of cold water in the eastern Pacific compared to relative warm water at the same latitudes in the western Atlantic (figure 4.12a). These SST patterns have not been designed to be a 'realistic' representation of the SSTs in the case that the continents were actually not there. Instead, the experiments have been designed to test the influence of continental heating from land surfaces on the SPCZ, whilst keeping any other forcing equal (including SSTs over the oceans).

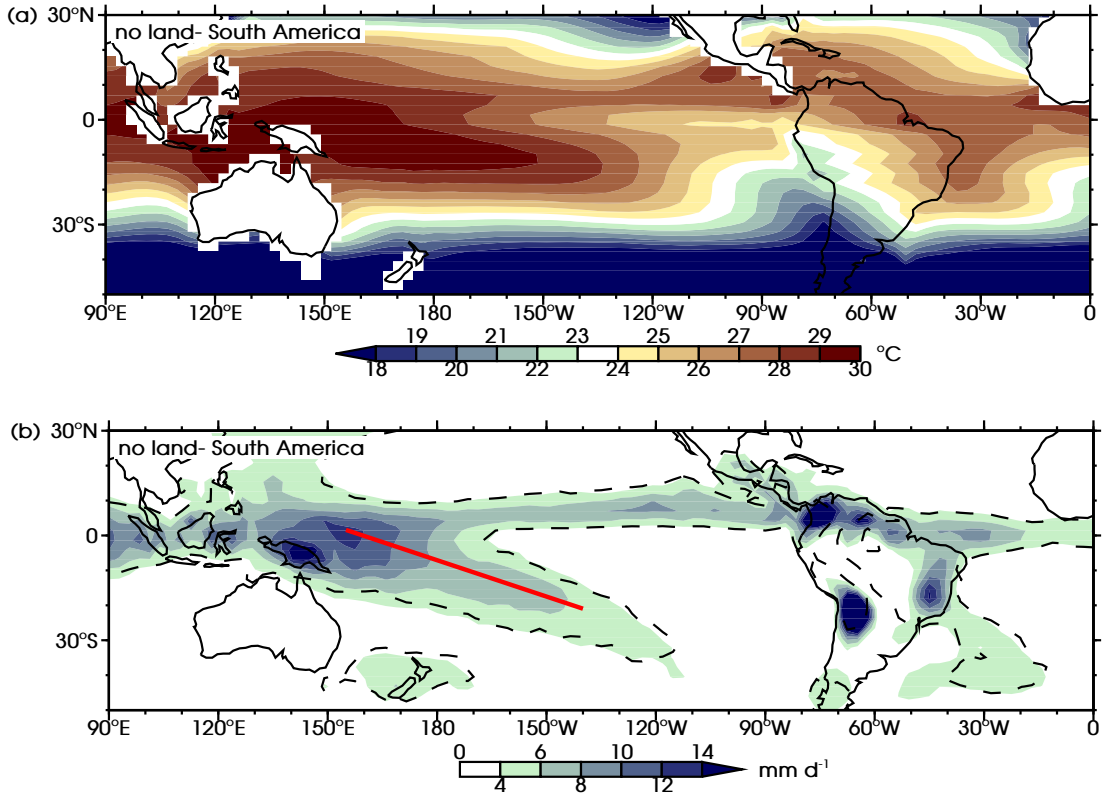

Figure 4.12: As figure 4.11, but now for the no South America integration.

Without continental heating over Australia, New Zealand, and the maritime continent, the SPCZ remains in place (figure 4.11b). The new slope is $-0.34°\text{N}/°\text{E}$, slightly less diagonal than in the control integration. Within the SPCZ margin the precipitation rate has somewhat decreased, giving a slightly weaker SPCZ strength ($7.03\ \text{mm d}^{-1}$). Precipitation over Australia and the maritime continent has increased. This is likely to be caused by the increased near-surface water vapour pressure when land surface is changed to sea surface in the model and the fact that these relatively humid surfaces are not at sea level.

Similarly the influence of South American continental heating on the SPCZ seems to be small, the change in SPCZ orientation and strength is minimal (figure 4.12b). The slope of the SPCZ in the experiment is $-0.35°\text{N}/°\text{E}$, its strength $7.83\ \text{mm d}^{-1}$. As was found in the no-Australia integration, the largest precipitation changes appear over the removed continent of South America.

To test the influence of the aqua mountains, an additional integration was performed in which all continents and all orography were removed (not shown). The results were not significantly different from the no-land integrations presented

here. Kiladis *et al.* (1989) performed equivalent experiments in an AGCM. Despite having prescribed a different SST forcing over the removed continents and changing SST patterns in open ocean, their results match the current no-land South America experiment. The location of the simulated SPCZ in their model is biased towards Australia, consequently removing continental heating there has a more significant effect.

4.5 DISCUSSION

Experiments have been conducted using IGCM4 to test the influence of surface boundary conditions on the SPCZ. Experiments included zonal SST asymmetries, absolute SST values, global orography and continental configuration (the presence of Australia and South America). The quality of the simulated SPCZ in the IGCM4 control run is within the range of 23 CMIP5 AMIP experiments. SPCZ slope and strength from all experiments are plotted in figure 4.13, together with the control integration, observational data and 23 CMIP5 coupled model historical experiments. The figure shows the SPCZ is a very robust climatological feature. Removing orography or removing the Australian or South American continents has very little influence; the experimental SPCZ is almost identical to the SPCZ in the control integration in these cases.

Zonal SST asymmetries impact both SPCZ strength and slope. Stronger asymmetries lead to a stronger SPCZ (+4.5 mm d^{-1} for $\alpha = 2$). La Niña events are comparable to these experiments and the experimental results agree with the observed stronger SPCZ during such events (e.g. Folland *et al.*, 2002; Juillet-Leclerc *et al.*, 2006). Decreasing SST asymmetries towards zonally symmetric values impacts the SPCZ slope. The modelled diagonal SPCZ collapses when the asymmetry is half as strong as observed values ($\alpha = 0.5$), instead there is a wide band of precipitation over the equator. Such a collapse of the SPCZ to a zonal band of precipitation has been observed during extreme El Niño events (e.g. Vincent *et al.*, 2011; Cai *et al.*, 2012). The upper-tropospheric dynamical forcing does not change in these integrations; it is atmospheric thermodynamics that makes the difference. The subtropical high, west of the Andes provides moisture to the SPCZ (figure 4.14a). With decreasing zonal SST asymmetry this moisture transport slows down and despite dynamical forcing,

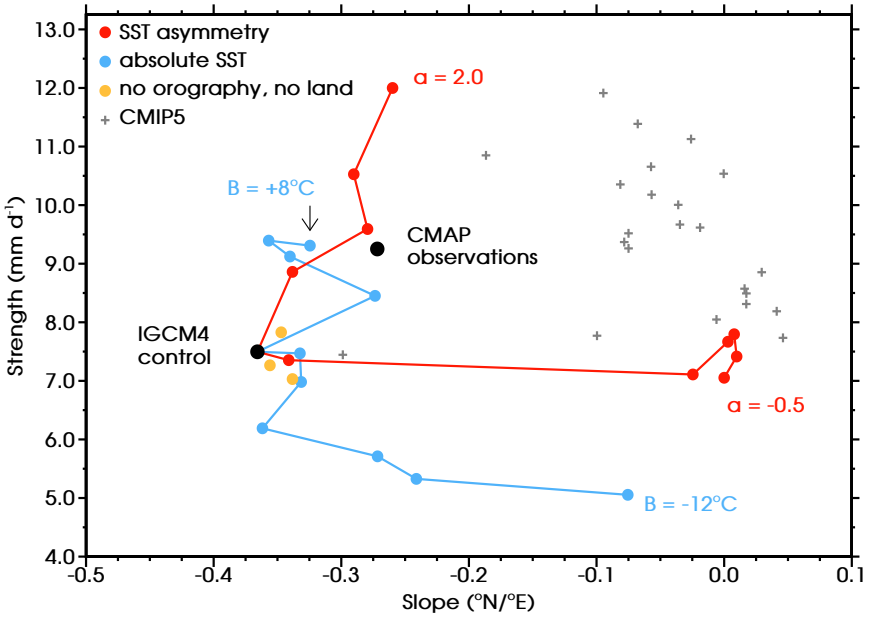

Figure 4.13: Time mean SPCZ strength (November to April, mm d^{-1}) plotted against SPCZ slope (°N/°E). Black dots are the CMAP observations and the IGCM4 control integration. Experiments: no orography and no land (orange), SST asymmetry (red), absolute SST (blue), CMIP5 historical experiments (grey).

convection is not triggered (figure 4.14b). Similar lower-tropospheric moisture convergence anomalies have been observed during extreme El Niño events (Vincent *et al.*, 2011).

The absolute SST experiments show that SST values impact the SPCZ strength. For increasing SSTs the SPCZ holds its diagonal orientation whilst the precipitation rate increases by +1.9 mm d^{-1} for the β = +8°C integration. Vertical profiles of temperature and humidity indicate that computed convection reaches higher and produces more precipitation. Decreasing SSTs has the opposite effect. For extremely cold cases the SPCZ loses its diagonal orientation; values of CAPE over the South Pacific are too low for deep convection and strongest precipitation is found over the area with highest CAPE, parallel to the SST contours. These extremely cold integrations are in agreement with model experiments of the Last Glacial Maximum (21 ky BP, CO_2 180 ppm, northern ice sheet) in which the SPCZ is shifted northwards (Saint-Lu *et al.*, 2015).

From the ensemble of IGCM4 experiments it can therefore be concluded that there are prerequisite conditions that need to be met to create a diagonal SPCZ. Asymmetries in the SST pattern are shown to be vital. Though not considered in the

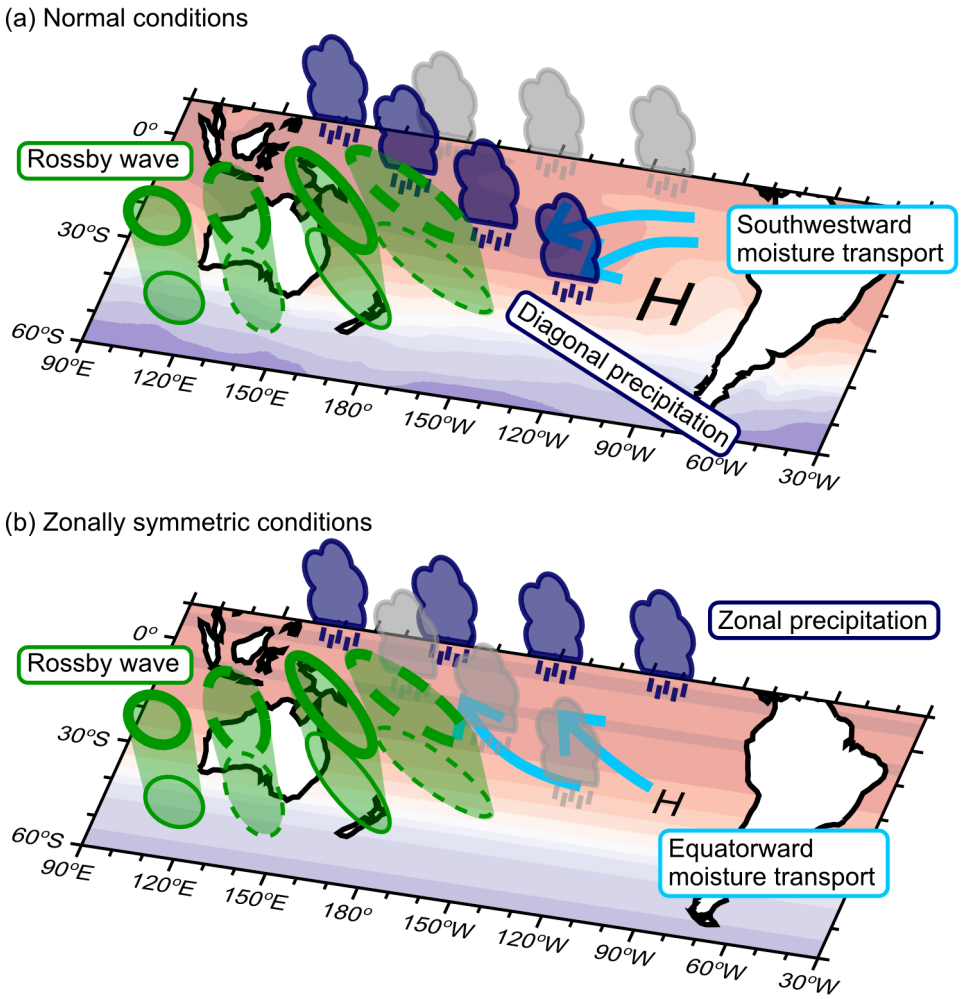

Figure 4.14: (a) Schematic of the conditions and mechanism of a diagonal SPCZ. An asymmetrical SST distribution generates a subtropical anticyclone over the southeast Pacific, on its western flank this area transports moisture southwestward into the SPCZ region. Dynamical forcing from equatorward propagating Rossby waves then triggers convection in a northwest-southeast oriented band, parallel to an area of reduced static stability ahead of a cyclonic vorticity anomaly. (b) As (a) but for zonally symmetric SST conditions. The subtropical anticyclone weakens and moisture transport is equatorward. Despite similar diagonally oriented dynamical forcing, precipitation forms in a zonal band along the equator.

current experiments, air-sea interactions and ocean basin boundaries are, ultimately, responsible for these asymmetries (Seager & Murtugudde, 1997). The high pressure area that consequently forms over the subtropical eastern Pacific transports warm, moist air from the equator to the SPCZ region. Then, when the dynamical forcing is right, deep convection produces precipitation over the SPCZ (figure 4.14a).

Coral isotope based studies of the SPCZ in past climates so far focus mainly on the eigtheenth-century onwards (Bagnato *et al.*, 2005; Juillet-Leclerc *et al.*, 2006). These studies give valuable information of climatic variations in the SPCZ and provide additional information to verify output from climate models for different climate basic states. However, to make reliable statements on SST distributions and the SPCZ further back in time, a more dense network of isotope cores is needed. If such data were available, an interesting question following the current study would be, whether the onset of the SPCZ coincides with the onset of zonal SST gradients about 1-2 Myr ago (McClymont & Rosell-Mele, 2005; Brierley & Fedorov, 2010).

Twenty-first-century projections of SPCZ precipitation are uncertain in the CMIP5 ensemble, however SST projections are consistent and show an equatorial warming and reduced zonal and meridional gradients (J R Brown *et al.*, 2013; Widlansky *et al.*, 2013). Based on the physical mechanisms presented here and the CMIP5 SST projections, the future of the SPCZ depends on the relative strength of two competing effects. Increasing absolute SST values force stronger SPCZ precipitation, while decreased zonal SST gradients force weaker SPCZ precipitation; this uneasy balance agrees with model experiments by Widlansky *et al.* (2013).

5

CONCLUSIONS

The aim of this thesis is to investigate the diagonal, northwest-southeast, orientation of the South Pacific and South Atlantic Convergence Zones (SPCZ and SACZ, respectively); in particular, to understand the interaction of dynamic and thermodynamic processes and how these induce and maintain the diagonal orientation and determine the strength of precipitation rates within the SPCZ and SACZ. The key results of the three preceding chapters are discussed in this chapter, together with a discussion of how these results help to progress the scientific understanding of diagonal convergence zones.

5.1 MECHANISMS FOR THE EXISTENCE OF DIAGONAL SOUTHERN HEMISPHERE CONVERGENCE ZONES

Theoretical frameworks have been presented in which the mechanisms that result in a diagonally oriented SPCZ are considered. The processes, interactions and feedbacks in these frameworks act on different time scales and together result in the climatological mean SPCZ that is observed over the South Pacific Ocean. On short, synoptic time scales the chain of events discussed in chapter 2 explains the development of individual, diagonally oriented, precipitation events. This mechanism for the development of precipitation in the SPCZ was found in

observational-based data and in output from the Intermediate General Circulation Model version 4 (IGCM4). The proposed mechanisms are however dependent on the given climatological atmospheric mean state; in chapter 4 the processes that give rise to this mean state are discussed.

The zonally asymmetric distribution of Sea Surface Temperatures (SSTs) forces an atmospheric mean state in which diagonal convergence zones can develop. Two aspects of the mean state have been identified to directly impact the formation of a diagonal SPCZ. First, the shape of the upper-tropospheric mean flow, with a subtropical jet and equatorial westerlies, the 'westerly duct', steers Rossby waves originating in this jet equatorwards. Wind shear on the northern edge of the jet and simple advection evolve originally circular vorticity centres in these waves, into diagonal, northwest-southeast, elongated shapes. Barotropic Rossby wave dynamics then describe the equatorward propagation well.

The second key aspect of the mean state is the southwestward flow that is found on the western flank of the east Pacific subtropical high. This flow provides a continuous supply of moisture to the SPCZ. Ahead of diagonally oriented cyclonic vorticity centres in the Rossby wave, poleward flow ascends and triggers convection in a band parallel to the vorticity centre. The climatological SPCZ is then the sum of many of such precipitation events. In the absence of the mean moisture transport towards the SPCZ region, e.g. when the zonal SST asymmetry is reduced, the dynamical Rossby wave forcing does not lead to a significant thermodynamic response and the SPCZ disappears in favour of a zonal precipitation band close to the equator.

Latent heat release from condensation in deep convection results in more ascent and more upper-tropospheric divergence. Through vortex stretching, the associated anticyclonic tendency spins down the cyclone that triggered deep convection. This negative feedback has been shown to dissipate the Rossby wave in situ, stopping further Rossby wave propagation. The sequence of events discussed here can be found in observational-based data and in IGCM4. The results from the perturbation experiment in chapter 3 confirm the causal relation between Rossby wave initiated deep convection and dissipation of the same Rossby wave.

Convection events in the SPCZ directly impact Rossby wave propagation in the region; equatorward propagating Rossby waves dissipate in the SPCZ. These

Rossby waves normally transport eastward momentum from the extratropics towards equatorial regions (Kiladis, 1998). This momentum transport is cancelled and subsequently the upper-tropospheric westerly flow over the equatorial eastern Pacific is reduced in strength. As discussed earlier, these westerlies are a key aspect of the mean flow that promotes the diagonal SPCZ. The impact of the SPCZ on the Pacific mean flow is likely to be a negative feedback in the local climate system.

Though most of the work in this thesis is focussed on the SPCZ, the same interaction between Rossby waves and parallel bands of deep convective precipitation is also valid in the SACZ (chapter 2). There is however a crucial difference, the negative feedback based on vortex stretching that prevents continued wave propagation in the SPCZ is not strong enough to dissipate the Rossby wave in the SACZ region. These findings provide a step forwards in the understanding of the mechanisms for the existence of the SPCZ and SACZ.

5.2 LIMITATIONS, IMPLICATIONS AND FURTHER WORK

IGCM4 is an Atmospheric General Circulation Model (AGCM), the experiments presented here therefore do not include interactions between atmosphere and ocean. Given the importance of the distribution of SSTs in setting the diagonal orientation of the SPCZ, this is an important limitation to the study. In the actual climate and in a coupled model, SSTs are the result of heat exchange between ocean and atmosphere, ocean circulation and vertical ocean mixing. An obvious extension to chapter 4 would therefore be to repeat the 'no orography' and 'no land' experiments in a coupled model. This is however not as simple as suggested, as the simulated SPCZ in coupled models is biased to be overly zonal (J R Brown *et al.*, 2013; Niznik *et al.*, 2015). The approach of chapter 4, to break down the SPCZ mechanism, will therefore need adjustment as well.

Furthermore, the AGCM used in this study is one of intermediate complexity. Though its ability to simulate a diagonal SPCZ is within the spread of AGCM models in the Coupled Model Intercomparison Project phase 5 (CMIP5), the parametrisation scheme for convection is basic and depends on local atmospheric stability alone. Model developments and increased computational power now allow for convection permitting models, i.e. models in which convection is explicitly represented and

not parametrised. The impact of such models on the simulation of the SPCZ is still unknown. For large-scale extratropical systems with well-resolved dynamical ascent forcing convection, convectively parametrised models perform well. However, the self-organised convection at the tropical end of the SPCZ is not represented well by parametrisation.

Despite the limitations of IGCM4, the new presented results contribute to the understanding of the formation of diagonal SPCZ and SACZ. Only the present-day climate, in El Niño-Southern Oscillation (ENSO) neutral state has been taken in to account. The results are however of interest to the study of both interannual variability and climate projections of the SPCZ. One way of using the new results is to take them in to account when formulating new research questions and methods. For example, for the study of the SPCZ in a future warmer climate, chapter 4 shows it is very important to have an unbiased SST field to force the atmosphere. The generally biased coupled models in the CMIP5 ensemble might therefore not be the best tools for such studies, as also suggested by J N Brown *et al.* (2013) and Widlansky *et al.* (2013). Instead flux-corrected coupled ocean-atmosphere models, with reduced SST biases, could be used.

Another way in which the new results can be used, is by taking the presented mechanisms and applying them to a different atmospheric mean state, e.g. a warmer future climate. Based on projected SST changes, the change to lower-tropospheric moisture transport, Rossby wave propagation and the related change to SPCZ strength and orientation can then be predicted. Some confidence for such an approach can be gained by applying this method to known changes in the mean state. For an ENSO positive climatic mean state (El Niño), the experiments from chapter 4 suggest a decreased diagonal orientation for the SPCZ, which is in agreement with observed changes (Vincent *et al.*, 2011; Haffke & Magnusdottir, 2013; Murphy *et al.*, 2014).

Finally, the current work also leads to further research questions for possible future study. In chapter 2 a Rossby wave mechanism is proposed that explains how Rossby waves trigger convection in a diagonal band along the SPCZ and SACZ. Possible further experiments could include a test to investigate what the SPCZ or SACZ would look like when Rossby waves are eliminated. Such an experiment could be designed in different ways, for example by using a regional AGCM with

modified boundary conditions, simulations in which the meridional gradient of planetary vorticity is removed outside the tropics or by nudging the extratropics to a climatological mean state. This test would identify whether the Rossby wave mechanism is a proximate or ultimate cause of convection along the SPCZ or SACZ.

Furthermore, in chapter 2 it is shown that the SPCZ and SACZ are formed by the same mechanism based on equatorward Rossby wave propagation. One could investigate if the development of the South Indian Convergence Zone, not considered in this thesis, can also be explained by this mechanism and whether it is much weaker than the SPCZ and SACZ because there is no upper-tropospheric westerly duct over the Indian Ocean. Another question, also based on the mechanism presented in chapter 2, is what processes set the longitude at which Rossby waves from the subtropical jet start propagating equatorward. Is this longitude, as suggested by Widlansky *et al.* (2011), related to the location of the jet exit and decreasing zonal wind speeds?

In chapter 4 moisture transport from the tropics towards the SPCZ region is identified as an important aspect of the atmospheric basic state to support a diagonal SPCZ. An experiment in which the lower-tropospheric moisture levels are controlled, without other changes to the basic state could increase understanding of this mechanism. Would the SPCZ remain in position in a world with a zonally asymmetric SST distribution but with low levels of atmospheric moisture?

The model results from the experiments in chapter 4 show that the processes for a diagonal SACZ are more complicated than those that set the diagonal SPCZ. Besides SSTs, also orography and land-sea contrasts influence the SACZ. A more detailed investigation, maybe with a more complex AGCM, would increase the understanding of the SACZ. A final suggestion would be to investigate the links between SPCZ and ITCZ and between SPCZ and SACZ. The SST asymmetry experiments in chapter 4 suggest that the increasing precipitation rates in the SPCZ are linked to decreasing precipitation in the ITCZ, although a mechanism for this link has not been suggested. In IGCM4 no link between SPCZ and SACZ convection was found, though the existence of such a link was suggested by Grimm & Silva Dias (1995). Further study is needed, maybe with a focus on the area where Rossby waves are dissipiated due to the SPCZ and where Rossby waves forcing SACZ convection originate.

5.3 SUMMARY OF THE THESIS

This thesis considers the mechanisms responsible for the northwest-southeast, diagonal, orientation of the SPCZ and SACZ. Various interactions between large-scale dynamic and local thermodynamic processes and interactions between tropical and extratropical regions have been investigated. Zonal asymmetries in the distribution of SSTs give rise to an atmospheric mean state which is conducive to the formation of a diagonally oriented SPCZ. Key features of this mean state are the shape of the upper-tropospheric flow and southwestward moisture transport on the western flank of the subtropical high. In this mean state, equatorward propagating Rossby waves trigger diagonally oriented bands of deep convective precipitation in both the SPCZ and SACZ. Two negative feedback mechanisms have been identified. First, the dissipation of Rossby waves due to latent heat release from convection caused by these Rossby waves. Second, the impact of convection in the SPCZ on the strength of upper-tropospheric westerlies in the eastern equatorial Pacific. These show there is a two-way interaction between the atmospheric mean state and the diagonal SPCZ and SACZ.

A

OVERVIEW OF CMIP5 MODELS

Table A.1 gives an overview of the 23 models in the Coupled Model Intercomparison Project phase 5 (CMIP5) that are referred to in the thesis[1]. Output from two CMIP5 baseline simulations have been used: 'historical' and 'AMIP'. In the 'historical' experiment the models are integrated in their coupled form, i.e. atmosphere and ocean. To allow for verification of the model output against the observational record, atmospheric composition (including CO_2 concentration and natural and anthropogenic aerosols), solar forcing and land use changes are imposed. 'AMIP' stands for Atmospheric Model Intercomparison Project; the atmospheric model is integrated without a coupled ocean model. Sea surface temperatures and sea ice concentrations are prescribed from observational data. Changing atmospheric composition, solar forcing and land use are prescribed as in the 'historical' experiment.

Figure A.1 shows maps for the individual models for November to April mean precipitation rates in the 'AMIP' experiment, Figure A.2 the equivalent in the 'historical' experiment. Time means have been computed over the years 1979–2005.

[1] I acknowledge the World Climate Research Programme's Working Group on Coupled Modelling, which is responsible for CMIP, and I thank the climate modeling groups (listed in Table A.1) for producing and making available their model output. For CMIP the US Department of Energy's Program for Climate Model Diagnosis and Intercomparison provides coordinating support and led development of software infrastructure in partnership with the Global Organization for Earth System Science Portals.

Table A.1: Overview of CMIP5 models included in study.

Model name	Year	Institution	Main reference(s)
ACCESS1.0	2011	Commonwealth Scientific and Industrial Research Organization (CSIRO) and Bureau of Meteorology (BOM)	Bi *et al.* (2013), Dix *et al.* (2013)
ACCESS1.3	2011	CSIRO and BOM	Bi *et al.* (2013), Dix *et al.* (2013)
BCC-CSM1.1	2011	Beijing Climate Center, China Meteorological Administration	Wu (2012), Xin *et al.* (2012), Xin *et al.* (2013)
BCC-CSM1.1(m)	2011	Beijing Climate Center, China Meteorological Administration	Wu (2012), Xin *et al.* (2012), Xin *et al.* (2013)
BNU-ESM	2011	Beijing Normal University	Ji *et al.* (2014)
CanAM4	2010	Canadian Center for Climate Modelling and Analysis	Von Salzen *et al.* (2013)
CCSM4	2010	US National Centre for Atmospheric Research (NCAR)	Gent *et al.* (2011)
CESM1-CAM5	2010	US National Science Foundation - Department of Energy (DOE) - NCAR	Hurrell *et al.* (2013)
CMCC-CM	2009	Centro Euro-Mediterraneo per I Cambiamenti Climatici	Fogli *et al.* (2009)
CNRM-CM5	2010	Centre National de Recherches Meteorologiques and Centre Europeen de Recherche et Formation Avancees en Calcul Scientifique	Voldoire *et al.* (2013)
CSIRO-Mk3-6-0	2009	Queensland Climate Change Centre of Excellence and CSIRO	Rotstayn *et al.* (2012)
FGOALS-g2	2011	Institute of Atmospheric Physics - Tsinghua University	Li *et al.* (2013)
GFDL-CM3	2011	National Oceanic and Atmospheric Administration (NOAA) Geophysical Fluid Dynamics Laboratory	Delworth *et al.* (2006), Donner *et al.* (2011)
GISS-E2-R	2011	National Aeronautics and Space Administration Goddard Institute for Space Studies USA	Schmidt *et al.* (2006)
HadGEM2-AO	2009	UK Met Office Hadley Centre	Collins *et al.* (2011), Martin *et al.* (2011)

Table A.1: Overview of CMIP5 models included in study (continued).

Model name	Year	Institution	Main reference(s)
IPSL-CM5A-LR	2010	Institut Pierre Simon Laplace	Dufresne *et al.* (2013)
IPSL-CM5A-MR	2009	Institut Pierre Simon Laplace	Dufresne *et al.* (2013)
IPSL-CM5B-LR	2010	Institut Pierre Simon Laplace	Dufresne *et al.* (2013)
MIROC5	2010	University of Tokyo, National Institute for Environmental Studies and Japan Agency for Marine-Earth Science and Technology	Watanabe *et al.* (2010)
MPI-ESM-LR	2009	Max Planck Institute for Meteorology	Giorgetta *et al.* (2013)
MPI-ESM-MR	2009	Max Planck Institute for Meteorology	Giorgetta *et al.* (2013)
MRI-CGCM3	2011	Meteorological Research Institute	Yukimoto *et al.* (2011), Yukimoto *et al.* (2012)
NorESM1-M	2011	Norwegian Climate Centre	Iversen *et al.* (2013)

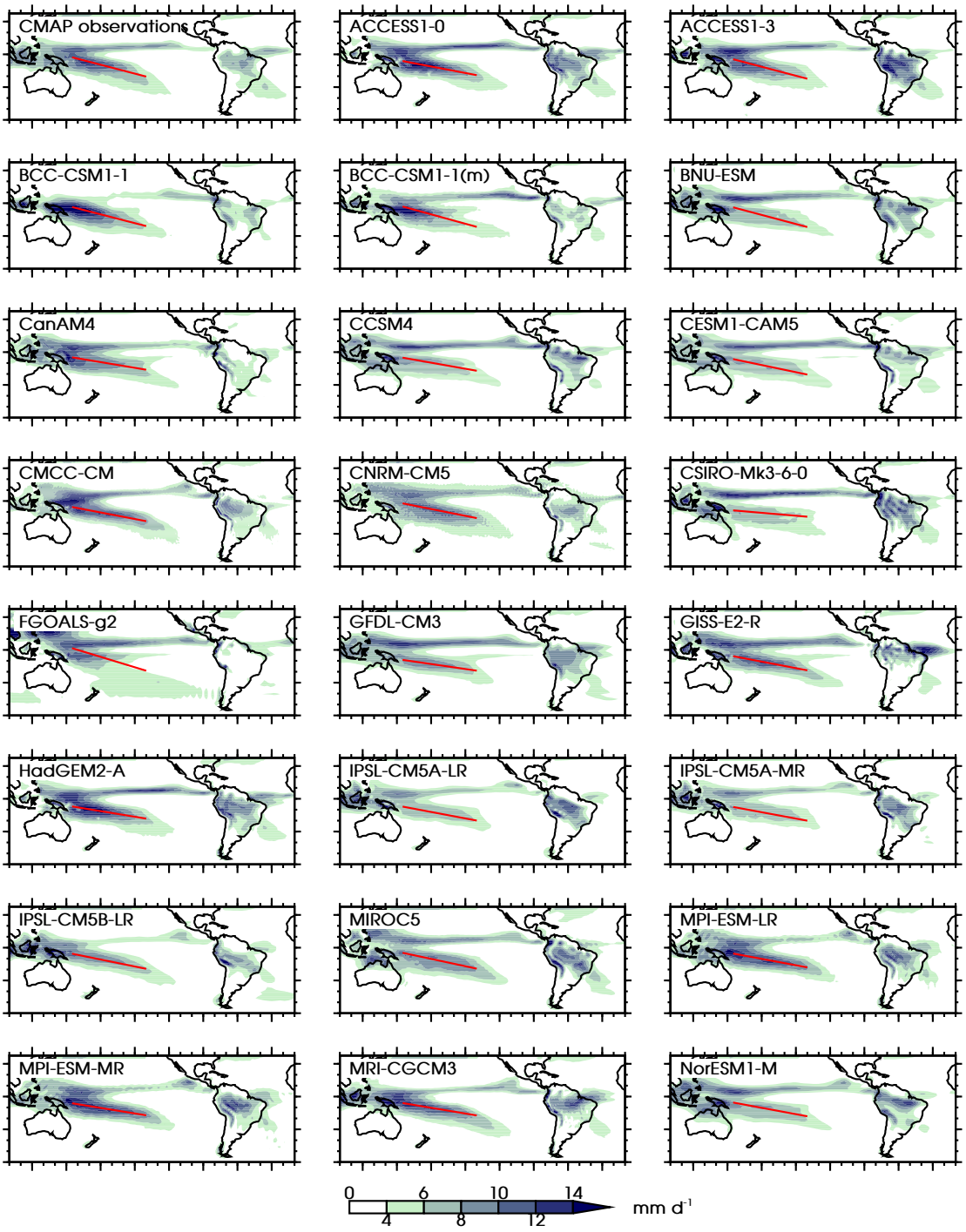

Figure A.1: Time mean precipitation rate (November to April) in CMAP (top left) and 23 models in the CMIP5 'AMIP' experiment in shaded colours (mm d^{-1}). Red diagonal lines indicate the mean SPCZ precipitation axis, computed as in section 4.2.

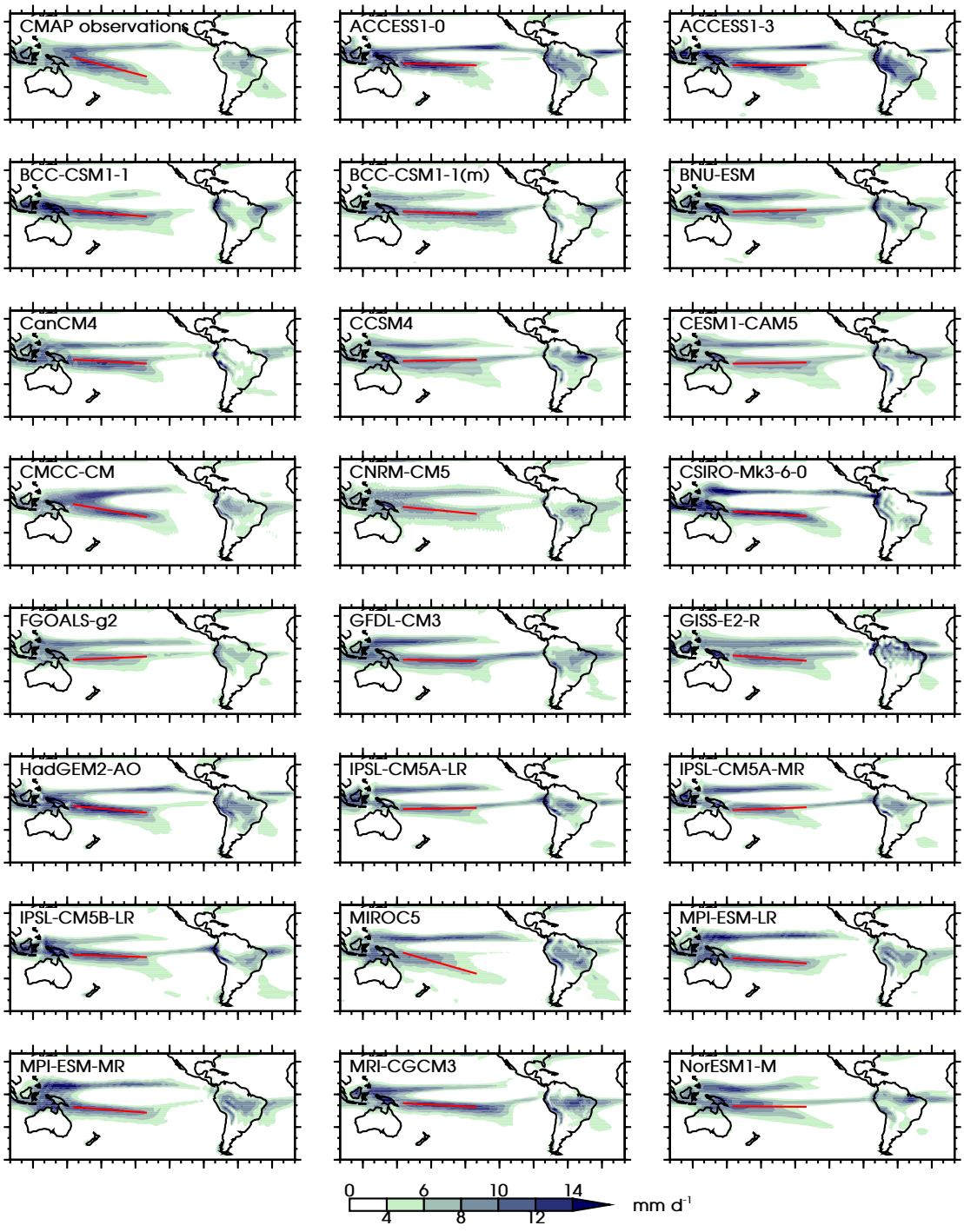

Figure A.2: As Figure A.1, but now for the CMIP5 'historical' experiment.

B

IGCM4 MODEL EVALUATION

This appendix is based on part of a paper that has been published in Geoscientific Model Development with the title 'IGCM4: A fast, parallel and flexible intermediate climate model' (Joshi *et al.*, 2015). K. van der Wiel was responsible for the analysis of the T42L20 model configuration, under supervision by M.M. Joshi, who provided scientific input.

In this appendix the model climatology of the Intermediate General Circulation Model version 4 (IGCM4) in its standard T42L20 configuration is presented (model description in section 3.2). The model was integrated for 60 years, from which the first 10 years were removed as spin-up. December, January, February (DJF) and June, July, August (JJA) seasonal means are compared to the relevent observational-based data product (described in section 2.2).

Seasonal mean surface temperatures for IGCM4 are compared to surface temperatures from the NCEP-DOE Reanalysis (Kanamitsu *et al.*, 2002, time mean over 1979-2013) in figure B.1. In IGCM4, during austral summer (DJF) there is a cold bias over Greenland, Alaska, northern Europe and Asia; tropical land surfaces and Antarctica show a warm bias. In austral winter (JJA) most land surfaces show a warm bias, except Antarctica which is colder than in the reanalysis. The absolute biases are mostly below 10°C. Biases over the oceans are very small, as Sea Surface Temperatures (SSTs) are prescribed rather than computed. Note that for the work

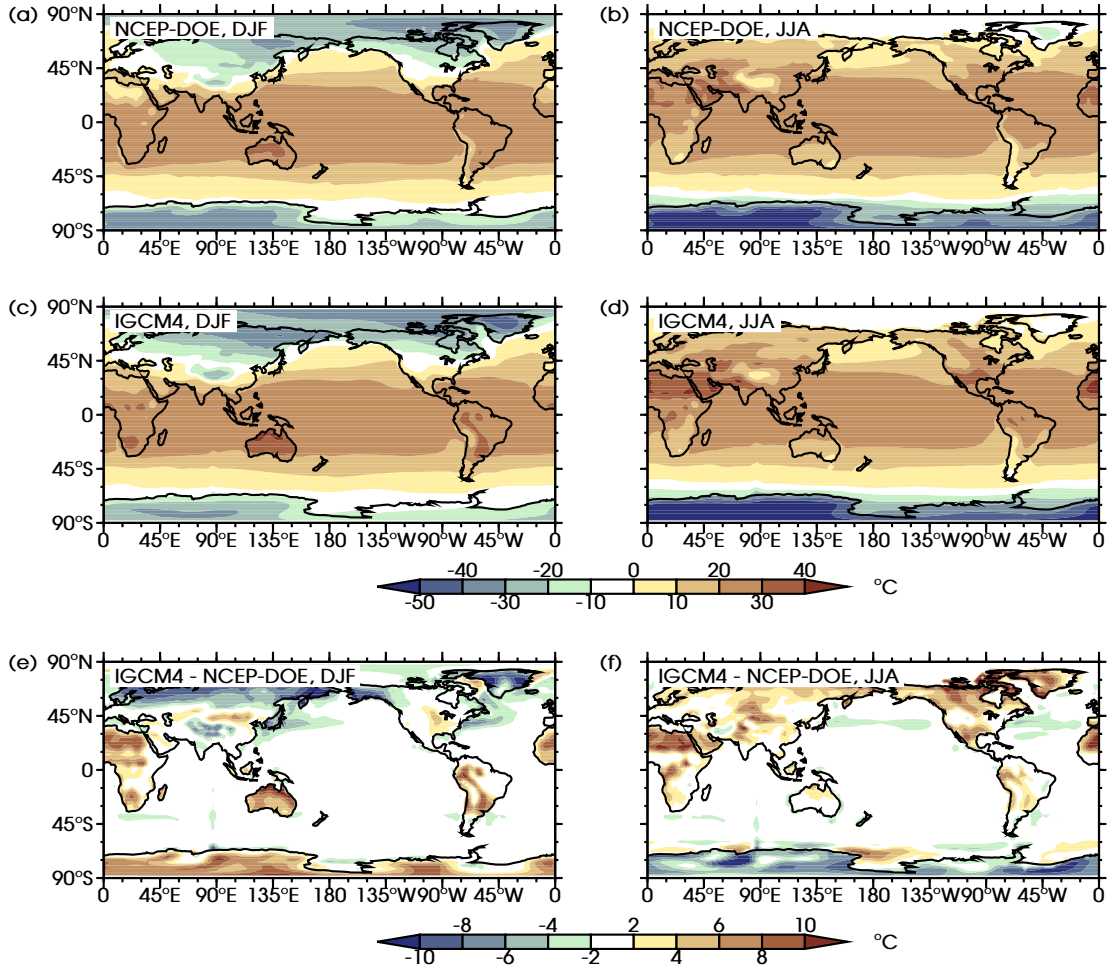

Figure B.1: Surface temperature (°C) in (a,b) NCEP-DOE reanalysis, (c,d) IGCM4 and (e,f) difference between IGCM4 and reanalysis. Left column shows December-February time mean, right column shows June-August time mean.

presented in chapters 3 and 4 the standard IGCM4 SST forcing, that is shown here, is replaced with one based on the NOAA Optimum Interpolation V2 dataset (Reynolds *et al.*, 2002).

During austral summer, the South Pacific Convergence Zone (SPCZ), South Atlantic Convergence Zone (SACZ) and Intertropical Convergence Zone (ITCZ) are represented quite well in IGCM4 (diagnosed by their 4 mm d^{-1} contour, Figure B.2b). The SPCZ is slightly weaker than observed, the ITCZ displaced northwards (Figure B.2c, observations from Climate Prediction Center Merged Analysis of Precipitation, CMAP, Xie & Arkin, 1997, time mean over 1979–2005). To compare IGCM4's performence with other Atmospheric General Circulation Models (AGCMs), data from the Coupled Model Intercomparison Project phase 5 (CMIP5)

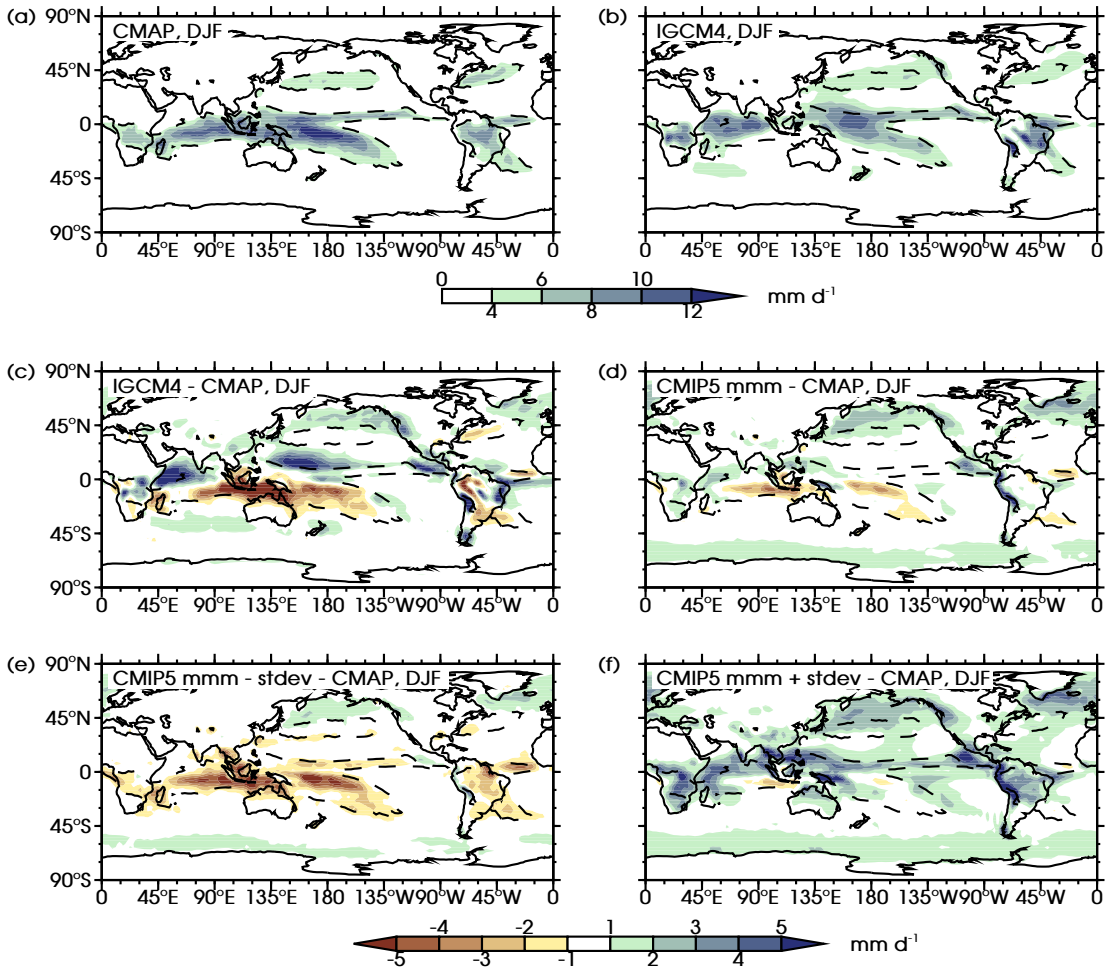

Figure B.2: Time mean precipitation rate (December-February, mm d^{-1}) in (a) CMAP, (b) IGCM4 and differences between (c) IGCM4 and CMAP, (d) CMIP5 multi model mean ensemble and CMAP, (e) as for (d) but for the multi model mean minus one standard deviation and (f) as for (e) but multi model mean plus one standard deviation. CMIP5 models as in appendix A. The dashed contour in all panels shows the 4 mm d^{-1} from CMAP.

atmosphere-only ('AMIP') experiment are analysed (appendix A). The multi model mean precipitation bias is smaller than IGCM4 (Figure B.2d). However when variability amongst individual models is taken into account (mean ± one standard deviation, figures B.2e and B.2f), IGCM4 is found within the model spread. For example, in the SPCZ, IGCM4 has a 2–5 mm d^{-1} dry bias, which is comparable to the CMIP5 multi model mean minus one standard deviation. The simulated precipitation distribution of state-of-the-art AGCMs is of a similar quality to IGCM4.

In austral winter IGCM4 shows larger precipitation biases, especially over the Indian Ocean, maritime continent and Caribbean region (figure B.3c). Such biases are however also found in the collection of models in CMIP5 (figure B.3e and B.3f).

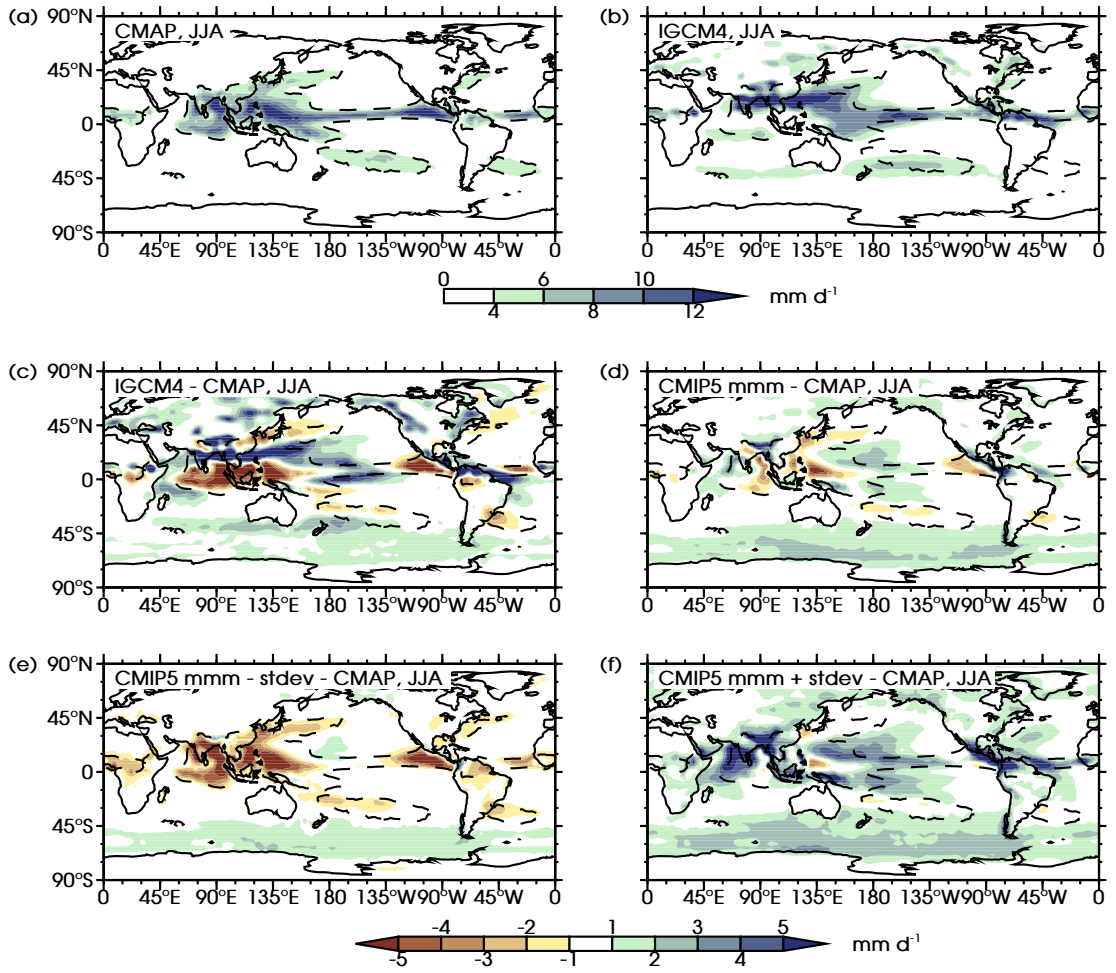

Figure B.3: As figure B.2, but now for June-August time mean.

For both seasons IGCM4 is within the quality range of more complex AGCMs in the CMIP5 archive, for the current study of the diagonal convergence zones it is therefore a suitable choice as an intermediate complexity climate model.

In figure B.4 simulated Outgoing Longwave Radiation (OLR) is compared to observations from the Interpolated OLR dataset (Liebmann & Smith, 1996, time mean over 1979–2011). In the tropics, where OLR is related to convective clouds and precipitation, the main features are represented well. There is a positive bias over the maritime continent during austral summer and over the Indian Ocean during austral winter, which both correspond to dry biases in the precipitation field.

The zonal mean zonal wind shows good agreement between IGCM4 and the NCEP-DOE reanalysis (time mean over 1979–2011). During austral summer, the southern subtropical jet is displaced about 10° equatorwards, in austral winter its poleward edge is about 10 m s^{-1} weaker than observed. The differences between

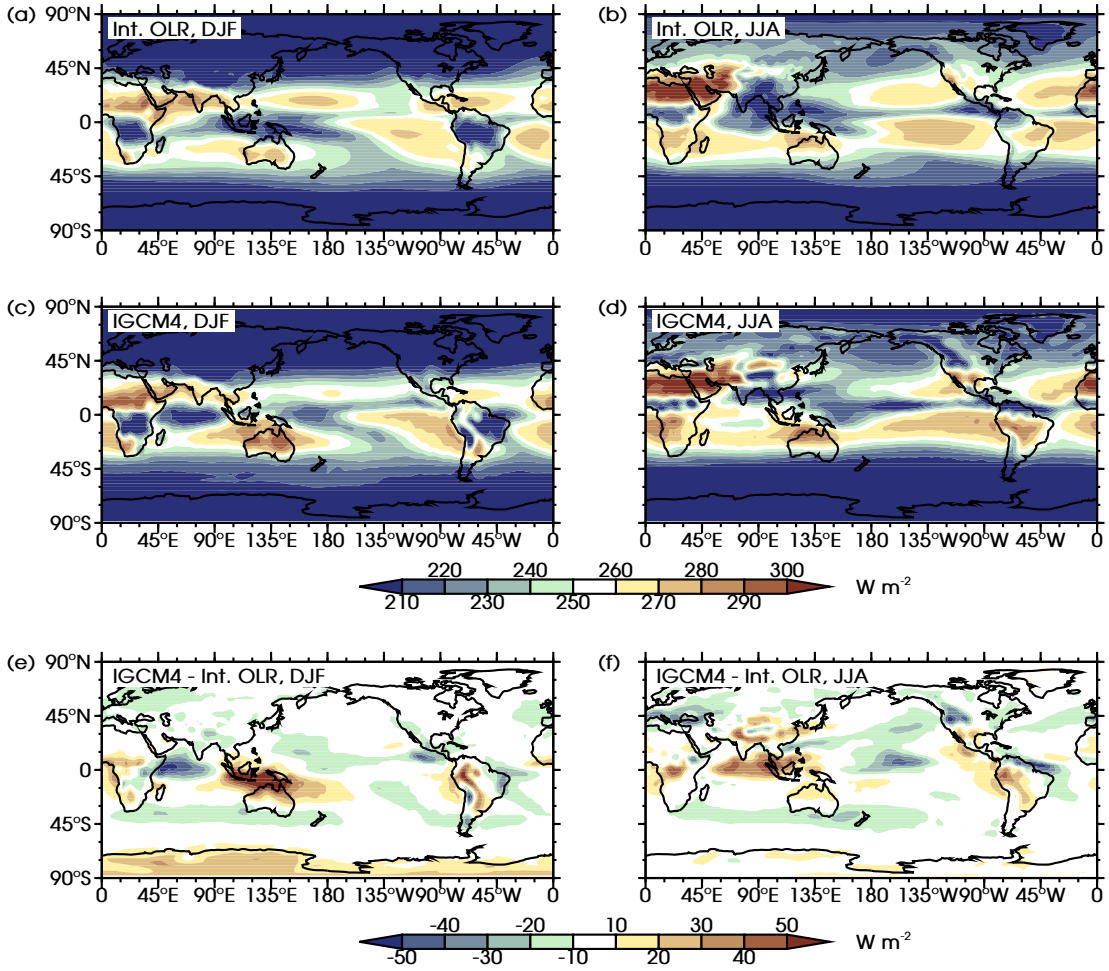

Figure B.4: As figure B.1, but now for OLR (W m^{-2}). Observational data from Interpolated OLR.

IGCM4 and reanalysis are smaller in the northern hemisphere subtropical jet.

Departures from the DJF zonal mean field are shown in figure B.6. The 200 hPa northern hemisphere standing wave pattern is found in both models, IGCM4 reproduces the eddy field of NCEP-DOE (time mean over 1979-2013). The low-pressure anomalies are weaker in IGCM4 (150 m height difference over northeast Asia), the high-pressure anomaly over the Atlantic Ocean is slightly weaker as well (50 m).

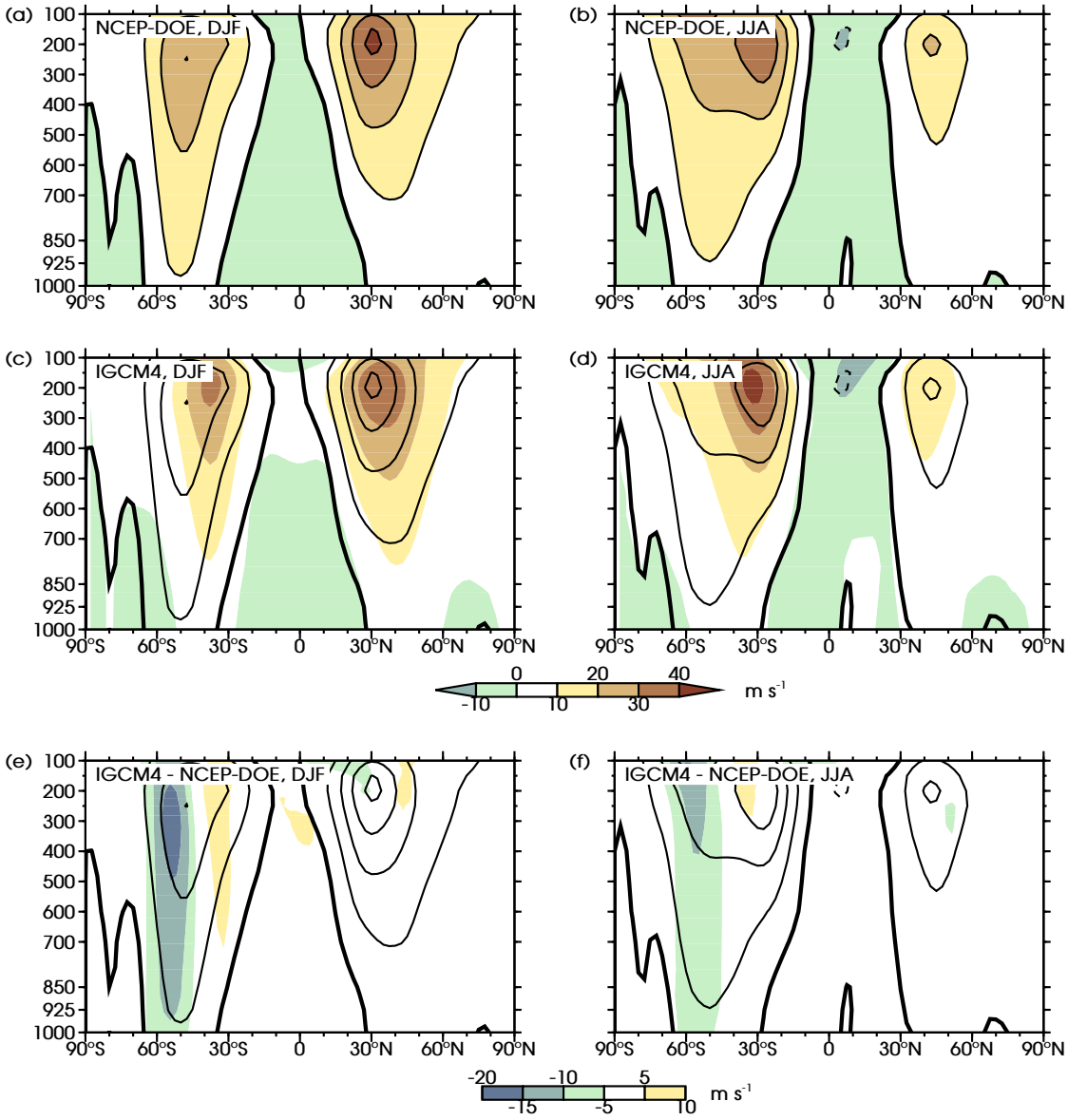

Figure B.5: As figure B.1, but now for zonal mean zonal wind (m s^{-1}). Observational data from NCEP-DOE. The contours in all panels show data from NCEP-DOE (contour interval 10 m s^{-1}, negative contours dashed, zero contour thicker).

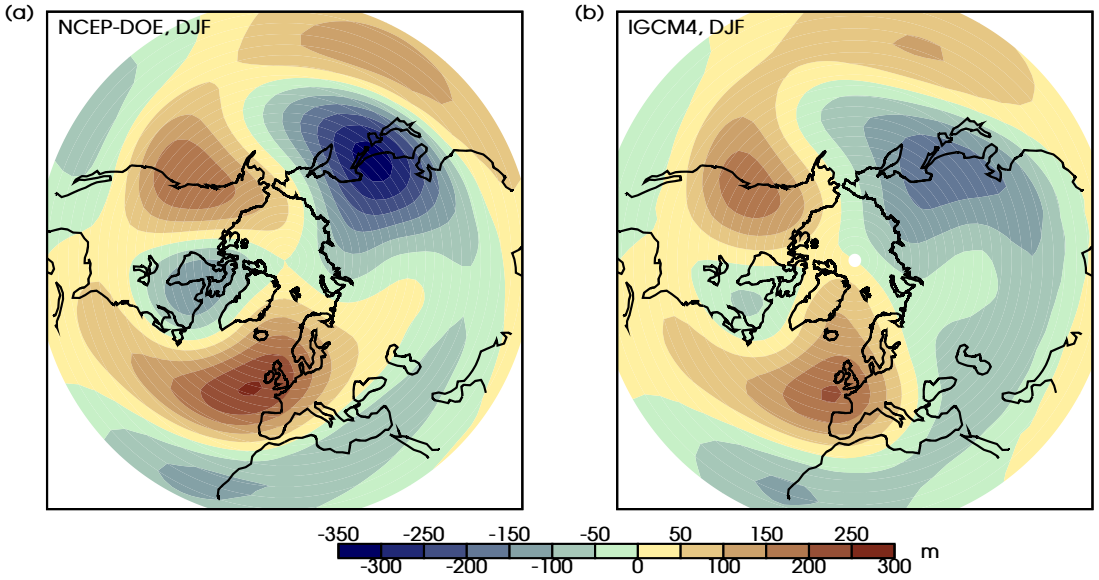

Figure B.6: Time mean geopotential height (m) eddy fields at 200 hPa (December-February) in (a) NCEP-DOE reanalysis and (b) IGCM4.

REFERENCES

Ambrizzi, T, Hoskins, B J, & Hsu, H-H. 1995. Rossby wave propagation and teleconnection patterns in the austral winter. *Journal of the Atmospheric Sciences*, **52**, 3661 – 3672.

Anderson, R K, Farr, G R, Ashman, J P, Smith, A H, & Ritter, L F. 1974. *Application of meteorological satellite data in analysis and forecasting*. Tech. rept. DTIC Document.

Arkin, P A, & Meisner, B N. 1987. The relationship between large-scale convective rainfall and cold cloud over the western hemisphere during 1982-84. *Monthly Weather Review*, **115**, 51 – 74.

Back, L E, & Bretherton, C S. 2009. On the relationship between SST gradients, boundary layer winds, and convergence over the tropical oceans. *Journal of Climate*, **22**, 4182 – 4196.

Bagnato, S, Linsley, B K, Howe, S S, Wellington, G M, & Salinger, J. 2005. Coral oxygen isotope records of interdecadal climate variations in the South Pacific Convergence Zone region. *Geochemistry Geophysics Geosystems*, **6**, Q06001.

Barros, V, Gonzalez, M, Liebmann, B, & Camilloni, I. 2000. Influence of the South Atlantic convergence zone and South Atlantic Sea surface temperature on interannual summer rainfall variability in Southeastern South America. *Theoretical and Applied Climatology*, **67**, 123 – 133.

Battisti, D S, Sarachik, E S, & Hirst, A C. 1999. A consistent model for the large-scale steady surface atmospheric circulation in the tropics. *Journal of climate*, **12**, 2956–2964.

Bellucci, A, Gualdi, S, & Navarra, A. 2010. The double-ITCZ syndrome in coupled general circulation models: the role of large-scale vertical circulation regimes. *Journal of Climate*, **23**, 1127–1145.

Berry, G, Reeder, M J, & Jakob, C. 2011. A global climatology of atmospheric fronts. *Geophysical Research Letters*, **38**(4).

Betts, A K. 1986. A new convective adjustment scheme. Part I: Observational and

theoretical basis. *Quarterly Journal of the Royal Meteorological Society*, **112**, 677 – 691.

Bi, D, Dix, M, Marsland, S J, O'Farrell, S, Rashid, H, Uotila, P, Hirst, A, Kowalczyk, E, Golebiewski, M, Sullivan, A, Yan, H, Hannah, N, Franklin, C, Sun, Z, Vohralik, P, Watterson, I, Zhou, X, Fiedler, R, Collier, M, Ma, Y, Noonan, J, Stevens, L, Uhe, P, Zhu, H, Griffies, S M, Hill, R, Harris, C, & Puri, K. 2013. The ACCESS coupled model: description, control climate and evaluation. *Australian Meteorological Oceanographic Journal*, **63**, 41–64.

Bjerknes, J. 1969. Atmospheric teleconnections from the equatorial Pacific. *Monthly Weather Review*, **97**, 163 – 172.

Bony, S, Dufresne, J-L, Le Treut, H, Morcrette, J-J, & Senior, C. 2004. On dynamic and thermodynamic components of cloud changes. *Climate Dynamics*, **22**, 71–86.

Bony, S, Stevens, B, Frierson, D M W, Jakob, C, Kageyama, M, Pincus, R, Shepherd, T G, Sherwood, S C, Siebesma, A P, Sobel, A H, Watanabe, M, & Webb, M J. 2015. Clouds, circulation and climate sensitivity. *Nature Geoscience*, **8**, 261–268.

Borlace, S, Santoso, A, Cai, W, & Collins, M. 2014. Extreme swings of the South Pacific Convergence Zone and the different types of El Niño events. *Geophysical Research Letters*, **41**, 4695–4703.

Brierley, C M, & Fedorov, A V. 2010. Relative importance of meridional and zonal sea surface temperature gradients for the onset of the ice ages and Pliocene-Pleistocene climate evolution. *Paleoceanography*, **25**, PA2214.

Brown, J N, Gupta, A S, Brown, J R, Muir, L C, Risbey, J S, Whetton, P, Zhang, X, Ganachaud, A, Murphy, B, & Wijffels, S E. 2013. Implications of CMIP3 model biases and uncertainties for climate projections in the western tropical Pacific. *Climatic Change*, **119**, 147–161.

Brown, J R, Power, S B, Delage, F P, Colman, R A, Moise, A F, & Murphy, B F. 2011. Evaluation of the South Pacific Convergence Zone in IPCC AR4 climate model simulations of the twentieth century. *Journal of Climate*, **24**, 1565 – 1582.

Brown, J R, Moise, A F, & Delage, F P. 2012. Changes in the South Pacific Convergence Zone in IPCC AR4 future climate projections. *Climate Dynamics*, **39**, 1 – 19.

Brown, J R, Moise, A F, & Colman, R A. 2013. The South Pacific Convergence Zone in CMIP5 simulations of historical and future climate. *Climate Dynamics*, **41**, 2179 – 2197.

Cai, W, Lengaigne, M, Borlace, S, Collins, M, Cowan, T, McPhaden, M J, Timmermann, A, Power, S, Brown, J, Menkes, C, Ngari, A, Vincent, E M, & Widlansky, M J. 2012. More extreme swings of the South Pacific Convergence Zone due to greenhouse warming. *Nature*, **488**, 365 – 370.

Carvalho, L M V, Jones, C, & Liebmann, B. 2004. The South Atlantic Convergence Zone: intensity, form, persistence, and relationships with intraseasonal to interannual activity and extreme rainfall. *Journal of Climate*, **17**, 88 – 108.

Chaves, R R, & Nobre, P. 2004. The South Indian Convergence Zone and interannual rainfall variability over Southern Africa. *Geophysical Research Letters*, **31**, L03204.

Collins, W J, Bellouin, N, Doutriaux-Boucher, M, Gedney, N, Halloran, P, Hinton, T, Hughes, J, Jones, C D, Joshi, M, Liddicoat, S, Martin, G, O'Connor, F, Rae, J, Senior, C, Sitch, S, Totterdell, I, Wiltshire, A, & Woodward, S. 2011. Development and evaluation of an Earth-system model–HadGEM2. *Geoscientific Model Development*, **4**, 1051–1075.

Delworth, T L, Broccoli, A J, Rosati, A, Stouffer, R J, Balaji, V, Beesley, J A, Cooke, W F, Dixon, K W, Dunne, J Dunneand K A, Durachta, J W, Findell, K L, Ginoux, P, Gnanadesikan, A, Gordon, C T, Griffies, S M, Gudgel, R, Harrison, M J, Held, I M, Hemler, R S, Horowitz, L W, Klein, S A, Knutson, T R, Kushner, P J, Langenhorst, A R, Lee, H-C, Lin, S-J, Lu, J, Malyshev, S L, Milly, P C D, Ramaswamy, V, Russell, J, Schwarzkopf, M D, Shevliakova, E, Sirutis, J J, Spelman, M J, Stern, W F, Winton, M, Wittenberg, A T, Wyman, B, Zeng, F, & Zhang, R. 2006. GFDL's CM2 global coupled climate models. Part I: Formulation and simulation characteristics. *Journal of Climate*, **19**, 643–674.

Dix, M, Vohralik, P, Bi, D, Rashid, H A, Marsland, S J, O'Farrell, S, Uotila, P, Hirst, A C, Kowalcyzk, E A, Sullivan, A, Yan, H, Franklin, C, Sun, Z, Watterson, I, Collier, M, Noonan, J, Rotstayn, L, Stevens, L, Uhe, P, & Puri, K. 2013. The ACCESS Coupled Model: Documentation of core CMIP5 simulations and initial results. *Australian Meteorological Oceanographic Journal*, **63**, 83–99.

Donner, L J, Wyman, B L, Hemler, R S, Horowitz, L W, Ming, Y, Zhao, M, Golaz, J-C, Ginoux, P, Lin, S-J, Schwarzkopf, M D, Austin, J, Alaka, G, Cooke, W F, Delworth, T L, Freidenreich, S M, Gordon, C T, Griffies, S M, Held, I M, Hurlin, W J, Klein, S A, Knutson, T R, Langenhorst, A R, Lee, H-C, Lin, Y, Magi, B I, Malyshev, S L, Milly, P C D, Naik, V, Nath, M J, Pincus, R, Ploshay, J J, Ramaswamy, V, Seman,

C J, Shevliakova, E, Sirutis, J J, Stern, W F, Stouffer, R J, Wilson, R J, Winton, M, Wittenberg, A T, & Zeng, F. 2011. The dynamical core, physical parameterizations, and basic simulation characteristics of the atmospheric component AM3 of the GFDL global coupled model CM3. *Journal of Climate*, **24**, 3484–3519.

Duchon, C E. 1979. Lanczos filtering in one and two dimensions. *Journal of Applied Meteorology*, **18**, 1016 – 1022.

Dufresne, J-L, Foujols, M-A, Denvil, S, Caubel, A, Marti, O, Aumont, O, Balkanski, Y, Bekki, S, Bellenger, H, Benshila, R, Bony, S, Bopp, L, Braconnot, P, Brockmann, P, Cadule, P, Cheruy, F, Codron, F, Cozic, A, Cugnet, D, de Noblet, N, Duvel, J-P, Ethé, C, Fairhead, L, Fichefet, T, Flavoni, S, Friedlingstein, P, Grandpeix, J-Y, Guez, L, Guilyardi, E, Hauglustaine, D, Hourdin, F, Idelkadi, A, Ghattas, J, Joussaume, S, Kageyama, M, Krinner, G, Labetoulle, S, Lahellec, A, Lefebvre, M-P, Lefevre, F, Levy, C, Li, Z X, Lloyd, J, Lott, F, Madec, G, Mancip, M, Marchand, M, Masson, S, Meurdesoif, Y, Mignot, J, Musat, I, Parouty, S, Polcher, J, Rio, C, Schulz, M, Swingedouw, D, Szopa, S, Talandier, C, Terray, P, Viovy, N, & Vuichard, N. 2013. Climate change projections using the IPSL-CM5 Earth System Model: from CMIP3 to CMIP5. *Climate Dynamics*, **40**, 2123–2165.

Espinoza, J C, Marengo, J A, Ronchail, J, Carpio, J M, Flores, L N, & Guyot, J L. 2014. The extreme 2014 flood in south-western Amazon basin: the role of tropical-subtropical South Atlantic SST gradient. *Environmental Research Letters*, **9**, 124007.

Fogli, P G, Manzini, E, Vichi, M, Alessandri, A, Patara, L, Gualdi, S, Scoccimarro, E, Masina, S, & Navarra, A. 2009. *INGV-CMCC carbon (ICC): A carbon cycle Earth system model*. Tech. rept. 6. Centro Euro-Mediterraneo per i Cambiamenti Climatici.

Folland, C K, Renwick, J A, Salinger, M J, & Mullan, A B. 2002. Relative influences of the Interdecadal Pacific Oscillation and ENSO on the South Pacific Convergence Zone. *Geophysical Research Letters*, **29**, 1643.

Forster, P M de F, Blackburn, M, Glover, R, & Shine, K P. 2000. An examination of climate sensitivity for idealised climate change experiments in an intermediate general circulation model. *Climate Dynamics*, **16**, 833 – 849.

Gent, P R, Danabasoglu, G, Donner, L J, Holland, M M, Hunke, E C, Jayne, S R, Lawrence, D M, Neale, R B, Rasch, P J, Vertenstein, M, Worley, P H, Yang, Z-L, & Zhang, M. 2011. The community climate system model version 4. *Journal of*

Climate, **24**, 4973–4991.

Gill, A E. 1980. Some simple solutions for heat-induced tropical circulation. *Quarterly Journal of the Royal Meteorological Society*, **106**, 447 – 462.

Gill, A E. 1982. *Atmosphere-Ocean Dynamics*. San Diego, CA, USA: Academic Press, Inc.

Giorgetta, M A, Jungclaus, J, Reick, C H, Legutke, S, Bader, J, Böttinger, M, Brovkin, V, Crueger, T, Esch, M, Fieg, K, Glushak, K, Gayler, V, Haak, H, Hollweg, H-D, Ilyina, T, Kinne1, S, Kornblueh, L, Matei, D, Mauritsen, T, Mikolajewicz, U, Mueller, W, Notz, D, Pithan, F, Raddatz, T, Rast, S, Redler, R, Roeckner, E, Schmidt, H, Schnur, R, Segschneider, J, Six, K D, Stockhause, M, Timmreck, C, Wegner, J, Widmann, H, Wieners, K-H, Claussen, M, Marotzke, J, & Stevens, B. 2013. Climate and carbon cycle changes from 1850 to 2100 in MPI-ESM simulations for the Coupled Model Intercomparison Project phase 5. *Journal of Advances in Modeling Earth Systems*, **5**, 572–597.

Godshall, F A. 1968. Intertropical convergence zone and mean cloud amount in the tropical Pacific Ocean. *Monthly Weather Review*, **96**, 172–175.

Griffiths, G M, Salinger, M H, & Leleu, I. 2003. Trends in extreme daily rainfall across the South Pacific and relationship to the South Pacific Convergence Zone. *International Journal of Climatology*, **23**, 847 – 869.

Grimm, A M, & Silva Dias, P L. 1995. Analysis of tropical-extratropical interactions with influence functions of a barotropic model. *Journal of the Atmospheric Sciences*, **52**, 3538 – 3555.

Grimm, A M, Barros, V R, & Doyle, M E. 2000. Climate variability in southern South America associated with El Niño and La Niña events. *Journal of Climate*, **13**, 36 – 58.

Grody, N C. 1991. Classification of snow cover and precipitation using the special sensor microwave imager. *Journal of Geophysical Research*, **96**, 7423 – 7435.

Gutzler, D S, & Wood, T M. 1990. Structure of large-scale convective anomalies over tropical oceans. *Journal of Climate*, **3**, 483 – 496.

Haffke, C, & Magnusdottir, G. 2013. The South Pacific Convergence Zone in three decades of satellite images. *Journal of Geophysical Research*, **118**, 1 – 11.

Held, I M, & Soden, B J. 2006. Robust responses of the hydrological cycle to global warming. *Journal of Climate*, **19**, 5686 – 5699.

Holton, J R. 2004. *An introduction to dynamical meteorology*. Fourth edn. Burlington, MA, USA: Elsevier Academic Press.

Hoskins, B J, & Ambrizzi, T. 1993. Rossby wave propagation on a realistic longitudinally varying flow. *Journal of Atmospheric Sciences*, **50**, 797 – 812.

Hoskins, B J, & Karoly, D J. 1981. The steady linear response of a spherical atmosphere to thermal and orographic forcing. *Journal of the Atmospheric Sciences*, **38**, 1179 – 1196.

Hoskins, B J, & Simmons, A J. 1975. A multi-layer spectral model and the semi-implicit method. *Quarterly Journal of the Royal Meteorological Society*, **101**, 637 – 655.

Hubert, L F. 1961. A subtropical convergence line of the South Pacific: a case study using meteorological satellite data. *Journal of Geophysical Research*, **66**, 1661 – 1671.

Hurrell, J W, Holland, M M, Gent, P R, Ghan, S, Kay, J E, Kushner, P J, Lamarque, J-F, Large, W G, Lawrence, D, Lindsay, K, Lipscomb, W H, Long, M C, Mahowald, N, Marsh, D R, Neale, R B, Rasch, P, Vavrus, S, Vertenstein, M, Bader, D, Collins, W D, Hack, J J, Kiehl, J, & Marshall, S. 2013. The community earth system model: A framework for collaborative research. *Bulletin of the American Meteorological Society*, **94**, 1339–1360.

IPCC. 2000. *Emissions Scenarios*. Cambridge, United Kingdom: Cambridge University Press.

IPCC. 2013. *Climate Change 2013: The Physical Science Basis. Contribution of Working Group I to the Fifth Assessment Report of the Intergovernmental Panel on Climate Change*. Cambridge, United Kingdom and New York, NY, USA: Cambridge University Press.

Iversen, T, Bentsen, M, Bethke, I, Debernard, J B, Kirkevåg, A, Seland, Ø, Drange, H, Kristjánsson, J E, Medhaug, I, Sand, M, & Seierstad, I A. 2013. The Norwegian earth system model, NorESM1-M – Part 2: Climate response and scenario projections. *Geoscientific Model Development*, **6**, 389–415.

Janowiak, J E, & Arkin, P A. 1991. Rainfall variation in the tropics during 1986-1989, as estimated from observations of cloud-top temperature. *Journal of Geophysical Research*, **96**, 3359 – 3373.

Ji, D, Wang, L, Feng, J, Wu, Q, Cheng, H, Zhang, Q, Yang, J, Dong, W, Dai, Y, Gong, D, Zhang, R-H, Wang, X, Liu, J, Moore, J C, Chen, D, & Zhou, M. 2014. Description

and basic evaluation of Beijing Normal University Earth System Model (BNU-ESM) version 1. *Geoscientific Model Development*, **7**, 2039–2064.

Jin, F, & Hoskins, B J. 1995. The direct response to tropical heating in a baroclinic atmosphere. *Journal of the Atmospheric Sciences*, **52**, 307 – 319.

Jorgetti, T, da Silva Dias, P L, & de Freitas, E D. 2014. The relationship between South Atlantic SST and SACZ intensity and positioning. *Climate Dynamics*, **42**, 3077–3086.

Joshi, M M, Stringer, M, Van der Wiel, K, O'Callaghan, A, & Fueglistaler, S. 2015. IGCM4: a fast, parallel and flexible intermediate climate model. *Geoscientific Model Development*, **8**, 1157–1167.

Juillet-Leclerc, A, Thiria, S, Naveau, P, Delcroix, T, Le Bec, N, Blamart, D, & Correge, T. 2006. SPCZ migration and ENSO events during the 20th century as revealed by climate proxies from a Fiji coral. *Geophysical Research Letters*, **33**.

Kalnay, E, Kanamitsu, M, Kistler, R, Collins, W, Deaven, D, Gandin, L, Iredell, M, Saha, S, White, G, Woollen, J, Zhu, Y, Leetmaa, A, Reynolds, R, Chelliah, M, Ebisuzaki, W, Higgins, W, Janowiak, J, Ropelewski, K C Mo C, Wang, J, Jenne, R, & Joseph, D. 1996. The NCEP/NCAR 40-year Reanalysis Project. *Bulletin of the American Meteorological Society*, **77**, 437–473.

Kanamitsu, M, Ebisuzaki, W, Yang, S-K, Hnilo, J J, Fiorino, M, & Potter, G L. 2002. NCEP DOE AMIP-II Reanalysis (R-2). *Bulletin of the American Meteorological Society*, **83**, 1631 – 1643.

Karoly, D J. 1983. Rossby wave propagation in a barotropic atmosphere. *Dynamics of Atmospheres and Oceans*, **7**, 111 – 125.

Kawai, H, & Inoue, T. 2006. A simple parameterization scheme for subtropical marine stratocumulus. *Scientific Online Letters on the Atmosphere*, **2**, 17–20.

Kayano, R T, & Andreoli, M V. 2007. Relations of South American summer rainfall interannual variations with the Pacific Decadal Oscillation. *International Journal of Climatology*, **27**, 531–540.

Kiladis, G N. 1998. Observations of Rossby waves linked to convection over the eastern tropical Pacific. *Journal of Atmospheric Sciences*, **55**, 321 – 339.

Kiladis, G N, & Weickmann, K M. 1992a. Circulation anomalies associated with tropical convection during northern winter. *Monthly Weather Review*, **120**, 1900 – 1923.

Kiladis, G N, & Weickmann, K M. 1992b. Extratropical forcing of tropical Pacific

convection during northern winter. *Monthly Weather Review*, **120**, 1924 – 1938.

Kiladis, G N, von Storch, H, & van Loon, H. 1989. Origin of the South Pacific Convergence Zone. *Journal of Climate*, **2**, 1185 – 1195.

Kitoh, A. 1997. Mountain uplift and surface temperature changes. *Geophysical Research Letters*, **24**, 185–188.

Kitoh, A. 2002. Effects of large-scale mountains on surface climate. A coupled ocean-atmosphere general circulation model study. *Journal of the Meteorological Society of Japan*, **80**, 1165 – 1181.

Kodama, Y M. 1992. Large-scale common features of subtropical precipitation zones (the Baiu Frontal Zone, the SPCZ, and the SACZ) part I: characteristics of subtropical frontal zones. *Journal of the Meteorological Society of Japan*, **70**, 813 – 836.

Kodama, Y M. 1993. Large-scale common features of subtropical convergence zones (the Baiu Frontal Zone, the SPCZ, and the SACZ) part II: conditions of the circulations for generating the STCZs. *Journal of the Meteorological Society of Japan*, **71**, 581 – 610.

Kornfield, J, & Hasler, A F. 1969. A photographic summary of the Earth's cloud cover for the year 1967. *Journal of Applied Meteorology*, **8**, 687 – 700.

Kornfield, J, Hasler, A F, Hansen, K J, & Suomi, V E. 1967. Photographic cloud climatology from ESSA III and V computer produced mosaics. *Bulletin of the American Meteorological Society*, **48**, 878 – 883.

Kumar, V V, Deo, R C, & Ramachandran, V. 2006. Total rain accumulation and rain-rate analysis for small tropical Pacific islands: a case study of Suva, Fiji. *Atmospheric Science Letters*, **7**, 53 – 58.

Lau, K-M, & Chan, P H. 1983. Short-term climate variability and atmospheric teleconnections from satellite-observed outgoing longwave radiation. I: Simultaneous relationships. *Journal of the Atmospheric Sciences*, **40**, 2735 – 2750.

Li, L, Lin, P, Yu, Y, Wang, B, Zhou, T, Liu, L, Liu, J, Bao, Q, Xu, S, Huang, W, Xia, K, Pu, Y, Dong, L, Shen, S, Liu, Y, Hu, N, Liu, M, amd X Shi, W Sun, Zheng, W, Wu, B, Song, M, Liu, H, Zhang, X, Wu, G, Xue, W, Huang, X, Yang, G, Song, Z, & Qiao, F. 2013. The flexible global ocean-atmosphere-land system model, Grid-point Version 2: FGOALS-g2. *Advances in Atmospheric Sciences*, **30**, 543–560.

Liebmann, B, & Smith, C A. 1996. Description of a complete (interpolated) outgoing

longwave radiation dataset. *Bulletin of the American Meteorological Society*, **77**, 1275 – 1277.

Liebmann, B, Kiladis, G N, Marengo, J A, Ambrizzi, T, & Glick, J D. 1999. Submonthly convective variability over South America and the South Atlantic convergence zone. *Journal of Climate*, **12**, 1877 – 1891.

Lin, J-L. 2007. The double-ITCZ problem in IPCC AR4 coupled GCMs: Ocean-atmosphere feedback analysis. *Journal of Climate*, **20**, 4497–4525.

Lindzen, R S, & Nigam, S. 1987. On the role of sea surface temperature gradients in forcing low-level winds and convergence in the tropics. *Journal of the Atmospheric Sciences*, **44**, 2418–2436.

Lintner, B R, & Neelin, J D. 2008. Eastern margin variability of the South Pacific Convergence Zone. *Geophysical Research Letters*, **35**, L16701.

Lorrey, A, Dalu, G, Renwick, J, Diamond, H, & Gaetini, M. 2012. Reconstructing the South Pacific Convergence Zone position during the presatellite era: a La Niña case study. *Monthly Weather Review*, **140**, 3653–3668.

Madden, R A, & Julian, P R. 1971. Detection of a 40-50 day oscillation in the zonal wind in the tropical Pacific. *Journal of the Atmospheric Sciences*, **28**, 702 – 708.

Madden, R A, & Julian, P R. 1972. Description of global-scale circulation cells in the tropics with a 40-50 day period. *Journal of the Atmospheric Sciences*, **29**, 1109 – 1123.

Martin, G M, Bellouin, N, Collins, W J, Culverwell, I D, Halloran, P R, Hardiman, S C, Hinton, T J, Jones, C D, McDonald, R E, McLaren, A J, O'Connor, F M, Roberts, M J, Rodriguez, J M, Woodward, S, Best, M J, Brooks, M E, Brown, A R, Butchart, N, Dearden, C, Derbyshire, S H, Dharssi, I, Doutriaux-Boucher, M, Edwards, J M, Falloon, P D, Gedney, N, Gray, L J, Hewitt, H T, Hobson, M, Huddleston, M R, Hughes, J, Ineson, S, Ingram, W J, James, P M, Johns, T C, Johnson, C E, Jones, A, Jones, C P, Joshi, M M, Keen, A B, Liddicoat, S, Lock, A P, Maidens, A V, Manners, J C, Milton, S F, Rae, J G L, Ridley, J K, Sellar, A, Senior, C A, Totterdell, I J, Verhoef, A, Vidale, P L, & Wiltshire, A. 2011. The HadGEM2 family of met office unified model climate configurations. *Geoscientific Model Development*, **4**, 723–757.

Matsuno, T. 1966. Quasi-Geostrophic motions in the equatorial area. *Journal of the Meteorological Society of Japan*, **44**, 25 – 42.

Matthews, A J. 2012. A multiscale framework for the origin and variability of the South

Pacific Convergence Zone. *Quarterly Journal of the Royal Meteorological Society*, **138**, 1165 – 1178.

Matthews, A J, & Kiladis, G N. 2000. A model of Rossby waves linked to submonthly convection over the eastern tropical Pacific. *Journal of the Atmospheric Sciences*, **57**, 3785–3798.

Matthews, A J, Hoskins, B J, Slingo, J M, & Blackburn, M. 1996. Development of convection along the SPCZ within a Madden-Julian Oscillation. *Quarterly Journal of the Royal Meteorological Society*, **122**, 669 – 688.

Matthews, A J, Hoskins, B J, & Masutani, M. 2004. The global response to tropical heating in the Madden-Julian Oscillation during northern winter. *Quarterly Journal of the Royal Meteorological Society*, **130**, 1991 – 2011.

McClymont, E L, & Rosell-Mele, A. 2005. Links between the onset of modern Walker circulation and the mid-Pleistocene climate transition. *Geology*, **33**, 389 – 392.

McGregor, S, Timmerman, A, Schneider, N, Stuecker, M R, & England, M H. 2012. The effect of the South Pacific Convergence Zone on the termination of El Niño events and the meridional asymmetry of ENSO. *Journal of Climate*, **25**, 5566 – 5586.

Meehl, G A. 1987. The Annual Cycle and Interannual Variability in the Tropical Pacific and Indian Ocean Regions. *Monthly Weather Review*, **115**, 27 – 50.

Meehl, G A, Lukas, R, Kiladis, G N, Weickmann, K M, Matthews, A J, & Wheeler, M. 2001. A conceptual framework for time and space scale interactions in the climate system. *Climate Dynamics*, **17**, 753 – 775.

Meehl, G A, Covey, C, Taylor, K E, Delworth, T, Stouffer, R J, Latif, M, McAvaney, B, & Mitchell, J F B. 2007. The WCRP CMIP3 multimodel dataset: A new era in climate change research. *Bulletin of the American Meteorological Society*, **88**, 1383–1394.

Murphy, B F, Power, S B, & McGree, S. 2014. The varied impacts of El Niño-Southern Oscillation on Pacific island climates. *Journal of Climate*, **27**, 4015 – 4036.

Neelin, J D. 1989. On the interpretation of the Gill model. *Journal of the Atmospheric Sciences*, **46**, 2466 – 2468.

Nieto Ferreira, R, & Chao, W C. 2013. Aqua-planet simulations of the formation of the South Atlantic convergence zone. *International Journal of Climatology*, **33**, 615 – 628.

Nieto Ferreira, R, Rickenbach, T M, & Wright, E A. 2011. The role of cold fronts in the onset of the monsoon season in the South Atlantic convergence zone. *Quarterly*

Journal of the Royal Meteorological Society, **137**, 908 – 922.

Niznik, M J, & Lintner, B R. 2013. Circulation, moisture and precipitation relationships along the South Pacific Convergence Zone in reanalyses and CMIP5 models. *Journal of Climate*, **26**, 10174 – 10192.

Niznik, M J, Lintner, B R, Matthews, A J, & Widlansky, M J. 2015. The role of tropical-extratropical interaction and synoptic variability in maintaining the South Pacific Convergence Zone in CMIP5 models. *Journal of Climate*. accepted for publication.

North, G R, Bell, T L, & Cahalan, R F. 1982. Sampling errors in the estimation of empirical orthogonal functions. *Monthly Weather Review*, **110**, 699 – 706.

Ortega, P, & Guignes, T. 2007. Lightning activity analyses with respect to the SPCZ location. *Geophysical Research Letters*, **34**, L11807.

Power, S. 2011. Understanding the South Pacific Convergence Zone and Its Impacts. *Eos*, **92**, 55–55.

Power, S, Casey, T, Folland, C, Colman, A, & Mehta, V. 1999. Inter-decadal modulation of the impact of ENSO on Australia. *Climate Dynamics*, **15**, 319–324.

Qin, J, & Robinson, W A. 1993. On the Rossby Wave Source and the steady linear response to tropical forcing. *Journal of the Atmospheric Sciences*, **50**, 1819 – 1823.

Reynolds, R W, Rayner, N A, Smith, T M, Stokes, D C, & Wang, W. 2002. An improved in situ and satellite SST analysis for climate. *Journal of Climate*, **15**, 1609 – 1625.

Riemann-Campe, K, Fraedrich, K, & Lunkeit, F. 2009. Global climatology of convective available potential energy (CAPE) and convective inhibition (CIN) in ERA-40 reanalysis. *Atmospheric Research*, **93**, 534 – 545.

Robertson, A W, & Mechoso, C R. 2000. Interannual and interdecadal variability of the South Atlantic Convergence Zone. *Monthly Weather Review*, **128**, 2947 – 2957.

Rotstayn, L D, Jeffrey, S J, Collier, M A, Dravitzki, S M, Hirst, A C, Syktus, JI, & Wong, K K. 2012. Aerosol-and greenhouse gas-induced changes in summer rainfall and circulation in the Australasian region: a study using single-forcing climate simulations. *Atmospheric Chemistry and Physics*, **12**, 6377–6404.

Rudolf, B, Hauschild, H, Rueth, W, & Schneider, U. 1994. Terrestrial precipitation analysis: Operational method and required density of point measurements. *NATO ASI Series*, **126**, 173 – 186.

Saint-Lu, M, Braconnet, P, Leloup, J, Lengaigne, M, & Marti, O. 2015. Changes in the ENSO/SPCZ relationship from past to future climates. *Earth and Planetary Science*

Letters, **412**, 18 – 24.

Salby, M L. 2012. *Physics of the atmosphere and climate*. First edn. New York, NY, USA: Cambridge University Press.

Salinger, M J, Basher, R E, Fitzharris, B B, Hay, J E, Jones, P D, Macveigh, J P, & Schmidely-Leleu, I. 1995. Climate trends in the south-west Pacific. *International Journal of Climatology*, **15**, 285 – 302.

Salinger, M J, Renwick, J A, & Mullan, A B. 2001. Interdecadal Pacific Oscillation and South Pacific climate. *International Journal of Climatology*, **21**, 1705 – 1721.

Schmidt, G A, Ruedy, R, Hansen, J E, Aleinov, I, Bell, N, Bauer, M, Bauer, S, Cairns, B, Cheng, V Canutoand Y, Genio, A D, Faluvegi, G, Friend, A D, Hall, T M, Hu, Y, Kelley, M, Kiang, N Y, Koch, D, Lacis, A A, Lerner, J, Lo, K K, Miller, R L, Nazarenko, L, Oinas, V, Perlwitz, J, Perlwitz, J, Rind, D, Romanou, A, Russell, G L, Sato, M, Shindell, D T, Stone, P H, Sun, S, Tausnev, N, Thresher, D, & Yao, M-S. 2006. Present-day atmospheric simulations using GISS ModelE: Comparison to in situ, satellite, and reanalysis data. *Journal of Climate*, **19**, 153–192.

Seager, R, & Murtugudde, R. 1997. Ocean dynamics, thermocline adjustment, and regulation of tropical SST. *Journal of Climate*, **10**, 521–534.

Slingo, J M. 1987. The development and verification of a cloud prediction scheme for the ECMWF model. *Quarterly Journal of the Royal Meteorological Society*, **113**, 899 – 927.

Spencer, R W. 1993. Global oceanic precipitation from the MSU during 1979-91 and comparisons to other climatologies. *Journal of Climate*, **6**, 1301 – 1326.

Streten, N A. 1970. A note on the climatology of the satellite observed zone of high cloudness in the central South Pacific. *Australian Meteorological Magazine*, **18**, 31 – 38.

Streten, N A. 1973. Some characteristics of satellite-observed bands of persistent cloudiness over the Southern Hemisphere. *Monthly Weather Review*, **101**, 486 – 495.

Takahashi, K, & Battisti, D S. 2007a. Processes controlling the mean tropical Pacific precipitation pattern. Part I: The Andes and the Eastern Pacific ITCZ. *Journal of Climate*, **20**, 3434 – 3451.

Takahashi, K, & Battisti, D S. 2007b. Processes controlling the mean tropical Pacific precipitation pattern. Part II: the SPCZ and the southeast Pacific dry zone. *Journal*

of Climate, **20**, 5696 – 5706.

Todd, M C, Washington, R, & James, T. 2003. Characteristics of summertime daily rainfall variability over South America and the South Atlantic convergence zone. *Meteorology and Atmospheric Physics*, **83**, 89 – 108.

Trenberth, K E. 1976. Spatial and temporal variations of the Southern Oscillation. *Quarterly Journal of the Royal Meteorological Society*, **102**, 639 – 653.

Trenberth, K E. 1991. *Teleconnections linking worldwide climate anomalies*. Cambridge University Press. Chap. General characteristics of El Niño-Southern Oscillation, pages 13–41.

Van der Wiel, K, Matthews, A J, Stevens, D P, & Joshi, M M. 2015a. A dynamical framework for the origin of the diagonal South Pacific and South Atlantic Convergence Zones. *Quarterly Journal of the Royal Meteorological Society*. published online, doi: 10.1002/qj.2508.

Van der Wiel, K, Matthews, A J, Joshi, M M, & Stevens, D P. 2015b. Why the South Pacific Convergence Zone is diagonal. *Climate Dynamics*. published online, doi: 10.1007/s00382-015-2668-0.

Vincent, D G. 1994. The South Pacific Convergence Zone (SPCZ): a review. *Monthly Weather Review*, **122**, 1949 – 1970.

Vincent, E M, Lengaigne, M, Menkes, C E, Jourdain, N C, Marchesiello, P, & Madec, G. 2011. Interannual variability of the South Pacific Convergence Zone and implications for tropical cyclone genesis. *Climate Dynamics*, **36**, 1881 – 1896.

Voldoire, A, Sanchez-Gomez, E, Salas y Mélia, D, Decharme, B, Cassou, C, Sénési, S, Valcke, S, Beau, I, Alias, A, Chevallier, M, Déqué, M, Deshayes, J, Douville, H, Fernandez, E, Madec, G, Maisonnave, E, Moine, M-P, Planton, S, Saint-Martin, D, Szopa, S, Tyteca, S, Alkama, R, Belamari, S, Braun, A, Coquart, L, & Chauvin, F. 2013. The CNRM-CM5.1 global climate model: description and basic evaluation. *Climate Dynamics*, **40**, 2091–2121.

Von Salzen, K, Scinocca, J F, McFarlane, N A, Li, J, Cole, J N S, Plummer, D, Verseghy, D, Reader, M C, Ma, X, Lazare, M, & Solheim, L. 2013. The Canadian fourth generation atmospheric global climate model (CanAM4). Part I: representation of physical processes. *Atmosphere-Ocean*, **51**, 104–125.

Wang, B, & Li, T. 1993. A simple tropical atmosphere model of relevance to short-term climate variations. *Journal of the Atmospheric Sciences*, **50**, 260 – 284.

Watanabe, M, Suzuki, T, O'ishi, R, Komuro, Y, Watanabe, S, Emori, S, Takemura, T, Chikira, M, Ogura, T, Sekiguchi, M, Takata, K, Yamazaki, D, Yokohata, T, Nozawa, T, Hasumi, H, Tatebe, H, & Kimoto, M. 2010. Improved climate simulation by MIROC5: mean states, variability, and climate sensitivity. *Journal of Climate*, **23**, 6312–6335.

Webster, P J, & Chang, H-R. 1991. Atmospheric wave propagation in heterogeneous flow: basic flow controls on tropical-extratropical interaction and equatorial wave modification. *Dynamics of Atmospheres and Oceans*, **27**, 91 – 134.

Webster, P J, & Holton, J R. 1982. Cross-equatorial response to middle-latitude forcing in a zonally varying basic state. *Journal of the Atmospheric Sciences*, **39**, 722 – 733.

Wheeler, M C, & Hendon, H H. 2004. An all-season real-time multivariate MJO index: development of an index for monitoring and prediction. *Monthly Weather Review*, **132**, 1917 – 1932.

Widlansky, M J. 2010. *Climate dynamics of the South Pacific Convergence Zone and similarities with other subtropical convergence zones in the southern hemisphere*. Ph.D. thesis, Georgia Institute of Technology.

Widlansky, M J, Webster, P J, & Hoyos, C D. 2011. On the location and orientation of the South Pacific Convergence Zone. *Climate Dynamics*, **36**, 561 – 578.

Widlansky, M J, Timmermann, A, Stein, K, McGregor, S, Schneider, N, England, M H, Lengaigne, M, & Cai, W. 2013. Changes in South Pacific rainfall bands in a warming climate. *Nature Climate Change*, **3**, 417 – 423.

Widlansky, M J, Timmermann, A, & Cai, W. 2014. An interhemispheric tropical sea level seesaw due to El Niño Taimasa. *Journal of Climate*, **27**, 1070 – 1081.

Wilheit, T T, Chang, A T C, & Chiu, L S. 1991. Retrieval of the monthly rainfall indices from microwave radiometric measurements using probability distribution functions. *Journal of Atmospheric and Oceanic Technology*, **8**, 118 – 136.

Wilks, D S. 2006. *Statistical methods in the atmospheric sciences*. Second edn. Burlington, MA, USA: Elsevier Academic Press.

Wu, T. 2012. A mass-flux cumulus parameterization scheme for large-scale models: Description and test with observations. *Climate dynamics*, **38**, 725–744.

Xie, P, & Arkin, P A. 1997. Global precipitation: a 17-year monthly analysis based on gauge observations, satellite estimates, and numerical model outputs. *Bulletin of the American Meteorological Society*, **78**, 2539 – 2558.

Xie, P, & Arkin, P A. 1998. Global montly precipitation extimates from satellite-observed Outgoing Longwave Radiation. *Journal of Climate*, **11**, 137 – 164.

Xin, X, Zhang, L, Zhang, J, Wu, T, & Fang, Y. 2013. Climate change projections over East Asia with BCC_CSM1.1 climate model under RCP scenarios. *Journal of the Meteorological Society Japan*, **91**, 413–429.

Xin, X-G, Wu, T, Li, J-L, Wang, Z-Z, Li, W-P, & Wu, F-H. 2012. How well does BCC_CSM1.1 reproduce the 20th century climate change over China? *Atmospheric and Oceanic Science Letters*, **6**, 21–26.

Yang, G-Y, & Hoskins, B J. 1996. Propagation of Rossby waves of nonzero frequency. *Journal of the Atmospheric Sciences*, **53**, 2365 – 2378.

Yukimoto, S, Yoshimura, H, Hosaka, M, Sakami, T, Tsujino, H, Hirabara, M, Tanaka, T Y, Deushi, M, Obata, A, Nakano, H, Adachi, Y, Shindo, E, Yabu, S, Ose, T, & Kitoh, A. 2011. *Meteorological Research Institute-Earth System Model version 1 (MRI-ESM1) - model description* -. Tech. rept. 64. Meteorological Research Institute.

Yukimoto, S, Adachi, Y, Hosaka, M, Sakami, T, Yoshimura, H, Hirabara, M, Tanaka, T Y, Shindo, E, Tsujino, H, Deushi, M, Mizuta, R, Yabu, S, Obata, A, Nakano, H, Koshiro, T, Ose, T, & Kitoh, A. 2012. A new global climate model of the Meteorological Research Institute: MRI-CGCM3—model description and basic performance. *Journal of the Meteorological Society of Japan*, **90**, 23–64.

Zhang, C. 2005. Madden-Julian Oscillation. *Review of Geophysics*, **43**, RG2003.

Zhang, G J, & Wang, H. 2006. Toward mitigating the double ITCZ problem in NCAR CCSM3. *Geophysical Research Letters*, **33**.

Zhang, X, Lin, W, & Zhang, M. 2007. Toward understanding the double Intertropical Convergence Zone pathology in coupled ocean-atmosphere general circulation models. *Journal of Geophysical Research: Atmospheres*, **112**.

Zhong, W Y, & Haigh, J D. 1995. Improved broad-band emissivity parameterization for water vapor cooling calculations. *Journal of Atmospheric Sciences*, **52**, 124 – 138.